



Precision measurements of the electron energy distribution in nuclear beta decays

Maciej Perkowski

Supervisors:

Prof. dr hab. K. Bodek

(Jagiellonian University in Kraków)

Prof. dr. N. Severijns

Co-supervisor:

Dr. D. Rozpędzik

(Jagiellonian University in Kraków)

Dissertation presented in partial fulfillment
of the requirements for the degrees of
Doctor of Science (PhD): Physics
at Katholieke Universiteit Leuven and
Doctor of Physical Science in Physics
at Jagiellonian University in Kraków

April 2020

Precision measurements of the electron energy distribution in nuclear beta decays

Maciej PERKOWSKI

Examination committee:

Prof. dr. V Afanasiev, chair

Prof. dr hab. K. Bodek, supervisor
(Jagiellonian University in Kraków)

Prof. dr. N. Severijns, supervisor

Prof. dr. T. Cocolios

Prof. dr. R. Raabe

Dr. D. Rozpędzik

(Jagiellonian University in Kraków)

Dissertation presented in partial fulfillment of the requirements for the degrees of Doctor of Science: Physics at Katholieke Universiteit Leuven and Doctor of Physical Science in Physics at Jagiellonian University in Kraków

April 2020

© 2020 KU Leuven – Faculty of Science
© 2020 Uniwersytet Jagielloński w Krakowie – Wydział Fizyki, Astronomii i Informatyki Stosowanej
Uitgegeven in eigen beheer, Maciej Perkowski

Alle rechten voorbehouden. Niets uit deze uitgave mag worden vermenigvuldigd en/of openbaar gemaakt worden door middel van druk, fotokopie, microfilm, elektronisch of op welke andere wijze ook zonder voorafgaande schriftelijke toestemming van de uitgever.

All rights reserved. No part of the publication may be reproduced in any form by print, photoprint, microfilm, electronic or any other means without written permission from the publisher.

Declaration

Wydział Fizyki, Astronomii i Informatyki Stosowanej

Uniwersytet Jagielloński

Oświadczenie

Ja niżej podpisany Maciej Perkowski (nr indeksu: 1028844) doktorant Wydziału Fizyki, Astronomii i Informatyki Stosowanej Uniwersytetu Jagiellońskiego oświadczam, że przedłożona przeze mnie rozprawa doktorska pt. "Precision measurements of the electron energy distribution in nuclear beta decays" jest oryginalna i przedstawia wyniki badań wykonanych przeze mnie osobiście, pod kierunkiem prof. dr. hab. Kazimierza Bodka, prof. dr. Nathala Severijnsa i dr. Dagmary Rozpędzik. Pracę napisałem samodzielnie.

Oświadczam, że moja rozprawa doktorska została opracowana zgodnie z Ustawą o prawie autorskim i prawach pokrewnych z dnia 4 lutego 1994 r. (Dziennik Ustaw 1994 nr 24 poz. 83 wraz z późniejszymi zmianami).

Jestem świadom, że niezgodność niniejszego oświadczenia z prawdą ujawniona w dowolnym czasie, niezależnie od skutków prawnych wynikających z ww. ustawy, może spowodować unieważnienie stopnia nabytego na podstawie tej rozprawy.

Kraków, dnia 28.04.2020



Acknowledgements

I would like to express gratitude to all the people who were standing by my side during my journey for the PhD title. It was a long and sometimes rough path. However, with your help, I reached the goal.

Thanks to unconditional trust and support of my family (Andrzej, Małgorzata and Rafał) I was able to withstand the stress that was lurking in shadows of this path. Paulina helped me to keep focused and motivated, which was crucial at the end of the process. I am also thankful to all my friends who would not let me forget the joy of life.

I am very grateful to my colleagues, who were working with me on the miniBETA spectrometer: Clare, Dagmara, Gergely, Konrad, Lennert, Leendert, and Paul. Our fruitful discussions and hours spent together in the lab were invaluable and pushed the project forward.

Finally, I would like to acknowledge my supervisors: Dagmara, Kazimierz and Nathal. All the insightful comments, ideas and advice showed me how to aim for higher standards.

Thank you!
Maciej

Abstract

Although nuclear β decays have been studied for almost a century, there are still questions that can be answered through precision measurements of the energy distribution of emitted electrons. The shape of the β spectrum reflects not only the weak interaction responsible for the decay. It is also sensitive to the strong interaction which confines the decaying quark in the nucleon. The electromagnetic force also plays a role since the ejected electron interacts with the charged nucleus. Therefore, measurements of the β spectrum shape are an important tool in understanding all the interactions combined in the Standard Model (SM) and high precision is required to disentangle the effects of different interactions. Moreover, these measurements can even shed some light on New Physics (NP), if discrepancies between the shape of a measured spectrum and the one predicted by the SM are observed.

One of the open questions is the validity of the $V - A$ form of the weak interaction Lagrangian. Measurements of the β spectrum directly address this issue, since the exotic currents (i.e. other than V and A) affect the spectrum shape through the so-called Fierz interference term b . An experiment sensitive to NP requires a precision at the level of 10^{-3} to be able to compete with energy frontier measurements performed at the Large Hadron Collider.

When precision is at stake, the success of an experiment is determined by a proper understanding of its systematic uncertainties. The main limitation of the precision of spectra measurements comes from the properties of the energy detector being used in the experiment. In particular, from the accuracy of the detector energy response and of the energy deposition model in the detector active volume. The miniBETA spectrometer was designed to measure β spectra with a precision at the level of 10^{-3} . It combines a plastic scintillator energy detector with a multi-wire drift chamber where electrons emitted from a decaying source are traced in three dimensions.

Using the plastic scintillator minimizes systematic effects related to the model of the energy deposition in the detector active volume. Due to the low Z of the plastic and a choice of the detector thickness, the probability that the energy is fully deposited is highest. Keeping the probability of other processes (i.e. backscattering, bremsstrahlung, and transmission) low reduces the influence of their uncertainties on the predicted spectrum. Particle tracking filters the measured spectrum from events not originating from electrons emitted from the source. It also allows for a recognition of backscattering events, further reducing their influence.

The thesis describes the commissioning of the miniBETA spectrometer. Several gas mixtures of helium and isobutane were tested as media for tracking particles. Calibrations of the drift chamber response were based on measurements of cosmic muons. The mean efficiency of detecting an ionizing particle in a single drift cell reached 0.98 for mixtures at 600 mbar and 0.95 at 300 mbar. The spatial resolution of a single cell, determined from the drift time, reached 0.4 mm and 0.8 mm, respectively. The resolution determined from the charge division was roughly an order of magnitude worse. Several corrections dealing with systematic effects were investigated, like a correction for a signal wire misalignment sensitive to shifts as small as 0.02 mm.

It was shown that particle tracking improves the precision of spectrum measurements, as the response of the spectrometer depends on the position where the scintillator was hit. Preliminary calibration of the energy response of the spectrometer was performed with a ^{207}Bi source. The calibration was based on fitting the measured spectrum with a spectrum being a convolution of simulated energy deposited in the scintillator and the spectrometer response. The energy resolution of the prototypical setup is $\rho_{1\text{MeV}} = 7.6\%$. The uncertainty of the scale parameter, hindering the extraction of energy dependent terms (i.e. the Fierz term and weak magnetism) from the spectrum shape, is $\sim 5 \times 10^{-3}$. These values will be significantly improved in a new setup, with an optimized scintillator geometry and better homogeneity of the energy response.

Beknpte samenvatting

Ondanks het vele onderzoek naar β -verval gedurende de 21e eeuw, zijn er nog steeds vele vragen die beantwoord kunnen worden door precisiemetingen op de energiedistributie van de uitgestuurde elektronen. De vorm van het β spectrum reflecteert niet enkel de zwakke interactie, verantwoordelijk voor het verval, maar ze is ook gevoelig aan de sterke interactie, die de participerende quarks samenhoudt in de atoomkern. De elektromagnetische kracht speelt hierin ook een rol aangezien de uitgezonden elektronen interageren met de geladen atoomkern. Hierdoor zijn metingen van het β spectrum een zeer nuttig middel om de interacties binnen het Standaard Model (SM) beter te begrijpen. Bovendien kunnen deze metingen een licht werpen op nieuwe fysica, als er verschillen worden waargenomen tussen de gemeten en verwachte spectrum vormen.

Eén van de open vragen is of de zwakke interactie Lagrangiaan werkelijk enkel Vector en Axiale-vector stromen toelaat. Metingen van het β spectrum kunnen een antwoord bieden op deze vraag, omdat de exotische stromen, d.w.z. stromen van een andere vorm dan 'Vector' of 'Axiale-vector', de vorm van het spectrum beïnvloeden via de zogenoemde Fierz term b . Om gevoelig te zijn aan deze 'nieuwe fysica' en te kunnen wedijveren met experimenten uitgevoerd aan de LHC in CERN, is een experimentele precisie van het niveau 10^{-3} noodzakelijk.

Wanneer precisie zo belangrijk is, wordt het succes van een experiment bepaald door het nauwgezet begrijpen van de systematische effecten. De grootste beperking in de precisie van een β spectrum meting zijn de eigenschappen van de energiegevoelige detector die gebruikt wordt in het experiment. Vooral de nauwkeurigheid waarmee de detector respons kan bepaald worden en de nauwkeurigheid van het theoretische model dat gebruikt wordt, zijn hierbij van belang. De miniBETA spectrometer was ontworpen om de β spectrum vorm te meten met een precisie van het 10^{-3} niveau. Het combineert een plastic scintillatie detector met een -met speciaal gas gevulde- dradenkamer, waar

de elektronen die door de bron worden uitgestuurd in drie dimensies kunnen getraceerd worden.

Door gebruik te maken van de plastic scintillatie detector kunnen de systematische effecten geïntroduceerd door het theoretische model geminimaliseerd worden. Bovendien wordt de kans dat de energie van het elektron volledig gedeponereerd wordt in de detector vergroot omwille van de kleine Z -waarde van het plastic. Hierdoor is de kans op processen als terugwaartse verstrooiing, remstraling en transmissie, immers minimaal, alsook de onzekerheid op de grootte van hun effect op het verwachte spectrum. Daarnaast zal het traceer algoritme deeltjes, die niet afkomstig zijn van de bron, filteren uit het opgemeten spectrum. Ten slotte laat de dradenkamer toe om terug-gestrooide elektronen te herkennen, waardoor dit effect nog verder gereduceerd wordt.

Deze thesis beschrijft de karakterisatie van de miniBETA spectrometer. Meerdere gasmengsels van helium en isobutaan werden getest als medium om deeltjes te traceren. Kalibraties van de dradenkamer respons werden gebaseerd op metingen van kosmische muonen. De gemiddelde efficiëntie voor het detecteren van een ioniserend deeltje in een enkele cel bereikte 0.98 voor mengsels bij 600 mbar en 0.95 bij 300 mbar. De ruimtelijke resolutie voor een enkele cel in het XY-vlak, bepaald door de drifttijd, werd voor dezelfde mengsels geschat op respectievelijk 0.4 mm en 0.8 mm. De ruimtelijke resolutie in het ZY-vlak, bepaald door het ladingsverschil aan weerszijden van de draad, werd geschat op een aantal mm. Een aantal correcties op systematische effecten werden onderzocht, zoals bv. een correctie op de positie shift van de afzonderlijke draden.

Er werd aangetoond dat het traceren van deeltjes de precisie van spectrum metingen verbeterde, mede door het feit dat de respons van de spectrometer afhankelijk is van de positie waar het deeltje de detector binnendringt. Een eerste kalibratie van de energie respons werd gedaan met een ^{207}Bi bron. Deze was gebaseerd op het fitten van het gemeten spectrum aan een gesimuleerd spectrum in combinatie met een convolutie. Met deze methode werd een resolutie van $\sigma_{1\text{MeV}} = 7.6\%$ gevonden voor het prototype. De onzekerheid op de conversieparameters die het bepalen van energieafhankelijke termen in het β spectrum, zoals de Fierz term en zwak magnetisme, verhindert, is $\sim 5 \times 10^{-3}$. Deze waarden zullen significant verbeteren in een nieuwe opstelling met geoptimaliseerde scintillatie detector en een betere homogeniteit van de energierespons.

Streszczenie

Jądrowy rozpad β badany jest już niemal od wieku, jednak wciąż pozostają pytania, na które można znaleźć odpowiedzi dzięki precyzyjnym pomiarom widma rozkładu energii emitowanych w rozpadzie elektronów. Na kształt widma β wpływają oddziaływania słabe, które odpowiadają za ten rozpad. Kształt ten jest również czuły na wpływ oddziaływań silnych, które wiążą rozpadający się kwark w nukleonie. Dodatkowo emitowany elektron oddziałuje elektromagnetycznie z naładowanym jądrem. Dlatego pomiary kształtu widma β są ważnym narzędziem służącym do zrozumienia wszystkich oddziaływań tworzących Model Standardowy (MS), a wysoka precyzja pomiarów jest wymagana, by rozwikłać wpływ poszczególnych oddziaływań. Co więcej, takie pomiary mogą przybliżyć nas do zrozumienia Nowej Fizyki (NF), jeśli wykażą istnienie różnicy pomiędzy widmem zmierzonym, a przewidywanym przez MS.

Jednym z otwartych pytań jest prawidłowość lagranżjanu oddziaływań słabych typu $V - A$. Pomiary widma β bezpośrednio dotyczą tego problemu, gdyż egzotyczne prądy (tj. inne niż V i A) wpływają na kształt widma poprzez tzw. interferencyjny człon Fierza b . Aby eksperyment był czuły na NF, wymagane jest, by precyzja pomiarowa była na poziomie 10^{-3} , co pozwoliłoby na konkurowanie z eksperymentami wysokich energii, przeprowadzanymi w Wielkim Zderzaczu Hadronów.

Kiedy stawką jest precyzja, sukces eksperymentu wymaga dokładnego poznania i zrozumienia występujących w nim niepewności systematycznych. Główne ograniczenie precyzji, z jaką wyznaczone jest widmo β , wynika z właściwości detektora energii, użytego w eksperymencie. W szczególności ważna jest dokładna znajomość odpowiedzi energetycznej tego detektora oraz modelu depozycji energii w aktywnej objętości detektora. Spektrometr miniBETA zaprojektowany został, by mierzyć widmo β z precyzją na poziomie 10^{-3} . Spektrometr ten łączy plastikowy scyntylator mierzący deponowaną w nim energię z wielodrutową komorą dryfową, w której w trzech wymiarach śledzone są elektrony emitowane z rozpadającego się źródła.

Użycie plastikowego scyntylatora zmniejsza efekty systematyczne związane z modelem depozycji energii w aktywnej objętości detektora. Dzięki niskiej liczbie atomowej Z plastiku oraz doborowi grubości detektora prawdopodobieństwo, że energia zostanie w całości zdeponowana w detektorze, jest największe. Utrzymanie prawdopodobieństwa pozostałych procesów (tj. rozproszenia wstecznego, emisji promieniowania hamowania, oraz przeniknięcia elektronu przez detektor) na niskim poziomie zmniejsza wpływ ich niepewności na modelowane spektrum. Śledzenie cząstek pozwala natomiast odfiltrować zdarzenia, które nie pochodzą od elektronów emitowanych ze źródła. Umożliwia również rozpoznawanie zdarzeń, w których nastąpiło rozproszenie wsteczne, dodatkowo zmniejszając jego wpływ na mierzone widmo.

W poniższej rozprawie opisano proces uruchomienia spektrometru miniBETA. Przebadano kilka mieszanek gazowych helu i izobutanu, w celu sprawdzenia ich przydatności w procesie śledzenia cząstek. Do skalibrowania odpowiedzi komory dryfowej wykorzystano miony kosmiczne. Średnia wydajność detekcji cząstki jonizującej w pojedynczej celi wyniosła 0.98 dla mieszanek pod ciśnieniem 600 mbar oraz 0.95 dla 300 mbar. Rozdzielczość przestrzenna pojedynczej celi, wyznaczona z czasu dryfu, osiągnęła odpowiednio 0.4 mm i 0.8 mm. Rozdzielczość wynikająca z metody podziału ładunku była gorsza o około rząd wielkości. Przebadano szereg poprawek służących zniwelowaniu efektów systematycznych, takich jak uwzględnienie przesunięcia pozycji drutu sygnałowego, czulej nawet na zmiany wynoszące 0.02 mm.

W rozprawie wykazano, że śledzenie cząstek poprawia precyzję pomiarów widma, co jest wynikiem zależności pomiędzy odpowiedzią spektrometru a pozycją gdzie cząstka trafiła detektor. Wykonano wstępną kalibrację odpowiedzi energetycznej spektrometru przy użyciu ^{207}Bi jako źródła. Kalibracja polegała na wyznaczeniu parametrów dopasowujących widmo zmierzone oraz uzyskane ze splotu wysymulowanego widma energii zdeponowanej w scyntylatorze z funkcją odpowiedzi spektrometru. Rozdzielczość energetyczna prototypowej konfiguracji spektrometru wynosi $\rho_{1\text{MeV}} = 7.6\%$. Niepewność parametru skalującego, która utrudnia wyznaczenie członów zależnych od energii (tj. członu Fierza oraz słabego magnetyzmu), wynosi $\sim 5 \times 10^{-3}$. Wartości te zostaną znacznie poprawione w kolejnej konfiguracji spektrometru, w której zoptymalizowano geometrię scyntylatora i która posiada lepszą jednorodność odpowiedzi energetycznej detektora.

Contents

Abstract	v
Beknopte samenvatting	vii
Streszczenie	ix
Contents	xi
1 Introduction	1
2 The Standard Model and beyond	3
2.1 Brief introduction to the Standard Model	3
2.2 Nuclear beta decay	5
2.3 Parity violation of the weak interaction	9
2.4 Beyond the Standard Model	11
3 The miniBETA experiment	15
3.1 Overview and experimental goals	15
3.2 Origins and evolution of particle tracking detectors	18
3.3 Operation principles of a drift chamber	21
3.3.1 Particle passing through matter	21

3.3.2	Major characteristics of the ionization process and electron drift in an electric field	25
3.4	Details of the miniBETA spectrometer setup	31
3.4.1	Spectrometer and the DAQ	31
3.4.2	Gas system	38
3.4.3	Control and analysis software	39
4	Initial tests of the chamber performance under different gas and voltage conditions	43
4.1	Overview	43
4.2	MiniBETA configuration	45
4.3	FASTER configuration	46
4.4	Results of the HV scans with the single detection plane	47
4.5	Summary and conclusions	53
4.6	HV settings for 10 planes configuration	56
5	Reconstruction of particle trajectory in the xy-projection	59
5.1	Overview	59
5.2	Determination of the drift time-to-radius relation	60
5.2.1	Principles of the trajectory fitting in the drift plane . .	60
5.2.2	Determination of x - and y -coordinates of the detected ionization position	62
5.2.3	Cosmic muons as the calibration source	63
5.2.4	Initial calibration	63
5.2.5	Iterative autocalibration procedure	65
5.3	Systematic errors affecting the drift time-to-radius relation . .	74
5.3.1	Correction of the “time walk” effect	74
5.3.2	Problem with trajectories parallel to traversed cell centers	77
5.3.3	Determination of t_0	78

5.3.4	Correction for the misalignment of signal wires	80
5.3.5	Effects correlated with the total height of a signal . . .	82
5.4	Results	86
5.4.1	Position resolution	86
5.4.2	Efficiency	87
5.4.3	Comparison of results obtained with different gas mixtures filling the chamber	91
6	Reconstruction of particle trajectory in the yz-projection	95
6.1	Overview	95
6.2	Charge division technique	95
6.2.1	Determination of the offset of the amplitude readout . .	96
6.2.2	Principles of the z -coordinate extraction	98
6.2.3	Experimental method for correcting the gain balance for preamplifiers	99
6.3	Particle tracking in the yz -projection	102
6.3.1	Determination of experimental corrections for the z - coordinate	104
6.3.2	Resolution of the hit positioning in the z -direction . . .	107
6.3.3	Efficiency of the tracking in the yz -projection	109
6.4	Summary	112
6.5	3D tracking	115
7	Towards measurements of the energy spectrum	121
7.1	Overview	121
7.2	Simulation of the energy spectrum	122
7.3	Positional dependency of the spectrometer response	123
7.4	Convolution-based method for calibrating the energy response of the spectrometer	127

7.5 Summary	131
8 Conclusions	133
A Tables of cell efficiencies	137
Bibliography	143

Chapter 1

Introduction

The miniBETA spectrometer was designed to improve knowledge about the beta spectrum shape of decaying isotopes in a region between 100 keV to a few MeV. This would allow getting a better understanding of the Standard Model (SM) or even of the physics beyond, by searching for the existence of a non-zero Fierz interference term. It would also permit a more precise determination of the weak magnetism factor.

The miniBETA is a prototypical, modular, reconfigurable, low-pressure and high transparency detector of ionizing particles. It allows for a 3D particle tracking, including backscattering detection, in a drift chamber volume. It also provides information about energy deposited in a plastic scintillator.

Coordinates of an ionizing particle trajectory, in a plane perpendicular to the direction of the wires stretched in the chamber, are determined through the typical operation mode of a multi-wire drift chamber (MWDC). Ionized electrons, created along the path of the particle, move in an electric field towards signal wires. Their drift times are translated into drift distances according to a drift time-to-radius relation. In addition, the coordinates along the wires are determined based on the charge division technique. Drifting electrons induce a current, detected at both ends of a wire. Heights of these signals are used to determine the position on the wire where the current was induced.

Due to its modularity, the setup allows for a relatively quick and easy exchange of its components (in case of a failure or in order to improve their performance). The design also simplifies changes in the geometry, e.g. changing the number of detection planes and the shape of cells they are forming or changing the type and position of an ionizing source mounted in the chamber.

A custom electronic data acquisition system (DAQ) was designed for this project, allowing for the readout of analog and digital signals coming from multiple outputs of the system and recording them in a form convenient for analysis. An individualized software with a graphical user interface (GUI) was programmed for the system. It provides an automatized, real-time monitoring and control of the experiment. Moreover, it increases the safety of the project, as it is able to turn off the high voltage and shut down the flow of a gas mixture when hazardous conditions are detected.

In addition, an analysis software with a GUI was developed. It provides a quick preview of the collected data, automatizes calculations required for the detector calibration in an initial phase of measurements and delivers results, such as the efficiency and the resolution of the tracking algorithm.

The thesis focuses on the performance of this prototypical setup. The system is described in detail. Methods of the data analysis are presented, with particular attention being paid to systematic effects, the understanding of which is crucial for the precision frontier. Results of commissioning measurements with several gas mixtures filling the drift chamber are presented. Additionally, areas where improvements can be made are highlighted and an outlook on the possible upgrades is provided.

Chapter 2

The Standard Model and beyond

2.1 Brief introduction to the Standard Model

The twentieth century began with two revolutionary theories. The first one was quantum mechanics originating from Max Planck's description of the black body problem. Planck showed that quantization of the radiation energy leads to the proper description of the energy spectrum emitted by a heated black body, which cannot be obtained on grounds of classical mechanics. Within years, the quantum mechanics became perceived as a very universal theory with a wide range of applications.

The second ground breaking theory was Einstein's special relativity, describing the relationship between space and time, based on two postulates: invariance of the physics laws in all inertial frames of reference and the speed of light in vacuum being constant, regardless of the motion of the light source or the observer.

Both of these theories ignited a belief, that there should exist an universal framework, able to describe all the fundamental laws of physics in an elegant way with a common language [1]. The Standard Model (SM) is currently the theory which, probably, leads us the closest to this goal, although the objective is not yet fulfilled [2, 3].

The SM catalogs all known elementary particles (Fig. 2.1) and provides unified tools for describing three out of the four known fundamental forces, i.e. the

electromagnetic, weak and strong forces but not gravity. The matter is made out of fermions (particles of a half-integer spin, following Fermi–Dirac statistics) and the forces are carried by bosons (integer spin, following Bose–Einstein statistics).

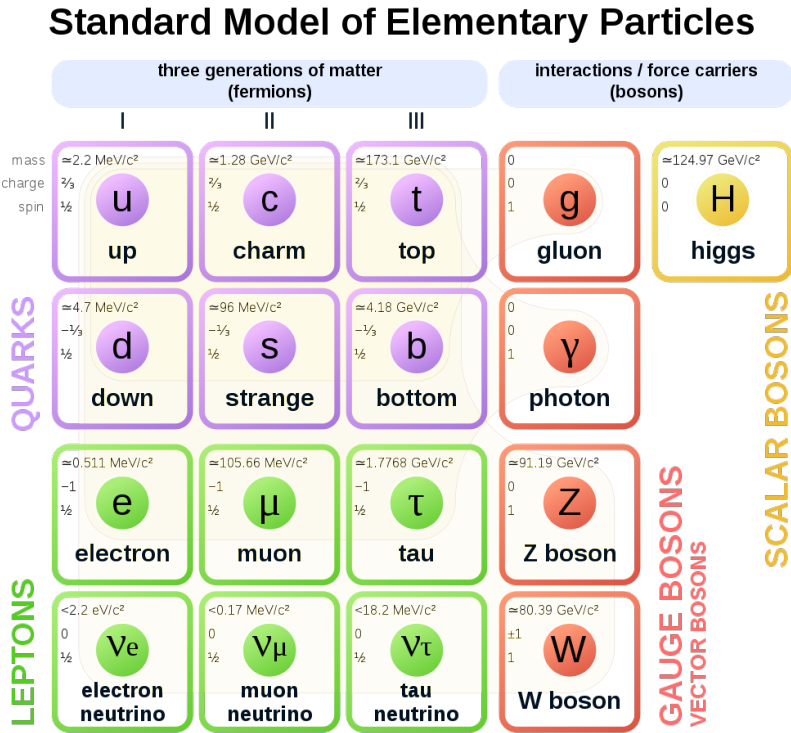


Figure 2.1: Elementary particles included in the Standard Model [4].

The electromagnetic force, carried by photons, is responsible for interactions between electrically charged particles and is described by quantum electrodynamics (QED). The weak force is carried by W^+ , W^- and Z bosons, and is responsible for interactions between leptons and quarks. It is the only force which can change a particle flavor, i.e. change a quark/lepton of one type into another one, e.g. in neutron/muon decays. The above forces are unified in the Glashow–Weinberg–Salam theory. The incorporated Higgs mechanism explains the origin of mass of the elementary particles.

The strong force binds the quarks and antiquarks together into hadrons and is mediated by gluons. These interactions are described by quantum

chromodynamics (QCD). As a residual effect, the strong force keeps protons and neutrons in atom nuclei. The SM merges all the above theories into one.

Despite being an extremely successful theory, the SM falls short in answering several questions. Just to mention a few of them:

- How is gravity added to the unified theory?
- Why are the SM predictions inconsistent with the cosmological observations, e.g. predominance of matter over antimatter?
- Where does dark energy come from?
- Is there an explanation behind the number and values of the model parameters?
- Why are no CP violating processes involving strong interactions observed?

2.2 Nuclear beta decay

The nuclear beta decay is a general term, which refers to three subtypes of nuclear processes:

- β^- decay: ${}_Z^AX \rightarrow {}_{Z+1}^AX' + e^- + \bar{\nu}_e$;
- β^+ decay: ${}_Z^AX \rightarrow {}_{Z-1}^AX' + e^+ + \nu_e$;
- electron capture: ${}_Z^AX + e^- \rightarrow {}_{Z-1}^AX' + \nu_e$;

where A and Z are mass and atomic numbers of an isotope X and e^- , e^+ , ν_e , $\bar{\nu}_e$ refer to electron, positron, electron neutrino, and electron antineutrino, respectively.

Henri Becquerel was the first who discovered the existence of spontaneous radiation, emitted from uranium salts themselves, without being excited by any external factor. At first, he thought that his radiation is a kind of an X-ray, found earlier that year. However, soon he realized that these rays are of a different type, as they can be deflected by electric or magnetic fields, whereas X-rays were neutral [5].

The radiation particles were classified by Ernest Rutherford according to their penetration abilities into alpha (α), beta (β) and gamma (γ) rays [6] and were explained as being a product of spontaneous transmutation of elements. By

studying the mass-to-charge ratio Becquerel found that β particles are in fact electrons.

Distributions of kinetic energy of α and γ particles were found to be narrow, which corresponds to the fact that these particles carry the energy difference between the mother and the daughter nuclear states. However, the continuous spectrum of β energies was a mystery, as it seemed to contradict the law of conservation of energy. Moreover, the emission of only an electron would not conserve the angular momentum.

The solution to these problems was proposed by Pauli, suggesting that there are also “neutrons” in the nucleus, light particles with a mass similar to the one of an electron, with no electric charge and spin 1/2, which are emitted together with electrons during the β decay [7]. However, neutrons discovered by Chadwick, were of the mass of protons, hence not fitting Pauli’s explanation.

The problem was solved by Fermi [8, 9]. He named the mysterious particle neutrino, to stress its tiny mass that has to be zero or much smaller than the electron mass. Fermi formulated a theory of the beta decay based on three assumptions (citing Fermi):

- i *The total number of electrons, as well as neutrinos, is not necessarily constant. This possibility, however, is not analogous to the creation or annihilation of an electron-positron pair.*
- ii *The heavy particles (neutrons, protons) may be treated (as by Heisenberg) as two internal quantum states of the heavy particle.*
- iii *The Hamiltonian function of the system consisting of heavy and lightweight particles must be chosen that each transition from a neutron to a proton is associated with the creation of an electron and a neutrino. The reverse process (change of a proton into a neutron) must be associated with the annihilation of an electron and a neutrino. Note that by this, conversion of charge is assured.*

Fermi constructed the Hamiltonian of the neutron decay:

$$n \rightarrow p + e^- + \bar{\nu}_e$$

by summing energies of the heavy (H_p, H_n) and the light (H_e, H_ν) particles involved and adding a term describing interactions between the particles. The general Hamiltonian for this reaction can be written as [10]:

$$H_F = H_p + H_n + H_e + H_\nu + \underbrace{\sum_i C_i \int d^3x (\bar{p}\hat{O}_i n)(\bar{e}\hat{O}_i \nu)}_{\text{interaction term}} \quad (2.1)$$

Table 2.1: Elementary fermion transition operators.

\hat{O}_i	Transformation property of $\bar{\psi}\hat{O}_i\psi$	Number of matrices
1	Scalar (S)	1
γ^μ	Vector (V)	4
$\sigma^{\lambda\mu} = \frac{1}{2}[\gamma^\lambda, \gamma^\mu]$	Tensor (T)	6
$\gamma^\mu\gamma_5$	Axial-vector (A)	4
$\gamma_5 = -i\gamma_0\gamma_1\gamma_2\gamma_3$	Pseudoscalar (P)	1

In this equation \bar{p} , n , \bar{e} and ν are wave functions of the corresponding particles or their (Dirac) adjoints $\bar{\psi} = \psi^\dagger\gamma^0$ and \hat{O}_i are appropriate operators characterizing the decay and weighted by constants C_i . Due to the relativistic character of the decay, the wave functions have to be solutions of the Dirac equation, i.e. four-component spinors, hence the operators \hat{O}_i must be 4×4 spin matrices.

Since the interactions are integrated over the spatial coordinates and the Hamiltonian transforms like the time component of the four-momentum vector, the terms in the integrals have to be Lorentz scalars. This means that $\bar{\psi}\hat{O}_i\psi$ must be well behaved under Lorentz transformations. It can be shown [10], that there are exactly 16 of these operators, which are defined in Tab. 2.1, with the use of Dirac matrices γ^μ .

The terms in the interaction follow the current-current coupling, known from electrodynamics, hence they are named currents with a prefix corresponding to the transformation property, e.g. $\bar{\psi}\sigma^{\lambda\mu}\psi$ is called tensor current. The original interaction proposed by Fermi only included the V type operator. The interaction was modified by Gamow and Teller [11], to include a possibility of a spin change, which had been experimentally observed in transitions of the thorium family. This was obtained by adding the A operator to the interaction.

In Fermi's theory, the weak interaction is of a contact type: four fermions interact directly with one another. However, this description becomes invalid at energies ~ 100 GeV and higher where the true nature of the process starts to emerge. In the electroweak theory, the four-fermion contact interaction is replaced by an exchange of a W^+ , W^- or Z boson. For lower energies, due to high masses of these bosons ($m_{W^\pm} = 80.4$ GeV and $m_Z = 91.2$ GeV), weak interaction can be approximated as a contact type. Figure 2.2 presents the leading-order Feynman diagram for β^- decay of a neutron via an intermediate W^- boson.

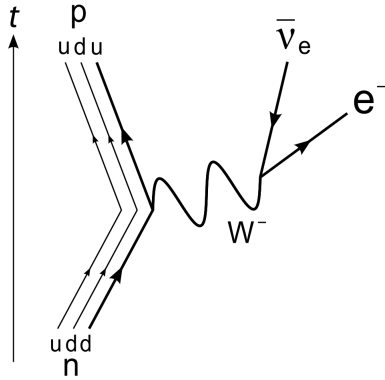


Figure 2.2: The leading-order Feynman diagram for β^- decay of a neutron via an intermediate W^- boson.

Table 2.2: Selection rules and observed ranges of $\log ft$ values for nuclear β decay [12].

Decay type	ΔJ	ΔT	$\Delta\pi$	$\log ft$
Superaligned	$0^+ \rightarrow 0^+$	0	no	3.1-3.6
Allowed	0,1	0,1	no	2.9-10
First forbidden	0,1,2	0,1	yes	5-19
Second forbidden	1,2,3	0,1	no	10-18
Third forbidden	2,3,4	0,1	yes	17-22
Fourth forbiddeb	3,4,5	0,1	no	22-24

Beta decays are divided into allowed and forbidden transitions according to their probability, which depends on the change of the angular momentum ΔJ , parity $\Delta\pi$, and isospin ΔT between the initial and the final nuclear states (Tab. 2.2). The degree of forbiddenness of the transition is also reflected in the ft -value (also known as the comparative half-life), defined as a product of the corresponding Fermi integral f , which depends on the kinematics of the decay, and the half-life $T_{1/2}$ of the transition. Because ft -values span many orders of magnitude, it is often more convenient to use $\log ft$.

2.3 Parity violation of the weak interaction

At first, conservation of parity P was assumed to be a general law of nature, valid for all interactions, since it was firmly established for strong and electromagnetic processes [7]. Observed beta decays were either Fermi or Gamow-Teller type (sensitive only to V or only to A), hence the existing belief that the weak interaction also has to be invariant under space inversion.

The problem appeared when the decay of K^+ mesons was discovered. It was found that its product can consist of two ($\pi^+ + \pi^0$) or three ($\pi^+ + \pi^+ + \pi^-$) pions, which would lead to a different parity $P = +1$ and $P = -1$ respectively. Since this seemed impossible, it was believed that what was observed was actually a decay of two different particles: τ^+ and θ^+ . But experimental measurements indicated that this had to be the same particle, as no differences were found between masses and lifetimes of the initial states.

The problem was called τ - θ puzzle and was finally resolved by T. D. Lee and C. N. Yang, when they realized that “*parity conservation (in weak interaction processes) is so far only an extrapolated hypothesis unsupported by experimental evidence*” and proposed the most general form of Hamiltonian, not limited by parity conservation [13]:

$$\begin{aligned}
 H_{int} = & (\bar{p}n)[\bar{e}(C_S + C'_S\gamma_5)\nu] \\
 & + (\bar{p}\gamma_\mu n)[\bar{e}\gamma_\mu(C_V + C'_V\gamma_5)\nu] \\
 & + \frac{1}{2}(\bar{p}\sigma_{\lambda\mu}n)[\bar{e}\sigma_{\lambda\mu}(C_T + C'_T\gamma_5)\nu] \\
 & - (\bar{p}\gamma_\mu\gamma_5 n)[\bar{e}\gamma_\mu\gamma_5(C_A + C'_A\gamma_5)\nu] \\
 & + (\bar{p}\gamma_5 n)[\bar{e}\gamma_5(C_P + C'_P\gamma_5)\nu] + \text{h.c.},
 \end{aligned} \tag{2.2}$$

Coupling constants C_i and C'_i are in general complex. However, they can be confined by general symmetries [14]. Invariance under time-reversal T requires all the constants to be real. Parity P is not violated if only one constant from a (C_i, C'_i) pair is present (i.e. $C_i = 0$ or $C'_i = 0$). Charge conjugation C is invariant if the C_i are real and the C'_i are purely imaginary, up to an overall phase.

Numerous experiments showed, with the most famous one being the Wu experiment [15], that only a single helicity λ (projection of the spin onto the direction of momentum) can be observed: e^- and ν are always created with $\lambda = -1$ (left-handed), while e^+ and $\bar{\nu}$ are always created with $\lambda = +1$ (right-handed). This means that parity is violated in the maximal way and the

only possible combination of coupling is of a type $V - A$. This fact was included in the Standard Model, where the complete interaction is described by:

$$H_{int,SM}(n, p, e, \nu) = \int d^3x [\bar{p}\gamma^\mu(C_V + C_A\gamma_5)n] \quad (2.3)$$

$$\times [\bar{e}\gamma_\mu(1 - \gamma_5)\nu],$$

where C_V and C_A are real constants, $C_V = 0.98558(11) G_F/\sqrt{2}$ and $C_A/C_V = -1.27510(66)$ [16]. These values are a result of the Standard Model fit ($C'_V = C_V$, $C'_A = C_A$, $C'_S = C_S = C'_T = C_T = 0$) to the existing experimental β -decay data. The data was restricted to the most sensitive measurements, i.e. $\mathcal{F}t$ -values (corrected ft -values, including nuclear structure and radiative corrections) of super-allowed $0^+ \rightarrow 0^+$ transitions and selected data from neutron decay. The Fermi coupling constant, $G_F/(\hbar c)^3 = 1.1663787(6) \times 10^{-5} \text{ GeV}^{-2}$ [17], is derived from the muon lifetime.

The difference between the values of coupling constants present in the SM is believed to result from the axial-vector operator being modified in the presence of the strong interaction [12]. The axial-vector is only partially conserved (PCAC - partially conserved axial-vector current), which means its divergence is non-zero, as opposed to the vector current, which is conserved (CVC - conserved vector current):

$$\text{CVC} : \sum_{\mu=1}^4 \frac{\partial V_\mu}{\partial x_\mu} = 0, \quad (2.4)$$

$$\text{PCAC} : \sum_{\mu=1}^4 \frac{\partial A_\mu}{\partial x_\mu} = a\phi_\pi,$$

where ϕ_π represents the pion field and a is a constant. This indicates that the weak axial-vector current is related to the strong interaction field through PCAC. Measurements of superallowed transitions agree with CVC: all superallowed transitions have the same $\mathcal{F}t$ -values within statistical uncertainties. A review and interpretation of these measurements can be found in [18].

Weak magnetism is one of the so-called induced coupling constants, which have to be included in the interaction term when high accuracy is required. In the SM picture, at the fundamental level, the β^- decay is caused by conversion of d quark to u quark by emission of W^- boson, decaying into e^- and $\bar{\nu}$. However, quarks are confined in the nucleus by the strong force and the decaying quark is interacting with the other two. To include this fact one has to write the vector

and axial-vector currents in the hadronic form [19]:

$$V_\mu^h = \bar{p} \left[g_V(q^2) \gamma_\mu + f_M(q^2) \sigma_{\mu\nu} \frac{q_\nu}{2M} + i f_S(q^2) \frac{q_\mu}{m_e} \right] n \quad (2.5)$$

$$A_\mu^h = \bar{p} \left[g_A(q^2) \gamma_\mu \gamma_5 + f_T(q^2) \sigma_{\mu\nu} \gamma_5 \frac{q_\nu}{2M} + i f_P(q^2) \frac{q_\mu}{m_e} \gamma_5 \right] n \quad (2.6)$$

In these expressions $q_\mu = (p_i - p_f)_\mu$ is the four-momentum transfer and M and m_e are the nucleus and the electron masses. The form factors $g_V, g_A, f_i (i = M, S, T, P)$ are arbitrary functions of the Lorentz scalar q^2 and, in the limit of zero-momentum transfer, $q^2 \rightarrow 0$, are called the vector, axial-vector, weak magnetism and induced scalar, induced tensor and induced pseudoscalar coupling, respectively. The induced couplings are dominated by weak magnetism and its inclusion is typically sufficient to be accurate down to the 10^{-3} level [20].

2.4 Beyond the Standard Model

There are no fundamental reasons, beyond purely experimental results, why only C_V and C_A coupling constants are non-zero in the SM. Measuring a non-zero value of C_S , C_T or C_P would directly require a correction to the current form of the SM or could even lead to development of new physics theories. Jackson, Treiman and Wyld proposed several possible tests for the validity of the invariance under time reversal (T symmetry) for allowed beta decay processes [21, 22]. Tests are based on several distribution functions with respect to momenta and spins of the decaying system and their sensitivity to the coupling constants not included in the SM.

A recent review by M. González-Alonso, O. Naviliat-Cuncic and N. Severijns covers in detail the status of tests of the standard electroweak model and of searches for new physics in allowed nuclear β decay and neutron decay, including both theoretical and experimental developments [16]. It also shows that the β spectrum shape is an interesting observable, sensitive to new physics. The leading-order expression for the β -energy from the differential distribution from oriented nuclei is given by:

$$W(E_e) dE_e = \frac{F(\pm Z, E_e)}{2\pi^3} p_e E_e (E_0 - E_e)^2 dE_e \xi \left(1 + b \frac{m_e}{E_e} \right). \quad (2.7)$$

In the equation E_e, p_e and m_e are the total energy, momentum and mass of the electron and E_0 is the maximum total electron energy. The term $F(\pm Z, E)$, which depends on the atomic number Z , is the Fermi function encoding the dominant Coulomb correction and the upper (lower) sign refers to β^- (β^+)

decay. The overall factor ξ depends on M_F and M_{GT} , which are Fermi and Gamow-Teller matrix elements and on the Lee-Yang coupling constants $C_i^{(\prime)}$:

$$\begin{aligned} \xi = & |M_F|^2 [|C_V|^2 + |C'_V|^2 + |C_S|^2 + |C'_S|^2] \\ & + |M_{GT}|^2 [|C_A|^2 + |C'_A|^2 + |C_T|^2 + |C'_T|^2]. \end{aligned} \quad (2.8)$$

The factor b is called Fierz interference term and is defined by:

$$\begin{aligned} b \times \xi = & \pm 2\gamma \operatorname{Re} [|M_F|^2 (C_S C_V^* + C'_S C_V'^*) \\ & + |M_{GT}|^2 (C_T C_A^* + C'_T C_A'^*)], \end{aligned} \quad (2.9)$$

where $\gamma = \sqrt{1 - \alpha^2 Z^2}$ and α is the fine structure constant.

The Fierz term is often given by:

$$b \approx \pm \frac{1}{1 + \rho^2} \left[\operatorname{Re} \left(\frac{C_S + C'_S}{C_V} \right) + \rho^2 \operatorname{Re} \left(\frac{C_T + C'_T}{C_A} \right) \right], \quad (2.10)$$

where:

$$\rho = \frac{C_A M_{GT}}{C_V M_F}, \quad (2.11)$$

is the Fermi/Gamow-Teller mixing ratio. For pure Fermi transitions $\rho = 0$ and for pure Gamow-Teller transitions $\rho \rightarrow \infty$. This notation directly shows that measuring nonzero Fierz coefficient would require the existence of either scalar or tensor (or both) interactions depending on the mixing ratio of the transition. These exotic interactions would require expanding the SM with new bosons being able to mediate them. As an example, scalar type interactions in β decay could be generated by a new, charged Higgs boson and scalar or vector leptoquarks (bosons coupling to quark-lepton pairs which carry lepton numbers, baryon numbers, and fractional charges). The exchange of scalar leptoquarks could also give rise to tensor couplings in β decay [19, 23, 24].

In the Standard Model $b = 0$. By measuring the β decay spectrum X_M and calculating its ratio with the spectrum given by the SM X_{SM} :

$$\frac{X_M}{X_{SM}} = 1 + b \frac{m_e}{E_e}, \quad (2.12)$$

one obtains an observable sensitive to new physics, where b is simply determined as the slope of the linear function of $(1/E_e)$. A precision of the order 10^{-3} is required if one wants to improve existing limits on the coupling constants beyond the SM [16, 23]. The best sensitivity to the Fierz term is achieved for decays with endpoint energies around 1-2 MeV, as was recently shown [25].

Before claiming the discovery of physics beyond the SM, one has to be sure, however, that the physics already included in the SM is well understood. This requires an even better description of the β spectrum, preferably reliable at the 10^{-4} level. Currently, the best and fully analytical description of the allowed β spectrum shape is provided by L. Hayen et al. [20,26], which is accurate to a few parts in 10^{-4} down to 1 keV for low- to medium- Z nuclei. Furthermore, authors stress the need for an accurate evaluation of weak magnetism contributions, as they are often the limiting factor of the precision. The weak magnetism is $\propto E$ and lack of its proper knowledge can hinder the extraction of the Fierz term contribution.

Chapter 3

The miniBETA experiment

3.1 Overview and experimental goals

The main goal of the miniBETA experiment is to measure the beta spectrum shape of interesting isotopes with a precision at the level of 10^{-3} for energies in the range from 100 keV to a few MeV. This level of precision is required if one would like to investigate the existence of the Fierz interference term, which expands the weak interactions with couplings not included in the Standard Model [16, 23, 25, 27, 28]. In addition, the influence of the weak magnetism has to be measured as well. Although the weak magnetism is part of the Standard Model, its coefficients are currently known only with a percent level precision, which is a limiting factor for high-precision spectrum shape analyses [20]. Moreover, the better knowledge about the weak magnetism is important also in the scope of the reactor neutrino anomaly [29].

When precision is at stake, the proper understanding of systematic errors becomes a key factor determining the success of an experiment. The aim of the miniBETA design was to establish and limit the influence of processes in which energy is not fully deposited in the spectrometer. The particle has to be fully stopped, which requires a certain thickness of the detector material. In the interaction of electrically charged particles with matter a part of the energy can be lost with a bremsstrahlung photon leaving the detector volume. Moreover, the electron can bounce back from the detector in a backscattering process, leaving there only a part of its energy. In general, the influence of all of these scenarios on the spectrum shape can be simulated, although the probability of

their occurrence is known with limited precision, which degrades the overall spectrum shape precision [30].

A plastic scintillator was chosen as the energy detector for the miniBETA spectrometer. It may seem like an unfortunate decision, since the energy resolution of organic scintillators is inferior to the one of other materials, e.g. high purity germanium (HPGe). However, simulations showed that the worse resolution of a scintillator has a small impact on uncertainties of the weak magnetism and Fierz term, extracted from a spectrum shape [30]. Therefore, using a scintillator instead of a HPGe is advantageous, as it decreases probabilities of backscattering and bremsstrahlung by an order of magnitude, due to the low atomic number Z of plastic (Fig. 3.7).

The chamber operates with a helium-based gas mixture at lower than atmospheric pressure. Thanks to the low mass and the low Z of the mixture the in-gas scattering and energy losses are limited [31–33]. The hexagonal shape of the drift cells reduces the number of wires required for shaping the electric field, increasing transparency of the chamber and cutting down the on-wire scattering probability [34].

Further reduction of the backscattering is achieved by an ability to track electrons in three dimensions in the multi-wire drift chamber (MWDC), that is part of the setup. A reconstructed event, where two trajectory lines are crossing at the scintillator surface, can be flagged and excluded from the spectrum shape analysis. Scattering events are interesting on their own, however. With minor modifications, like addition of a scatterer, the system can be focused on gathering experimental data that could lead to an improvement of the scattering model [30].

Particle tracking also increases the overall energy resolution of the scintillation detector. The light collection efficiency depends on the position where the scintillator was hit, due to the geometrical effects in the light transport from the scintillator, through the light guide, to the photomultiplier tube (PMT). This causes the detector response to depend on the hit position. Extrapolating a particle trajectory to the scintillator allows for correcting the energy readout for this effect. Moreover, the requirement for detecting a good trajectory in the chamber filters the spectrum from gammas and radiation not originating from the source.

A custom data acquisition system (DAQ) was developed for the spectrometer [34]. Modules equipped with analog and digital cards are the main blocks of the DAQ. Each module is responsible for the readout of a single signal plane. Whenever a signal is detected on a sense wire in coincidence with a signal from the scintillator, information about the corresponding drift time and heights of

signals from both ends of the wire is recorded. The tracking algorithm uses these values to calculate 3D trajectories of the ionizing particles passing the chamber.

The whole system is designed in a modular way that allows for a relatively easy exchange and modification of its constituents, e.g. the number and configuration of signal planes or the type and dimensions of the energy detector. The compact size of the spectrometer simplifies its transportation, allowing for a potential usage in on-line experiments, where betas from short-lived isotopes can be measured directly on-site.

Several other approaches are also being used in experiments looking for New Physics, aiming at precision $\leq 10^{-3}$ for the Fierz term. Calorimetric technique involves implanting radioactive isotopes (e.g. from ${}^6\text{He}$ beam) deep in a scintillating detector (e.g. NaI(Tl) , CsI(Na)) [35, 36]. This approach ensures 4π geometry and eliminates uncertainty related to backscattering.

Nab collaboration is using a so-called field-expansion spectrometer [37]. Trajectories of electrons and protons from neutron decays are confined by a magnetic field, which guides them towards 2 segmented Si detectors. This approach also provides detection in 4π . Similar segmented Si detectors are being used in Los Alamos National Lab to measure the spectrum shape of ${}^{45}\text{Ca}$ [38]. This setup also uses a magnetic field to confine electrons' trajectories.

NoMoS: the neutron decay products momentum spectrometer is a novel method of momentum spectroscopy. It utilizes the $R \times B$ drift effect to disperse charged particles dependent on their momentum in a uniformly curved magnetic field. This spectrometer is designed to precisely measure momentum spectra and angular correlation coefficients in free neutron beta decay [39].

The very unique approach is presented by Project8 collaboration, which plans to use cyclotron radiation emission spectroscopy from single electrons orbiting in a magnetic field [40]. A review of experiments serving as high precision probes for New Physics can be found in [16, 28].

3.2 Origins and evolution of particle tracking detectors

An analysis of a particle trajectory is one of the essential tools of the particle physics. Knowing its range in a given medium, curvature in a magnetic field and points where it started and ended allows identifying the type of particle, its momentum, and the origin. Charged particle trajectories were observed for more than a century thanks to Charles T. R. Wilson, who discovered that ions could act as centers for water droplet formation in the expansion cloud chamber. His detector was a sealed chamber with air, which was saturated with water vapor and adiabatically cooled by expanding its volume, causing the vapors to condensate. In such conditions, a charged particle leaves a visible trail as the vapors condense on ions produced along the particle path. Wilson was awarded the Nobel Prize in Physics in 1927 “*for his method of making the paths of electrically charged particles visible by condensation of vapor*”. Cloud chambers led, inter alia, to the discoveries of the positron (1932, Nobel Prize in 1936, Fig. 3.1) and the muon (1936) by Carl Anderson.

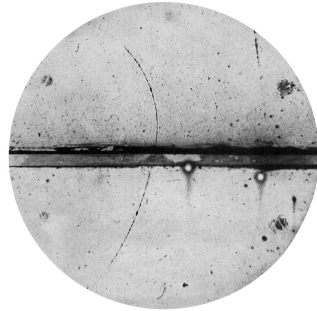


Figure 3.1: The first picture of the positron in a vertical Wilson chamber [41].

The ionization proces was also used by Donald A. Glaser in the bubble chamber he invented, for which he received the Nobel Prize in 1960. This chamber was filled with a superheated fluid, initially ether, in which ionizing particles leave bubbles along their trajectory and the bubble density is proportional to the energy loss. Bubble chambers allowed for the observation of processes involving weak neutral currents at Gargamelle in 1973 [42], showing the validity of the electroweak theory. The detector requires photographic readout, which makes the data analysis less convenient, especially when great statistics is required. Moreover, the liquid in the chamber requires recompression in order to eliminate the existing bubbles, which significantly reduces the rate of detection. Just to compare numbers: current experiments at the Large Hadron Collider (LHC) record the same number of events in less than 2 hours, as the Big European Bubble Chamber (BEBC), also at CERN, recorded during its 11 years operation (6.3 million pictures).

The next step in the ionization chamber evolution required higher rates for collecting the data, which has lead to the development of spark chambers. They

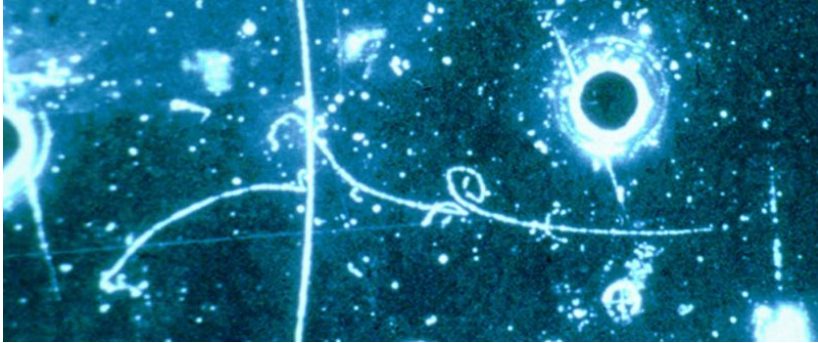


Figure 3.2: Electron-neutrino interaction registered in the Gargamelle bubble chamber that provided the first confirmation of a neutral current interaction [43].

are typically filled with a noble gas, e.g. helium or neon, and constitute of stacked metal plates with insulating spacers in between (~ 1 cm). A strong electric field between the plates causes a spark to appear along the trail of ionized gas left by an ionizing particle. Spark chambers require an additional triggering detector, e.g. pair of scintillators, which act as a fast switch delivering the high voltage to the planes, whenever an ionizing particle passes the setup, as a permanent field would cause arc formation and continuous discharging. A closely related detector, a streamer chamber, was the first one which recorded proton-antiproton interactions in CERN [44] (Fig. 3.3). The spatial resolution of spark chambers was lower than the one of bubble chambers, typically $\sigma_x \sim 1$ mm.

The next breakthrough came with George Charpak and his invention and development of the multi-wire proportional chamber (MWPC) in 1968 [46] (Fig. 3.4), which granted him the Nobel Prize in 1992. The name comes from the fact that a MWPC consists of layers of wires at high potential, located in between cathode layers at low potential (usually grounded), where each wire acts as a proportional counter, meaning that the readout signal induced by drifting ions is proportional to the energy deposited along the particle's path in the ionization process.

Electronic readout of the signal is possible due to a multiplication of the charge in a Townsend avalanche. This process occurs in the strong electric field in the vicinity of the wire, increasing the number of electrons by a few orders of magnitude. Moreover, MWPCs were able to cope with detection rates of $\sim 10^4$ times greater than what was possible with bubble chambers. The spatial resolution of the MWDC depends on the spacing between the signal wires s : $\sigma_x = s/\sqrt{12}$ (≈ 0.29 mm for $s = 1$ mm). The resolution can be improved by measuring the arrival time of the pulses. Evaluation of this idea led to the

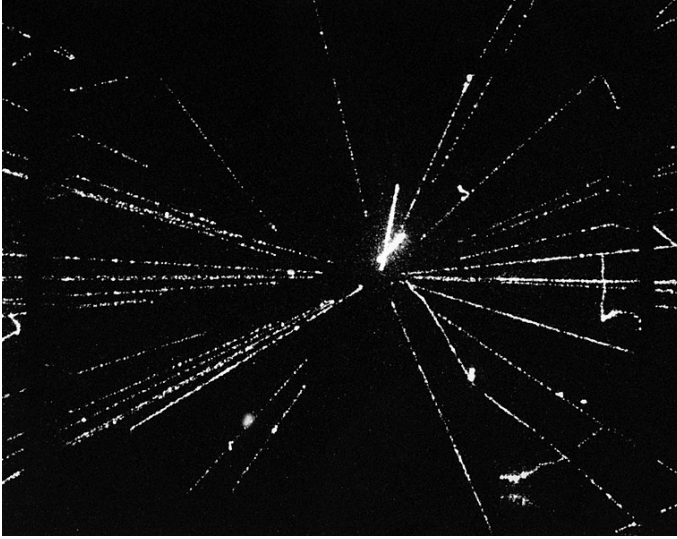


Figure 3.3: Particle trajectories in the UA5 streamer chamber resulting from the proton-antiproton interaction at 540 GeV [45].

development of drift chambers. Principles of their operation are explained in the following section.

The concept of using the ionization was further developed, branching into several detector types, like time projection chambers (TPC), micro-strip gas chambers (MSGC), GEM detectors and resistive plate chambers (RPC), just to mention a few. More details can be found in [17, 47–50]. Table 3.1 summarizes the properties of common particle detectors.

Table 3.1: Typical properties of common charged particle detectors [17].

Detector type	Intrinsic Spatial Resolution (rms)	Time Resolution	Dead Time
Resistive plate chamber	$\lesssim 10$ mm	1 ns	-
Streamer chamber	$300\ \mu\text{m}$	$2\ \mu\text{s}$	100 ms
Bubble chamber	$10\text{--}150\ \mu\text{m}$	1 ms	50 ms
Proportional chamber	$50\text{--}100\ \mu\text{m}$	2 ns	20–200 ns
Drift chamber	$50\text{--}100\ \mu\text{m}$	2 ns	20–100 ns
Micro-pattern gas detectors	$30\text{--}40\ \mu\text{m}$	<10 ns	10–100 ns

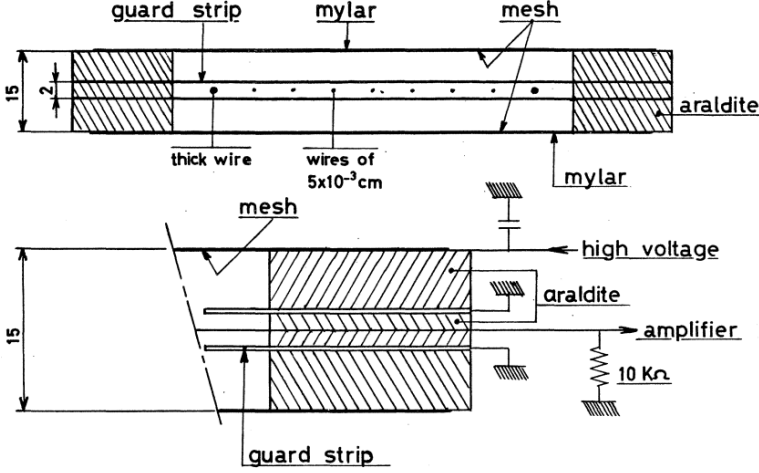


Figure 3.4: Some details of the construction of the multiwire chambers. A copper shield protects the wires at their output from the chamber, and contains the solid-state amplifiers [46].

3.3 Operation principles of a drift chamber

3.3.1 Particle passing through matter

When a charged particle passes through matter two things happen: the particle loses energy and is deflected from its original direction, which is caused by inelastic collisions with atomic electrons and elastic scattering off nuclei. In addition, energy can be lost due to bremsstrahlung and Cherenkov radiation. For heavy particles interactions can be practically limited to the inelastic collisions with atomic electrons. The process is described as a quantum mechanical transition between the field of the particle and the field created indirectly by the neighboring polarizable atoms. As a result, the medium is ionized along the particle path.

The equation describing the average energy loss per distance traveled $\langle dE/dx \rangle$ (also called the stopping power) by an energetic particle, heavier than the electron, is called Bethe formula [17]:

$$\left\langle -\frac{dE}{dx} \right\rangle = K z^2 \frac{Z}{A} \frac{1}{\beta^2} \left[\frac{1}{2} \ln \frac{2m_e c^2 \beta^2 \gamma^2 W_{max}}{I^2} - \beta^2 - \frac{\delta(\beta\gamma)}{2} \right], \quad (3.1)$$

where $K = 4\pi N_A r_e^2 m_e c^2$, N_A is the Avogadro's number, r_e is the classical electron radius, m_e is the electron rest mass, c is the speed of light, z is the

charge number of the incident particle, Z and A are the atomic number and the atomic mass of the absorber, $\beta = v/c$, v is the velocity of the incident particle, $\gamma = \sqrt{1 - \beta^2}^{-1}$ and $\delta(\gamma\beta)$ is the density effect correction. Bloch provided an approximation for the mean excitation energy $I \approx (10 \text{ eV}) \cdot Z$, although nowadays more accurate tables for this relation are available and used. W_{max} is the maximum energy transfer to an electron in a single collision:

$$W_{max} = \frac{2m_e c^2 \beta^2 \gamma^2}{1 + 2\gamma m_e/M + (m_e/M)^2}. \quad (3.2)$$

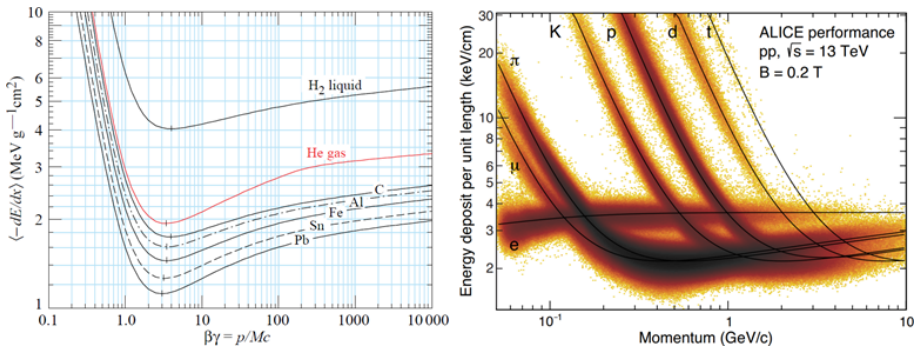


Figure 3.5: (Left) Mean energy loss rate in liquid hydrogen (bubble chamber), gaseous helium, carbon, aluminum, iron, tin, and lead. Radiative effects, relevant for muons and pions, are not included. These become significant for muons in iron for $\beta\gamma \geq 1000$, and at lower momenta for muons in higher- Z absorbers. (Right) Energy deposited versus momentum measured in the ALICE TPC [17].

The Bethe formula is fairly accurate (\sim a few percent) for intermediate- Z material, in the region $\beta\gamma \in (0.1, 1000)$. For lower energies, one has to apply shell corrections and for higher, the energy loss due to bremsstrahlung has to be considered. Figure 3.5 (left) presents the energy losses as a function of $\beta\gamma$ in several materials. A few characteristic regions can be distinguished:

- a sharp decrease up to $\beta\gamma > 1$, dominated by β^{-2} resulting from a classical mechanics derivation,
- a broad minimum at $\beta\gamma \approx 3.5$,
- a logarithmic rise, as the field of the particle flattens and extends due to the Lorentz contraction, which increases the influence of distant-collision;
- a saturation called the “Fermi plateau” caused by the “density effect” $\delta(\beta\gamma)$, depending on the medium density, which describes the shielding of

the particle field due to the medium polarization, limiting the effective range of interaction.

If the ionizing particle is an electron, some adaptations of the equation have to be made. The assumption that the energy loss is a small fraction of the incident energy is then no longer valid. Moreover, interacting electrons are indistinguishable in the quantum mechanical picture, which limits the W_{max} by $1/2$. By convention, energy loss is calculated for the faster one of the emerging electrons. Energy transfers in electron-electron scattering are described by the Møller cross section. The stopping power is obtained as the first moment of the Møller cross section divided by dx [17]:

$$\left\langle \frac{dE}{dx} \right\rangle = \frac{1}{2} K \frac{Z}{A} \frac{1}{\beta^2} \left[\ln \frac{m_e c^2 \beta^2 \gamma^2 \{m_e c^2 (\gamma - 1)/2\}}{I^2} + (1 - \beta^2) - \frac{2\gamma - 1}{\gamma^2} \ln 2 + \frac{1}{8} \left(\frac{\gamma - 1}{\gamma} \right)^2 - \delta \right]. \quad (3.3)$$

In order to calculate the stopping power of a mixture or a compound, one can use an approximation based on the Bragg additivity rule, where the total stopping power is a weighted sum of loss rates in the constituents weighted according to their weight fraction w_i :

$$\left\langle \frac{dE}{dx} \right\rangle = \sum w_i \left\langle \frac{dE}{dx} \right\rangle_i. \quad (3.4)$$

A charged particle trajectory deflects as the particle passes through matter (Fig. 3.6). The total deflection is a sum of numerous singular deflections, mostly due to Coulomb scattering from nuclei which is described by the Rutherford cross-section. Although most of the scattering is small-angle, hence the total deflection distribution around its mean is well covered by the Central Limit Theorem, the existence of big-angle deflections introduces non-Gaussian tails to the distribution. Molière's theory represents well these Coulomb scatterings [51].

The central 98% of the projected angular distribution of a relativistic heavy particle can be approximated by a Gaussian function with standard deviation given by Lynch & Dahl [52]:

$$\theta_0^{RMS} = \frac{13.6 \text{ MeV}}{\beta c p} z \sqrt{\frac{x}{X_0}} \left[1 + 0.038 \ln \left(\frac{x z^2}{X_0 \beta^2} \right) \right], \quad (3.5)$$

where p , βc and z are the momentum, velocity and charge number of the incident particle, x is the thickness of the scattering medium and X_0 is the tabularized radiation length.

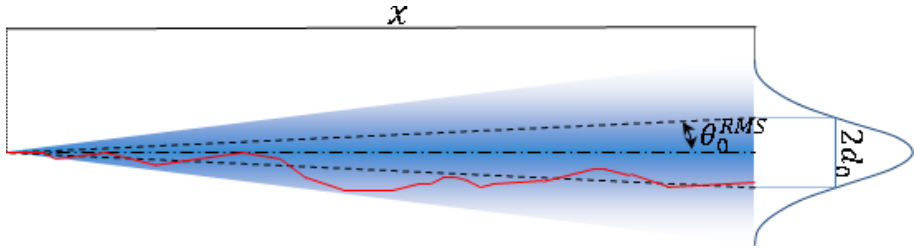


Figure 3.6: Visualization of the multiple-scattering process. The red line represents the single trajectory, and the shaded triangle the density of all trajectories. The planar angular distribution will have the root mean square θ_0^{RMS} and over the distance x will cause the displacement characterized approximately by the Gaussian distribution with the rms width d_0 .

Backscattering is a scattering process during which the particle changes its direction back to the half-sphere defined by the direction it came from, resulting in a picture where the particle bounces off the medium. Good understanding of this process is crucial for precise spectrum shape measurements, as backscattered particles deposit only part of their energy in the detector.

In practice, scattering distributions are obtained from simulations. However, a proper model is not always an obvious choice, as a compromise has to be made between single-scattering calculations, where each interaction is treated individually and multiple-scattering ones, based on the statistical approximations. Moreover, the models are precise only up to a few percents, which limits the precision of an energy spectrum shape measurement if the detector used reveals a high backscattering probability [30].

Generally, backscattering probability increases with the Z of the material [53]. Choosing a low- Z material limits the influence of backscattering on the spectrum shape, hence it can increase the precision of the experiment. A comparison between the probabilities for different outcomes (i.e. full-energy deposition, backscattering, bremsstrahlung, and transmission) when an electron hits a 3 mm high purity germanium (HPGe) and a 1 cm plastic (BC-400 from Saint-Gobain) detector is presented in Fig. 3.7.

The miniBETA spectrometer uses a plastic scintillator in combination with tracking of particles in a drift chamber, allowing for almost an backscattering-free measurement of the spectrum shape. To further reduce systematic effects influencing the experiment, the hexagonal cell shape was chosen, as it reduces the number of wires needed to form the required electric field, hence increasing the detection volume transparency, and limiting scattering on wires [34]. Moreover,

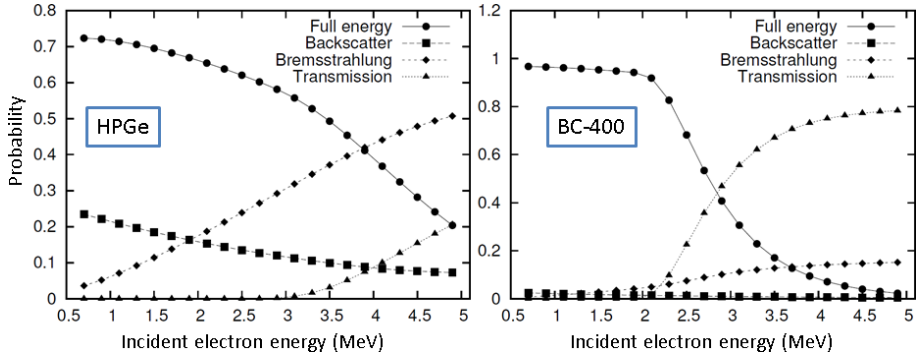


Figure 3.7: Probabilities of the different possible outcomes when an electron hits (left) a 3 mm thick slab of Ge and (right) a 1 cm thick plastic scintillator (BC-400 by Saint-Gobain) [30].

the gas mixture filling the chamber is based on helium. Due to its low mass and low Z (Tab. 3.2), energy losses are reduced and scattering is limited [31–33].

3.3.2 Major characteristics of the ionization process and electron drift in an electric field

Figure 3.8 presents an overview visualization of a β particle passing through a cell in the miniBETA drift chamber.

Ionizing encounters with the gas atoms along the particle path are purely random. The mean free path λ between these encounters is given by:

$$\lambda = 1/(\sigma_I N), \quad (3.6)$$

where σ_I is the ionization cross-section per electron and N is the number density of electrons in the medium:

$$N = N_A \frac{Z}{A} \rho, \quad (3.7)$$

described by the Avogadro's number N_A , the atomic number Z , the atomic weight A and the density ρ of the medium.

Along a path of length L there are by average $\langle N_I \rangle = L/\lambda$ encounters and the frequency distribution is Poissonian:

$$P(L/\lambda, k) = \frac{(L/\lambda)^k}{k!} \exp(-L/\lambda), \quad (3.8)$$

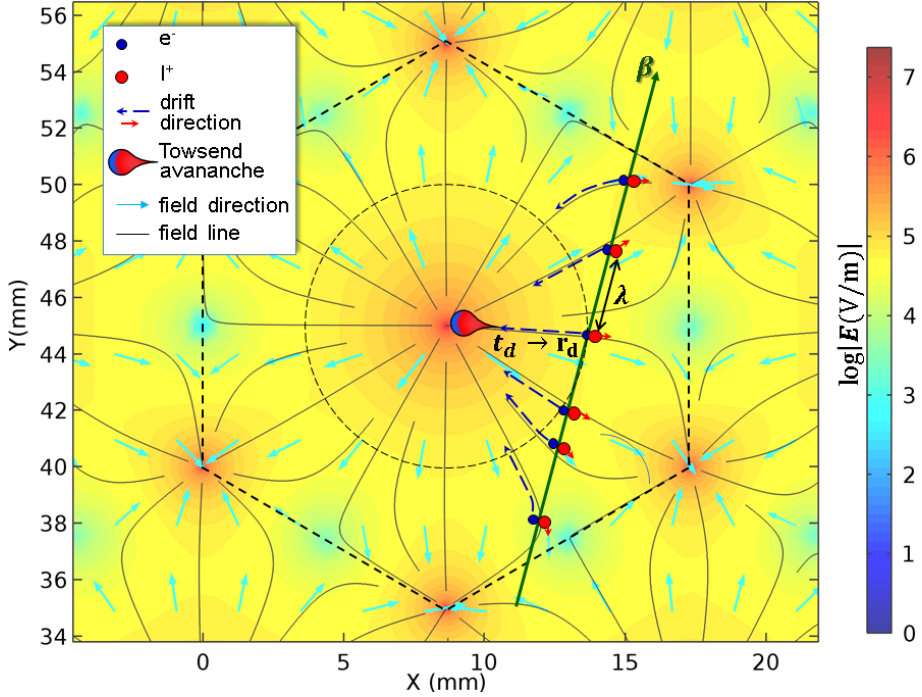


Figure 3.8: Simplified visualization of a β particle passing through the miniBETA drift cell, in the projection perpendicular to the alignment of the wires. The color in the background corresponds to the logarithm of the magnitude of the electric field strength $\log|E|$ calculated with COMSOL [54] for the actual dimensions and voltages used in the experiment [55]. Electrons e^- and positive ions I^+ are created along the particle path, with average interval λ between ionization clusters. Since the particle moves with relativistic velocity, the ionization happens instantaneously along the entire path. Then, electrons and ions move along the field lines in opposite directions. However, the ion's mobility is a few orders of magnitude lower, so their movement is neglected in this picture. When electrons approach the signal wire, their number is greatly multiplied in the Townsend avalanche, inducing a measurable current in the wire. The drift time t_d of the earliest electrons is recorded, and the drift distance r_d is calculated according to the drift time-to-radius relation (Eq. (3.12)).

leading to the exponential probability distribution $f(l)dl$ of the free flight paths l :

$$f(l)dl = (1/\lambda) \exp(-l/\lambda)dl. \quad (3.9)$$

Table 3.2: Properties of commonly used gases in drift chambers at normal conditions: ρ - density; E_x , E_I - first excitation, ionization energy; W_I - average energy per ion pair; $(dE/dx)_{mip}$, N_p , N_t - differential energy loss, primary and total number of electron-ion pairs per cm, for unit charge minimum ionizing particles [17]; X_0 - radiation length [31].

Gas	ρ (mg/cm ³)	E_x (eV)	E_I (eV)	W (eV)	$\frac{dE}{dx}$ (keV/cm)	N_p (cm ⁻¹)	N_t (cm ⁻¹)	X_0 (m)
He	0.179	19.8	24.6	41.3	0.32	3.5	8	5299
Ne	0.839	16.7	21.6	37	1.45	13	40	345
Ar	1.66	11.6	15.7	26	2.53	25	97	110
CO ₂	1.84	7.0	13.8	34	3.35	35	100	183
CH ₄	0.667	8.8	12.6	30	1.61	28	54	649
C ₂ H ₆	1.26	8.2	11.5	26	2.91	48	112	340
i-C ₄ H ₁₀	2.49	6.5	10.6	26	5.67	90	220	169

The mean free flight path λ can be obtained from experiments sensitive to a single electron detection, by measuring the inefficiency of detecting an ionization along the path L .

Besides the primary ionization, where few electrons are ejected from atoms in a single interaction with the passing particle, electrons can be additionally released due to secondary processes, which in practice constitute the majority of the total ionization. The ionized electron can have enough energy to free some more electrons. Moreover, if the medium is a mixture of at least two types of species an ionization can occur through intermediate excited states, where the energy from the excited atom or molecule (e.g. noble gas) is transferred to an object of the second type (e.g. quencher), with an ionization potential lower than the excitation energy of the first one [56]. Since multiple electrons are created in the single ionization in the vicinity of the encounter, the discussion most often refers to the behavior of electron clusters as objects of the analysis.

The nature of processes involved in the total ionization is not fully understood, hence experimental measurements are required for quantitative results. The medium is often characterized by the energy W_I that is spent on average on the creation of one free electron, regardless of the process. Table 3.2 presents properties of selected gases under normal conditions for minimum ionizing particles.

Velocities of primary electrons are mostly perpendicular to the particle track as their momentum is very small compared to the one of the particle. Electrons lose their kinetic energies in collisions with the medium particles, producing

secondary electrons and, because of their low mass, scattering isotropically. However, in the presence of the electric field \mathbf{E} , there is a peculiar direction, aligned with the field lines. Electrons are accelerated towards the high potential between each collision, resulting in the nonzero picked up velocity. The process of gaining and losing kinetic energy repeats resulting in the macroscopically observed drift velocity u :

$$u^2 = \frac{eE}{m_e N \sigma} \sqrt{\frac{\Delta}{2}}, \quad (3.10)$$

where e and m_e are the electron charge and mass, N is the number density of the medium, σ is the collision cross-section and Δ is the fractional energy loss per collision. If the energy picked up between collisions is lower than that of the medium excitation levels, the scattering is elastic and $\Delta \approx 2 \frac{m_e}{M} \sim 10^{-4}$, where M is the mass of the collision partner. Addition of compound molecules, like an organic quencher, dramatically increases the fractional energy loss due to the possibility of exciting their multiple rotational states, hence increasing the drift velocity u .

A point-like cloud of electrons in a cluster, created at $t = 0$, will diffuse after time t_d due to the randomness of scattering, increasing its size. It was discovered experimentally [57] that the diffusion is anisotropic, differentiating the direction \hat{z} along with the drift with a longitudinal diffusion coefficient D_L and perpendicular ones in \hat{x} and \hat{y} with a transverse diffusion coefficient D_T . The difference is explained by the fact, that D_L is affected by the variation of the electrons' mobility between the leading edge and the center of the traveling cloud [58]. The cloud density distribution n is given by:

$$n = \frac{1}{\sqrt{4\pi D_L t_d}} \left(\frac{1}{\sqrt{4\pi D_T t_d}} \right)^2 \exp \left[-\frac{x^2 + y^2}{4D_T t_d} - \frac{(z - ut_d)^2}{4D_L t_d} \right]. \quad (3.11)$$

Ions are much bigger and heavier than electrons, hence different processes determine their mobility. For the scope of this thesis, it is sufficient to say that their mobility is a few orders of magnitude smaller and depends less on the chamber operating conditions, like the field strength and the gas composition.

In the drift cell, the strength of the electric field is roughly inversely proportional to the distance r from the signal wire: $E \propto 1/r$. In the vicinity of the wire, approximately 5 times its radius, the field is high enough so that the energy obtained by the electron between collisions is sufficient to ionize additional electrons. The process is called Townsend avalanche and results in the number of electrons rising exponentially with each collision distance until the wire is reached. Due to the major difference in electron and ion mobility, the avalanche will have a drop-like shape, with half of the total ionization produced in the

last section between collisions with almost all the electrons in the head of the avalanche [49]. The multiplication factor depends on the gas composition and field strength. Figure 3.9 shows a general trend, how the total number of collected electrons depends on the voltage applied to the signal wire.

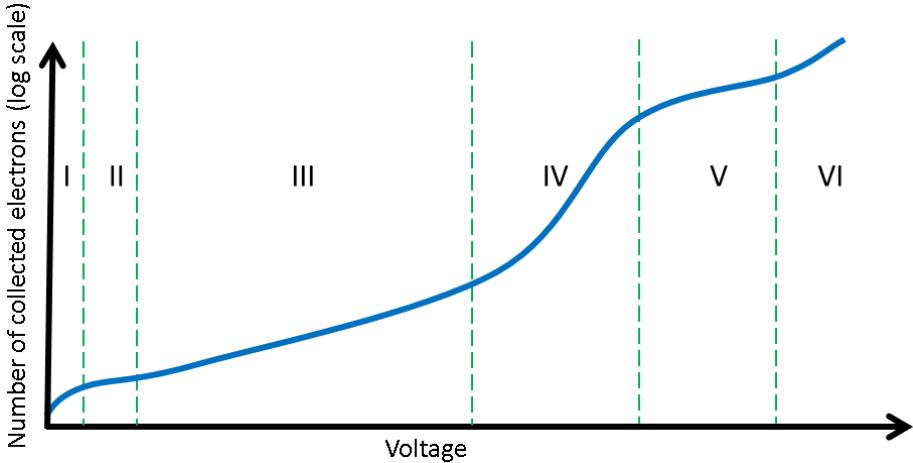


Figure 3.9: Illustrative relationship between the voltage applied to the signal wire and the number of collected ions. Roman numbers marks the characteristic operational modes, listed in the text.

There are 6 major regions that can be differentiated:

- I. Recombination region: part of the primary ionization is lost due to the recombination before reaching the wire.
- II. Ion saturation: recombination is suppressed and all the charges are efficiently collected.
- III. Proportionality mode: the field is strong enough to create the Townsend avalanche multiplying the collected charge. The charge is proportional to the number of original ion pairs, hence to the energy loss in the cell.
- IV. Limited proportionality: the number of ions created in the avalanche is so high, that they start to affect the shape of the electric field. Since their mobility is low, their presence significantly affects the consecutive events. This is called the space charge effect.
- V. Geiger-Möller mode: the space charge effect saturates the number of the created ion pairs. Photons created in the avalanche cause additional avalanches perpetually, making the particle tracking impossible.

VI. Gas breakdown region and arcs formation: operation in this region can cause irreversible damage to the chamber.

Gas mixtures based on noble gas with some addition of organic molecular quencher are a common medium used in drift chambers. Although the avalanche multiplication occurs in all gases, noble gases are preferred as they minimize energy losses in processes other than ionization, as e.g. excitation of molecules, so that a lower field is required to start the avalanche. However, a pure noble gas cannot serve as a good medium. It enters a permanent discharge region before reaching gas gain factors at a level required to produce a proper electronic signal. This is due to the other side of the coin: excited atoms of the noble gas (which are produced in abundance during the avalanche, when the produced ions collide with atoms), can return to the ground state only through a radiative process, producing UV photons. The noble gas is almost completely transparent to these photons, so that they can reach a cathode or the chamber walls releasing photoelectrons. Photoelectrons will drift back to the wire, causing additional avalanches. The whole process repeats resulting in a permanent discharge.

Even a small addition of polyatomic molecules can quench the continuous avalanches. Due to the high amount of non-radiative excited states, like rotational and vibrational states, quencher molecules can absorb UV photons, limiting their range, thus breaking the vicious cycle. Moreover, if the ionization potential of the quencher is lower than the excitation energy of the noble gas, the transfer is possible increasing the total ionization. This is called the Penning effect [48, 56, 59].

The moment t_d of the electrons arrival can be measured by monitoring the current in the signal wire since the movement of the charge in the electric field induces the current in the signal wire. The random nature of the energy losses, described by Eq. (3.8), results in multiple signals in time related to the arrival of electron clusters from different locations along the particle track. If the field has cylindrical symmetry, the earliest signal comes from the cluster which was created the closest to the wire. However, it is not guaranteed that the ionization happened at the point of closest approach of the trajectory. Because of this, the tracking positional resolution depends on the ionization density (primary ionization statistics).

Although choosing helium for the miniBETA gas mixture is beneficial from the spectroscopic point of view (argued in the previous section) it decreases the tracking resolution due to the high ionization potential of helium, and hence lowers the total number of ionization clusters created along the given path (Tab. 3.2). The downsides of He can be mitigated with a proper choice of the quenching gas, e.g. isobutane [32].

Operating at lower pressure further decreases the resolution as it lowers the electron density number N of the medium, which increases the mean free path λ between ionizing encounters (Eq. (3.6)) and increases the diffusion of the electron cloud (Eq. (3.11)). The positional resolution of the miniBETA drift chamber was compromised in favor of the spectroscopic goal of the miniBETA experiment.

Knowing the drift velocity u in the given conditions and the time the electrons drifted t_d , allows to calculate the distance r_d the electrons traveled in the cell:

$$r_d = \int_{t_0}^{t_d} u(t) dt. \quad (3.12)$$

Time t_0 refers to the moment when the ionization happened. In drift chambers t_0 is most often obtained from an external detector, e.g. scintillators, providing a fast signal when the ionizing particle passes the detection volume.

3.4 Details of the miniBETA spectrometer setup

3.4.1 Spectrometer and the DAQ

Figure 3.10 presents a scheme of the miniBETA detection chamber along with a picture of the system during the commissioning phase. The x -axis of the coordinate system used in the experiment is aligned with the numbering of wires on a plane, the y -axis correlates with the numbering of planes, and the z -axis is aligned with the orientation of the wires.

The detection chamber is built around an aluminum middle frame, attached to a support frame. The middle part is equipped with a source positioning system, which can move a source along x - and z -directions. Field (F) and signal (S) planes can be stacked on both sides of the middle part. A plane position is secured by metal rods, screwed to the middle frame, which passes through holes drilled along planes edges. Drift cells are formed by using a F-F-S-F-F-S-...-S-F-F pattern (Fig. 3.11, right). Planes are separated with aluminum spacers and O-rings in between. The spacers also provide rigidity to the system and the O-rings seal the chamber. Both sides of the chamber end with aluminum caps with mounted scintillators, light guides, and PMTs.

During the commissioning, the chamber was mostly operating in 0-10 configuration (with all the planes at one side of the beta source compartment), in order to obtain events with the longest trajectories. Other configurations can be adopted according to the measurement goal, e.g. 5-5 where the source

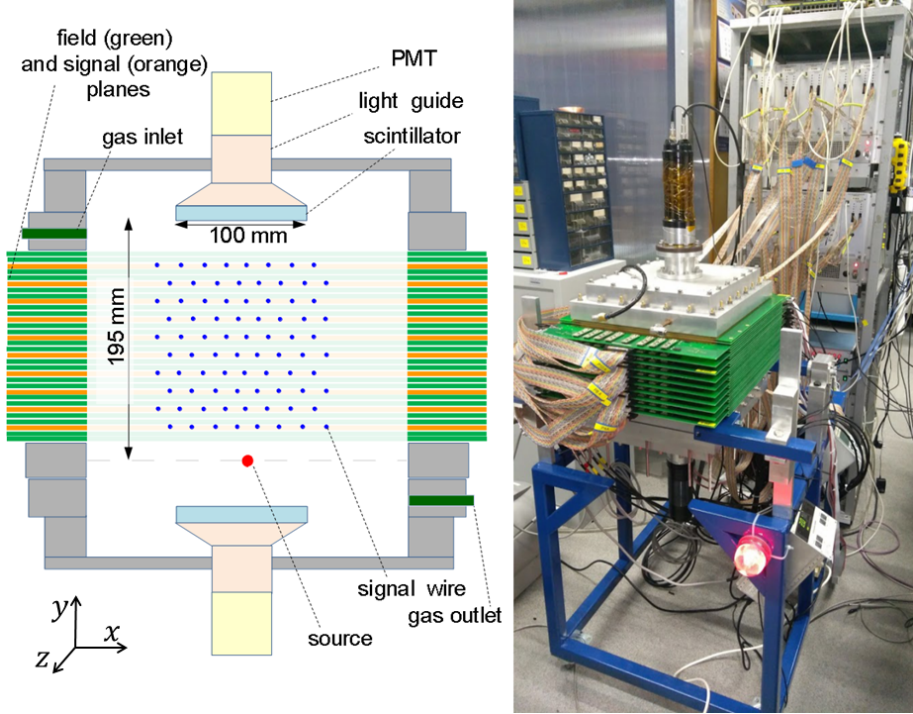


Figure 3.10: (Left) Schematic overview of the miniBETA spectrometer. (Right) Picture of the actual setup used during the commissioning phase.

is located between two sides, built from 5 layers of detection cells each, which increases the solid angle covered by the detector.

Field and signal planes are major constituents of the system. These are frames, made from multilayer printed circuit boards (PCB), with wires soldered to pads, stretching across the opening (3.11, left). Field wires are made out of copper-beryllium $\phi = 75 \mu\text{m}$. Signal wires are made out of chromium-nickel 8020 alloy $\phi = 25 \mu\text{m}$. This alloy provides relatively high resistivity ($R = 500 \Omega$ for $l = 24 \text{ cm}$), which is beneficial for the charge division technique (Sec 6.2). The distance between two wires on a plane is always 17.3 mm.

The system is simplified thanks to a single design for all signal planes and a single one for all field planes. The honeycomb cell structure is achieved by rotating subsequent planes by 180° , which introduces a half-cell translation of wires positions and a spare wire WS becomes W1 in the rotated configuration. This structure helps to resolve the left-right ambiguity during particle tracking.

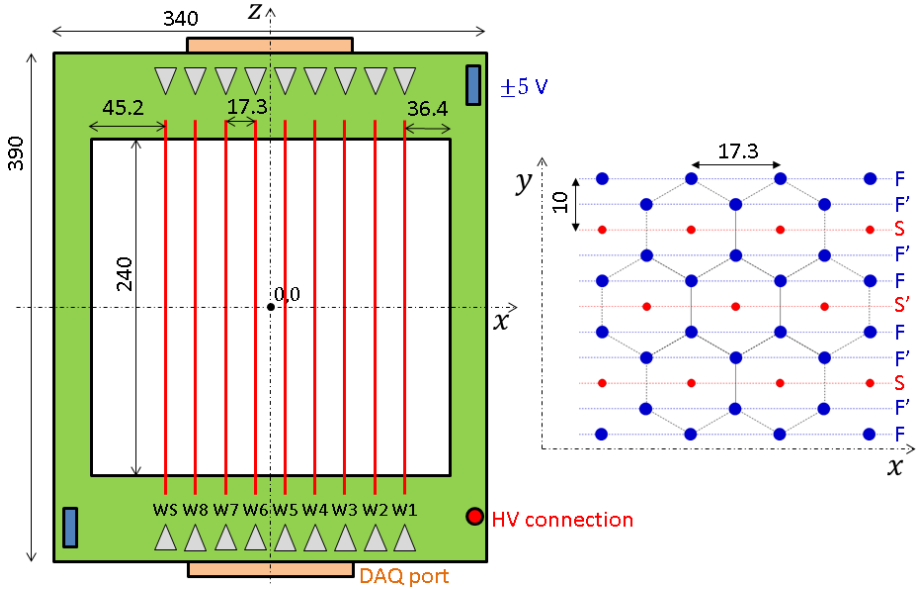


Figure 3.11: (Left) Scheme of the signal plane. Wires are marked in red and labeled W1...WS. Grey triangles visualize locations where the preamplifiers are mounted. (Right) Honeycomb structure formed by signal (S, red) and field (F, blue) wires. Letters with an apostrophe indicates planes turned by 180°. Dimensions are given in mm.

The hexagonal shape limits the number of wires required to form a cell, thus limits the probability of a particle scattering on a wire [34]. The plane design includes additional pads (not visible on the picture), which can form a planar (rectangular) cell configuration if one decides to use additional wires.

All the planes are connected to a common ground by a bridge formed when the planes are stacked together. The connection is made thanks to gold plated bands, that run on every plane, being connected by the aluminum spacers in between the planes. Field wires are connected to the ground. Each signal plane is connected to a single channel of a high voltage power supply (EBS8030), providing the same voltage on all wires of a given plane. The current on each HV channel is monitored by the custom made nanoamperometer connected to a PC by USB. Since the meter is floating on the high voltage, in order to prevent dangerous shortcuts, it is powered with batteries and the USB connection is decoupled by an optical link.

In addition, each signal plane is equipped with sockets for ± 5 V, which powers current preamplifiers and is generated by a custom made power supply. The preamplifiers are mounted directly on a signal plane in sockets at both sides of the signal wires in order to minimize the input noise and protect the signal from EM interferences. A 34-pin socket is located at each side of a signal plane and is used to read out signals from the preamplifiers. Flat ribbon cables are used to connect the signal planes with the DAQ.

Preamplifiers are easily replaceable, which benefits the system modularity. They work in current-mode with the input impedance below 5 ohms and the input stage bandwidth exceeding 300 MHz. The first stage of the preamplifier is a current-voltage converter with two fast bipolar transistors. The voltage pulse is fed to the high-pass filter which cuts off the DC bias and the slow varying components of the signal. The first filter is followed by a low-pass filter integrating the pulse with 100 ns time constant. The signal is then amplified and transmitted to the differential amplifier used to drive the transmission line. Differential signal transmission increases the external noise immunity when unshielded cables are used.

A simplified scheme of the DAQ architecture is presented in Fig. 3.12. A single DAQ module is responsible for data acquisition from a single plane. The module consists of two analog cards and one digital card, providing 16 ADC (analog-to-digital converter) and 8 TDC (time-to-digital converter) channels. The digital data is transmitted via a LAN port to the back-end computer where the process of receiving, sorting and formatting to a complete physical event is provided by the data logging software. The card configuration settings and control is done via a RS485 port. All modules are synchronized and share a common time-stamp, corresponding to the moment when the scintillator was hit by the ionizing particle.

The block diagram of the analog circuit is presented in Fig. 3.13. Differential signals from the preamplifiers are processed by the analog circuit. The signals from both wire ends are split into two branches. In the first branch signals from both ends are added and fed to the discriminator, which produces a TTL pulse for the TDC. If the sum of the analog signals is higher than the set value of the discriminator threshold, the stop signal for the TDC is generated. In the second branch both signals are transmitted to the fast peak-hold detectors, which are responsible for detection of the pulse amplitudes in a given gate time. Peak-hold detectors are used to stretch the pulse to the length acceptable for the ADC converters. The gate and hold signals are produced by a programmable timing circuit located on the analog board which uses the TDC start signal (external trigger) as a time reference. Analog boards hosting the analog signal processing circuits are equipped with built-in controllers for setting the thresholds of the

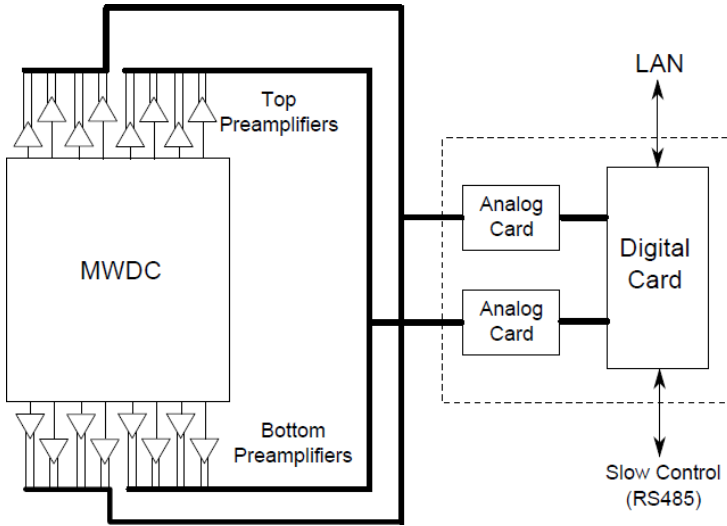


Figure 3.12: Schematic of the data acquisition architecture [34].

discriminators as well as the gate and the hold timing. The set values are fed to the controller over a slow-control bus (RS485).

The block diagram of the digital circuit is presented in Fig. 3.14. The digital board consists of 16 channels of 14-bit ADCs (using AD8099 chips made by Analog Devices) and a 8 channel TDC (using TDC-GPX chip made by Acam Messelectronic GmbH). The board measures the delay between the common start (trigger) pulse and the individual stop signals received from the discriminators, as well as the amplitudes of the pulses delivered by the peak-hold detectors. The stop signals are delayed by a 50 ns delay line in order to compensate for the delays introduced in the analog electronics. The ADCs sample the signals with 20 Msps sampling rate. The FPGA chip (Xilinx Spartan XC3S400) receives the data from the ADCs and the TDC, buffers them, provides zero-suppression and time-stamping, and formats the data frame. The data frame is transmitted to the integrated Ethernet/UDP stack (Wiznet W5100) which is responsible for communication with the backend PC hosting acquisition and control software. The digital board is also equipped with a built-in controller providing initialization and configuration of ADC, TDC and Ethernet chips. This controller is accessible via the slow-control bus.

A detailed description of the miniBETA DAQ is provided in [34]. Parts of this description were included in the above text, for the sake of the thesis completeness.

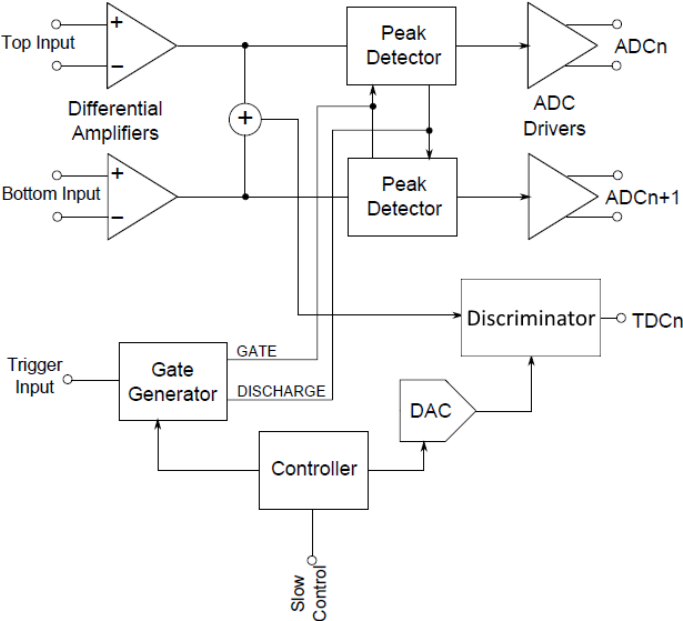


Figure 3.13: Block diagram of the analog board [34].

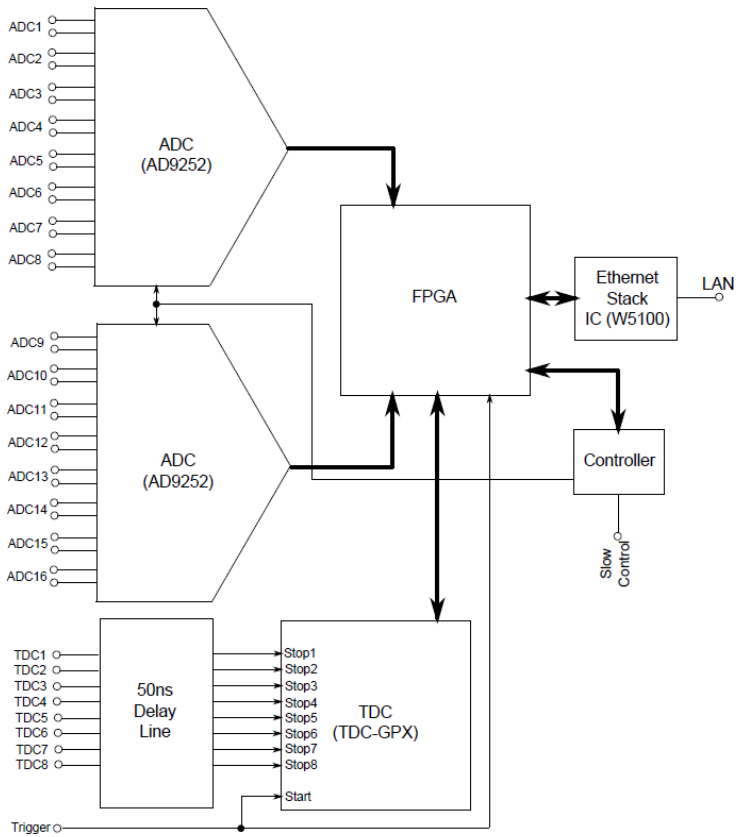


Figure 3.14: Block diagram of the digital board [34].

3.4.2 Gas system

Figure 3.15 presents a simplified scheme of the miniBETA gas system. The purity of helium and isobutane used in the measurements was 6.0 and 3.5, respectively. The gas mixture composition and its pressure are controlled with the PC. Two separate Bronkhorst Mass Flow Controllers F-201CV, based on individually calibrated thermal mass flow sensors, regulate the gas flow in each of the inlet lines. The composition is obtained by setting the flows according to the required ratio. The typically used flow value is ~ 0.05 l/min, which refills the chamber from 1 to 600 mbar within ~ 2 h. The chamber can be quickly vented through a manual valve, which is connected directly to the dry scroll vacuum pump, Agilent IDP15.

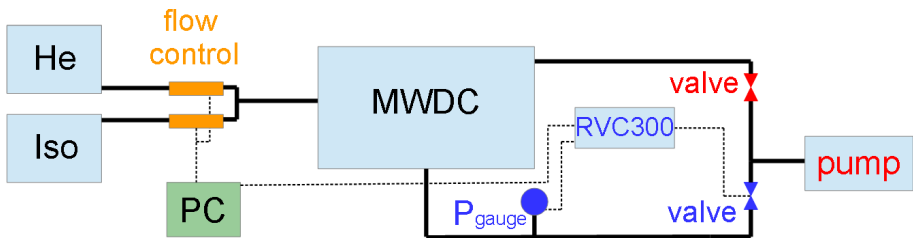


Figure 3.15: Schematic overview of the miniBETA gas system.

The pressure in the chamber is monitored and controlled by a set of devices produced by Pfeiffer Vacuum. A control module RVC 300 reads the pressure value from a gauge APR 250 and compares it with the one set by the PC. The module controls a motorized valve EVR 116, adjusting the opening to the vacuum pump, according to a PID loop control. The pressure stability is at the level of 1 mbar.

The mixture purity in the chamber is limited by the system tightness. A test was performed, during which the pressure was set to 300 mbar and valves were locked. Rise of the pressure was monitored over several hours. The calculated leakage rate was $r_L = 0.14$ mbar/h. With the filling rate $r_F = 344$ mbar/h the contamination level is $r_L/r_F = 0.0004$, so the mixture purity can be expressed as 3.5. The uncertainty of this result is a few orders of magnitude smaller than the value itself, hence it is not presented. The main cause of the leakage is the high number of rubber O-rings required in the setup, placed in between all the planes.

3.4.3 Control and analysis software

The experiment is operated with a dedicated software written in Python [60] (Fig. 3.16). Its graphical user interface (GUI) is based on the Qt libraries [61]. When a measurement is started the control software runs a receiver program, written in C++ [62], which listens to DAQ ports and aggregates the incoming data into events with the same time-stamp, saving them in a shared memory [34]. An object called `DataLogger` is created by the control software in parallel to the receiver. It is responsible for creating a HDF5 [63] file, where readouts of auxiliary sensors are saved along with the data from the DAQ in structures convenient for the analysis. Serial communication with sensors, mostly through USB and RS232 ports, is handled by the `pySerial` library [64].

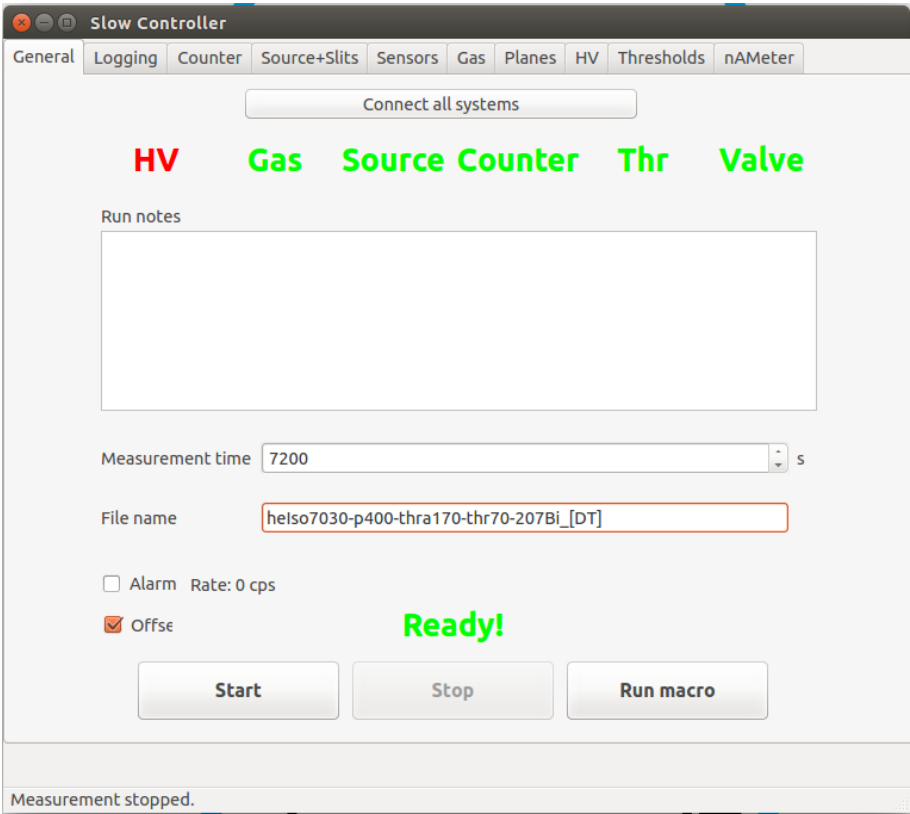


Figure 3.16: Screenshot of the program controlling the experiment.

Moreover, the control software is responsible for monitoring and operating multiple subsystems. It allows to:

- Change the source position if the motorized source positioning system is used.
- Set and read the flow, the ratio and the pressure of the gas mixture.
- Set and read the HV value on each signal plane and the current powering it.
- Set and read parameters of the DAQ, such as the ADC discrimination threshold.
- Monitor ambient temperature and pressure.

The control software is also able to stop the measurement and turn off the HV and the gas flow if hazardous conditions, like a sudden change in the gas flow or excessive current drain, are detected.

An additional software with a GUI was developed for the data analysis (Fig. 3.17). It is written in `Python` and uses the following libraries:

- `PyTables`: integrates the HDF5 format into the analysis, accelerating the process of managing very large amounts of data. One important feature of `PyTables` is that it optimizes memory and disk resources so that data takes less space [65];
- `SciPy`: an ecosystem providing the most essential tools for mathematics, science, and engineering [66] including: `NumPy` - the fundamental package for scientific computing with `Python`, introducing N-dimensional arrays [67] and `matplotlib` - a comprehensive 2D plotting library [68];
- `uncertainties`: a library introducing `ufloat` objects, which store variables values and associated uncertainties. Mathematical operations performed with such objects automatically calculate the uncertainty of the product, based on the linear error propagation theory with derivatives calculated through analytical formulas. [69].
- `lmfit` - a library providing a high-level interface to non-linear optimization and curve fitting problems for `Python` [70].

The analysis software allows for quick visualization of the recorded data. One can plot distributions of multiple variables, e.g. signal heights and drift times,

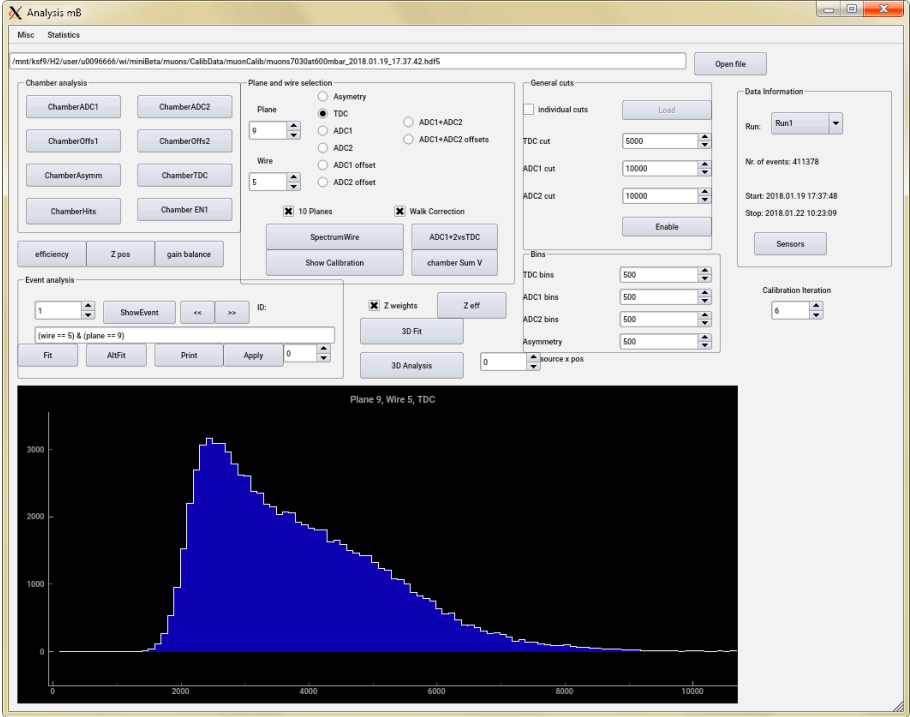


Figure 3.17: Screenshot of the analysis program.

as well as monitor sensors readout in time or visualize a trajectory of a particle with a certain id. The software also automatizes a couple of algorithms (e.g the drift time-to-radius relation autocalibration), described in the following sections, delivering the final results with one click in the GUI.

Python and its libraries are handled by the Anaconda distribution [71]. It provides simplified package management with version and dependency control, maintaining software integrity.

Chapter 4

Initial tests of the chamber performance under different gas and voltage conditions

4.1 Overview

The amount of electrons created in a gas detector (both through primary and secondary ionization) depends, among other factors, on the gas mixture and its pressure. Additional processes, involving meta-stable states (Penning effect) and optical resonances with a long lifetime, can influence the amount of the ionization when a mixture of gases is being used [48, 56, 59]. The complete process of the signal creation is still not fully understood and in order to obtain quantitative results for a given mixture in certain conditions, experimental measurements have to be performed.

One of the crucial parameters determining drift chamber operation is the voltage applied to the signal wires (Fig. 3.9). If it is too low, some of the electrons might “get lost” on their way and/or multiplication inside the avalanche will be too small to produce a signal sufficiently higher than the electronic noise. On the other hand, setting the voltage too high will bring the chamber to the Geiger-Müller mode, where the field is so high that it causes repetitive discharges inside the whole chamber or causes Malter breakdown [72], ejecting electrons from cathode wires or aluminum walls. Both of these effects make tracking of the ionizing particles no longer possible. Too high voltage can also

cause bigger sparks or even arcs in the system, which can burn the wires and some parts of the electronics. The optimal voltage depends on the gas mixture and its pressure.

During the initial tests, mixtures of helium isobutane at percentage ratios: 0/100, 50/50, 70/30, 90/10 both at 300 and 600 mbars were tested. An alternative DAQ system: FASTER module from LPC Caen [73], was used in addition to the custom miniBETA DAQ in order to better understand the chamber performance and to cross-validate the results. The measurements were performed with the setup consisting of only one detection layer (1 signal plane stacked between 4 field planes) in order to minimize the potential damage that can be caused if a spark or an arc appeared in the chamber. A ^{45}Ca source, decay of which is vastly dominated by a β^- transition [74], was mounted in front of the wire no 5.

The single cell counting efficiency η_0 , i.e. the probability that the single cell will produce a measurable signal if the scintillator was reporting a hit, was measured to establish how the detector performance is affected by changing gas mixture and voltage on signal wires. In this picture, a geometrical correction, being a ratio of the cell and the scintillator acceptance solid angles, is not included. It was found, that due to the scintillator efficiency inhomogeneity (Sec. 7.3) and influence of the in-gas scattering, this correction would not bring any added value at this stage of the project. The efficiencies obtained in such a way were compared, and regions where they reach plateaus, were looked for. A better estimate of the cell detection efficiency, which involves tracking of the particles, is described in Sec. 5.4.2.

After filling the chamber with a given gas mixture and waiting for the pressure to settle down, automated high voltage (HV) scans were performed, conducted by the control software. For each voltage step, a one hour long measurement was performed.

A custom made nanoamperometer was used to measure the current in the HV line powering the plane. During normal operation a plane drains tens of nA. The nanoamperometer was communicating with the PC through a USB port and whenever the current drain exceeded $1\text{ }\mu\text{A}$ the HV was automatically turned off by the control software. Such an increase in the current is undesirable and indicates that the conditions inside the chamber changed (e.g. due to the Malter effect or chamber entering the Geiger-Müller mode) which is potentially harmful to the experiment.

4.2 MiniBETA configuration

A simplified scheme of the electronic setup with the miniBETA custom DAQ is presented in Fig. 4.1. The output of the signal plane (after the preamplifier mounted on the plane) was directly connected to one of the miniBETA DAQ modules by a flat ribbon cable. The signal from the PMT was passing through an amplification module, with the gain $\times 10$, and then entered a constant fraction discriminator (CFD), which provided a logic signal (TTL) for the miniBETA Triggering Unit, responsible for triggering the readout of the DAQ module. The optimal threshold for the CFD was found to be ~ 15 mV. The total time delay for the trigger line (measured on the oscilloscope as the time difference between signals from the PMT output and the Triggering Unit input) was 60 ns. Signals from the plane are delayed by a line built into the DAQ to compensate for the delays introduced in the analog electronics.

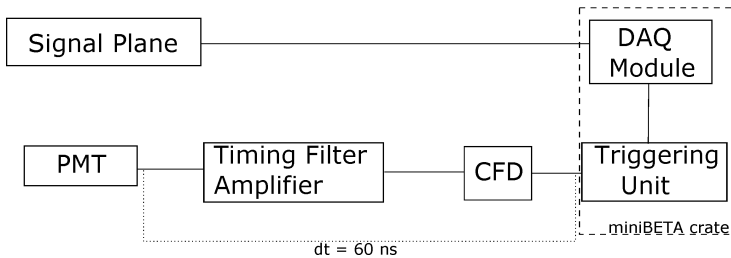


Figure 4.1: Scheme of the electronic setup used for the single plane measurements, when the data was collected by the miniBETA DAQ. The signal from the chamber, after passing the preamplifiers mounted on the plane, went directly to the DAQ. The PMT signal was additionally amplified and converted into a logic signal by external modules before reaching the triggering unit.

In the configuration involving the miniBETA DAQ, the direct number of PMT triggers is not available, since only the number of coincidence events between the chamber and the trigger $N_{c,m\beta}$ is being recorded. An external scaler module was used in order to count the number of triggers coming from the PMT. This number was estimated based on a short measurement for each gas mixture. The counting rate ρ_{PMT} was varying from 77(2) counts per second (cps) for the 50-50 mixture at 600 mbar to 120(3) cps for 70-30 at 300 mbar. The counting rate was correlated with the mixture density and isobutane percentage, which indicates that the stopping power of the gas has a significant effect on measurements with the ^{45}Ca source, due to its low endpoint energy ($E_0 = 255.8$ keV). The counting rate of the PMT without the source inside (a background level) was measured to be $\rho_b = 10(1)$ cps.

The single cell counting efficiency $\eta_{0,m\beta}$ for this setup was calculated as:

$$\eta_{0,m\beta} = \frac{N_{c,m\beta}}{(\rho_{PMT,m\beta} - \rho_b) \cdot t}. \quad (4.1)$$

Determined efficiencies are presented in Fig. 4.3. They will be discussed in more detail and compared with the efficiencies obtained with the FASTER system in Sec. 4.4

4.3 FASTER configuration

FASTER is a DAQ module produced by LPC Caen [73]. The module that was used has 4 channels and was designed for spectroscopy usage. For each detected event FASTER measures, digitizes and sends to the PC the following quantities:

- t : a timestamp of the trigger (in ns) - the moment when the signal passed the given threshold,
- Δt : a time interval (in ns) between the trigger and the moment when the signal reached its maximum height,
- V : height of the signal (in mV),
- Pileup: a flag saying if during a given time window a pile-up occurred,
- Saturation: a flag saying if the signal height was higher than the V range.

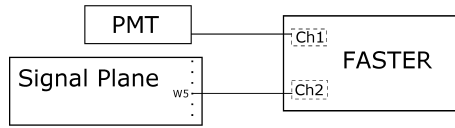


Figure 4.2: Scheme of the electronic setup using the FASTER DAQ. The PMT and the pin corresponding to the preamplified signal from the single end of the wire were both directly connected to individual FASTER channels.

In the tested setup, 2 FASTER channels were used and a scheme of the setup is presented in Fig. 4.2. The signal from the PMT was plugged directly to the first input. After shifting the channel baseline to 0 mV the PMT trigger threshold was set to 1.8 mV. The t value of this channel was used to provide timestamps for the PMT signals.

The second channel was dedicated to the preamplified signal from the signal wire in the chamber. To acquire the signal from the signal plane a passive probe was used. The signal was received from an output pin of the plane, corresponding to the single end of the wire number 5, with the ground of the probe being connected to a grounded pin. The baseline of the signal was shifted to 0 mV, and the trigger level for this channel was set to 15 mV. It was observed that the signal from the signal plane reveals more noise than the one from the PMT, hence the higher threshold. Using FASTER allowed to analyze additional data, not available in the miniBETA setup, i.e. the individual number of counts for each channel, the height of the signals in mV and their rise times. The background of the PMT ρ_b was found to be at the same level as when measured with the scaler in the miniBETA configuration.

The source was positioned in front of the mid-point of the wire. This configuration provides the signal only from one end of the wire. However, it was considered to be sufficient for the test measurements, since distributions of signal characteristics (i.e. heights and rise times) from the other side of the wire were very similar.

Since signals from both channels were recorded individually, a coincidence analysis was performed off-line. The pairs of recorded signals with timestamps in the range (-1000, +20000 ns) were flagged and the differences between timestamps were saved as values of the drift time t_d . The flagged hits could then be compared with the hits recorded by the miniBETA module, where only coincidences are recorded, by default.

The single cell counting efficiency $\eta_{0,F}$ for this setup was calculated as:

$$\eta_{0,F} = \frac{N_{c,F}}{N_{PMT,F} - \rho_b \cdot t}, \quad (4.2)$$

where $N_{c,F}$ is the number of hits with the coincidence flag, $N_{PMT,F}$ is the total number of hits recorded by the PMT channel, ρ_b is the counting rate of the background, and t is the length of the measurement. Determined efficiencies are presented in Fig. 4.3. They will be discussed in more detail and compare with the efficiencies obtained with miniBETA in the next paragraph.

4.4 Results of the HV scans with the single detection plane

The value of η_0 was calculated for each measured voltage step and each gas mixture, both for miniBETA and FASTER configuration (Fig. 4.3). The

mixture 0/100 (pure isobutane) at 600 mbar was excluded since it was observed that it would require a voltage higher than the system could handle. Mixtures of 90/10, both at 300 and 600 mbar, were quickly becoming unstable (causing a breakdown - a high current drain by the plane), thus no complete scan was available for this ratio. After the breakdown, a reduction in the ratio of coincidences was observed. One had to reduce the HV below 1000 V and then ramp up again in order to resume the standard behavior of the chamber. It was also observed that the voltage around which the chamber becomes unstable was decreasing each time a breakdown occurred and some time had to pass if one wanted to bring the stability limits back to higher levels.

These observations led to a conclusion that breakdowns were caused by the Malter effect rather than Geiger-Müller [72,75,76]. In the Malter theory, positive ions are accumulating on the insulating layer covering the cathode wires (from polymerized isobutane residua - aging effect) or the aluminum walls (due to their oxidation) and can build-up a charge high enough to rip off electrons from cathodes/walls, through the insulator. This charge builds up in time. Significant reduction of the anode voltage is required to cut off the resulting current and passing of some time might be required to fully discharge the surfaces. Additionally, the Malter effect is light sensitive, which can explain why mixtures with high helium ratio were more prone to the breakdown. Using alcohol or water additives was found to eliminate the breakdown problems in the BaBar drift chamber [75], which also operated with a helium-isobutane mixture and can be considered for miniBETA if less stable mixtures are used.

A desirable behavior of the chamber would show a plateau above a certain level of HV, where η_0 reaches its maximum value. However, no saturation of the efficiency was observed at all. Moreover, instead of this, some mixtures (e.g. 70-30 at 300 mbar) showed even an exponential increase in the counting rate. It was realized that additional criteria are needed to filter out some systematic effects, which led to this excess. The relation between the η_0 and HV measured with the 70-30 at 300 mbar mixture and the influence of the applied cuts is presented in Fig. 4.4. The cuts and the reasoning behind them are explained in the following text.

It was found that secondary hits (after-pulses) have a significant influence on the total number of recorded coincidences N_c . These are hits which have been detected within the same PMT trigger time gate after another hit. The data was reanalyzed and an additional variable indexing the hits was added according to the order of the arrival times of hits within the same time gate. The number of primary hits was called N_{prim} .

It was observed that the ratio of secondary hits increased significantly with a rise of the applied voltage and their drift time spectrum was significantly

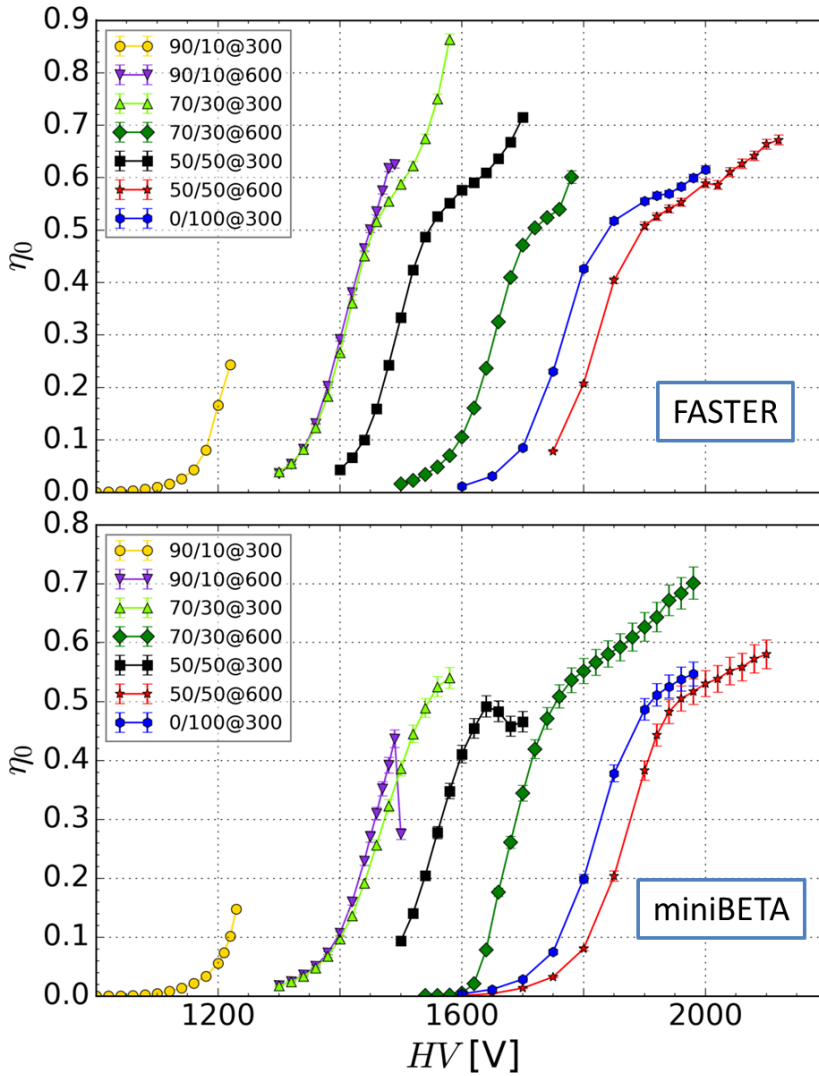


Figure 4.3: Plots of the counting efficiency η_0 for all hits from wire 5, measured with (top) FASTER and (bottom) miniBETA, for gas mixtures listed in legends.

shifted from the primary one (Fig. 4.5). Moreover, their amount was correlated with the gas ratio of the mixture filling the drift chamber. They were the most present in the 70-30 mixture at 300 mbar, where the amount of isobutane is

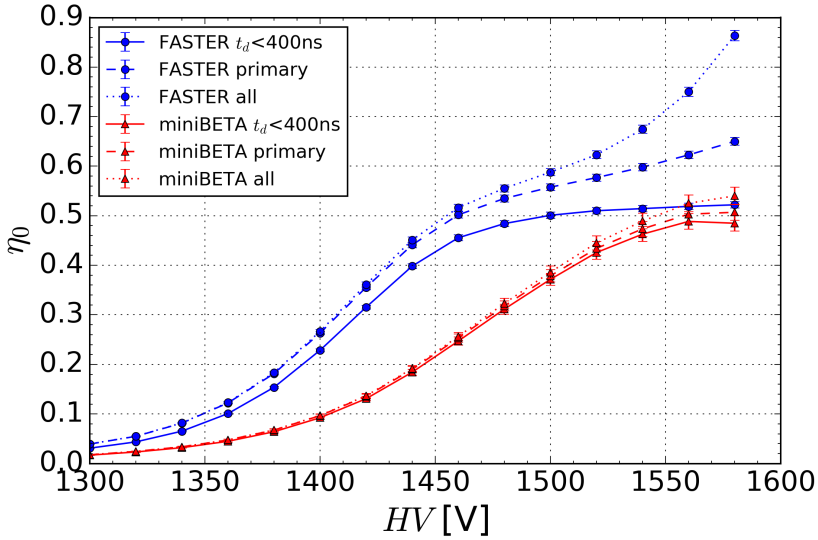


Figure 4.4: Relation between the calculated single cell efficiency η_0 (blue circles for FASTER and red triangles for miniBETA) and the voltage HV applied to the signal plane. The chamber was field with the 70/30 helium-isobutane mixture at 300 mbar. Dotted lines correspond to the data with no cuts, dashed - only primary hits and solid for the hits with the additional cut filtering out hits with $t_d > 400$ ns.

the lowest (90-10 mixtures became unstable before this effect could have been observed).

It is possible that this effect is caused by an influence of the UV light, created during avalanches, where the collected charge is multiplied in the vicinity of the signal wire when gas particles are heavily bombarded by accelerated electrons [77]. The isobutane in the mixture, having an ability to absorb the energy in a wide wavelength range due to numerous vibrational and rotational excited states, acts as a quencher and absorbs photons before they cause an additional ionization or knock electrons out of the chamber walls. Its presence in the mixture limits the amount of undesirable ionization, which obscures the ionization used for particle tracking.

Filtering out secondary hits still left the excess of counts, which seemed to be noise-related. It was observed that the distribution of the time difference t_d between the trigger signal and the charge collection has a very long tail towards the higher drift times (Fig. 4.5). The relation $r(t)$ between the drift distance and the drift time is questionable for such hits since their origin is dubious.

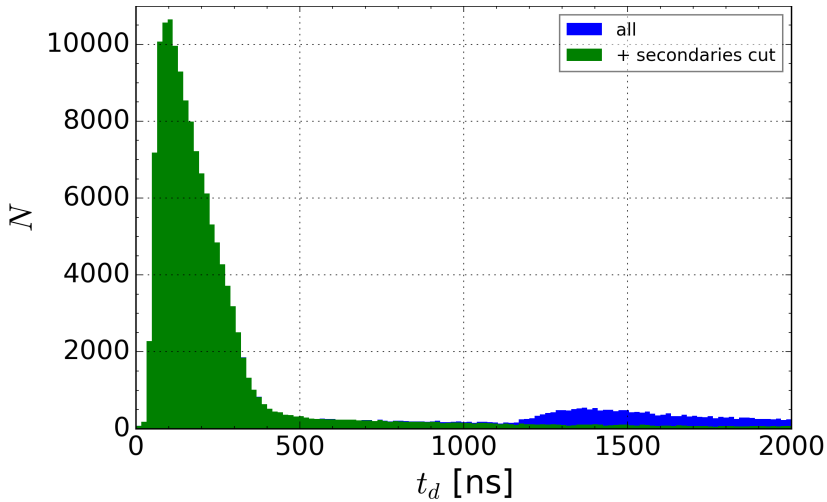


Figure 4.5: Distributions of the time t_d between the signals from both FASTER channels fulfilling the coincidence criteria. Blue represents all of the hits and green relates to the hits after the secondary ones (i.e. additional coincidences within the same time gate) were filtered out.

They might come from electrons created close to the borders of the cell, where the electric field is the weakest and ionized particles had to wander for some time before being attracted by the wire. Additionally, free electrons created outside of the detection plane borders can be attracted by it, since there are no physical boundaries in between.

Based on the above considerations, an additional cut was applied to the data. All the hits with $t_d > 400$ ns were removed from the analysis. The number of hits that was left after the above cuts was called N_{td} . After the final cut, it was observed that the single cell efficiency started to saturate above a certain voltage for a given gas mixture (Fig. 4.6). Additionally, this cut cleared the spectra of V and Δt recorded by FASTER from distinctive hits with a short rise time and a low height, probably originating from the noise (Fig. 4.7).

A common feature was observed for all the mixtures when FASTER and miniBETA DAQs were compared: until a certain voltage there were always fewer coincidences in the miniBETA data for a given voltage step (see Fig. 4.6). After analyzing the data it was found that this behavior is probably caused by a setting of a trigger threshold in the analog part of the miniBETA DAQ, the level of which was found to be higher than the FASTER one. This means that a higher signal was required to count as a hit for miniBETA.

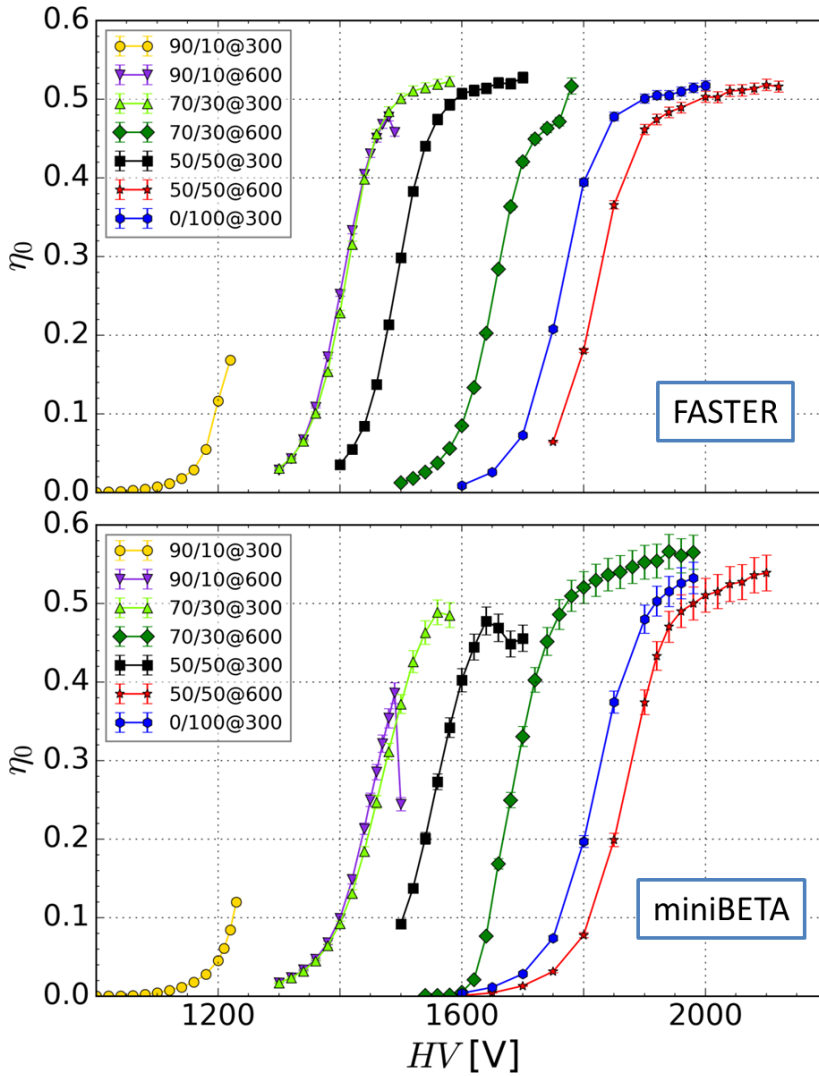


Figure 4.6: Efficiency η_0 for the hits remaining after both of the cuts were applied, measured with (top) FASTER and (bottom) miniBETA for gas mixtures listed in legends.

The range of the ADC was found to be too small in the miniBETA DAQ, as even before η_0 reached the plateau, distributions of V were showing mostly overshoots. This is an unwanted feature because the information about the signal height is

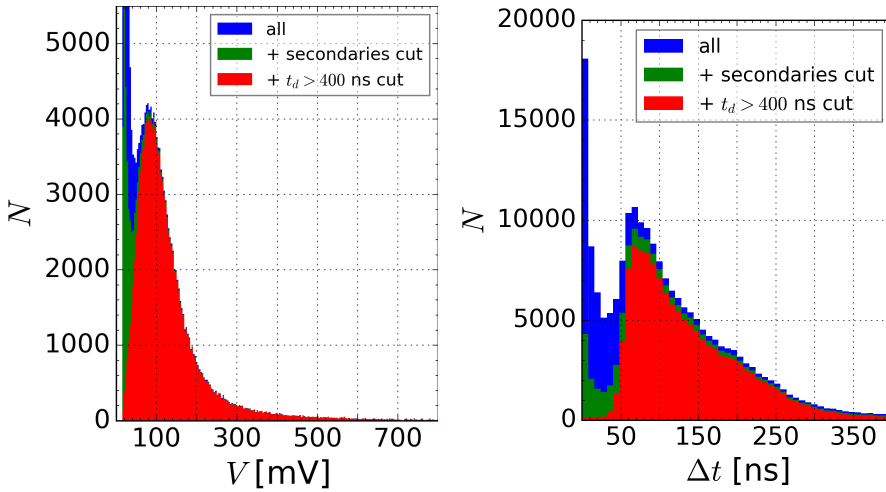


Figure 4.7: (Left) Distribution of recorded signal heights V . (Right) Distribution of recorded signal rise times Δt . Both distributions were recorded with FASTER. Colors on both spectra correspond to: (blue) the initial data; (green) the data with secondaries hits being filtered out; (red) after the additional cut, filtering out hits with a drift time $t_d > 400$ ns.

crucial for the charge division technique used to obtain a coordinate along the signal wire (Sec. 6.2). The left panel of Fig. 4.8 shows the relation between the mean value of the distribution of V measured with FASTER and the applied voltage HV . These values were then paired with the corresponding miniBETA η_0 in order to find a correlation between the signal height and the single cell efficiency (right panel of Fig. 4.8). The HV scans showed a common feature for all the mixtures: the height V of the recorded signal is the crucial parameter for the miniBETA DAQ to operate properly. The mode of its distribution has to be higher than 80 mV, in order for the full spectrum to pass the trigger.

4.5 Summary and conclusions

The HV scans performed with the single detection plane and both miniBETA and FASTER DAQs allowed for a better understanding of the detector performance and led to several improvements of the system. It was found that the single cell counting efficiency is the highest when the chamber operates in the region where the charge produced in the avalanche multiplication is high enough to produce a signal that after the charge-to-voltage preamplification can pass the

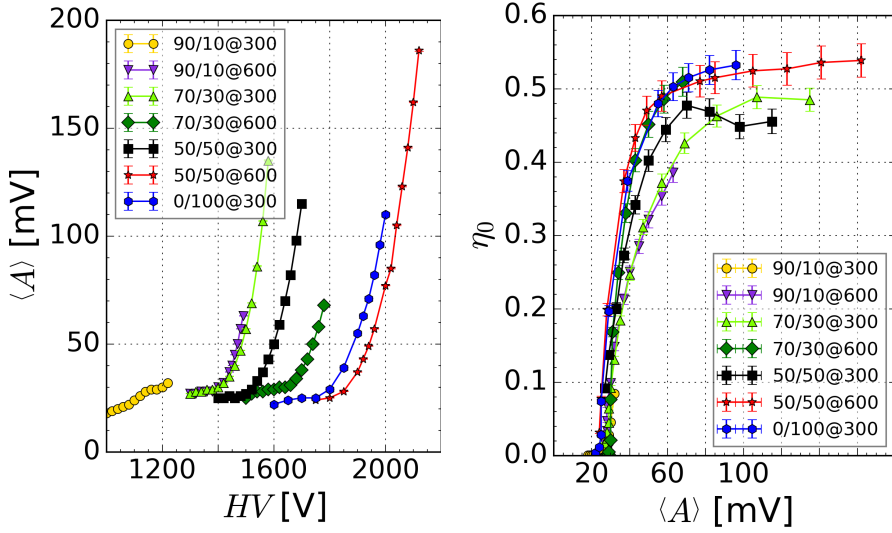


Figure 4.8: (Left) Relation between the calculated mean value of the FASTER signal height distributions $\langle A \rangle$ and the voltage HV applied on the signal plane. (Right) Relation between the calculated single cell efficiency $\eta_{0,mB}$ and $\langle A \rangle$.

effective threshold. This can be figured out by looking at the total signal height spectrum $Q = V_1 + V_2$. The position of its maximum has to be clearly distant from the histogram origin, so that the spectrum slope is not distorted by the threshold (Fig. 4.9).

Mixtures of 90/10 helium-isobutane ratio, both at 300 and 600 mbar, were not able to reach the satisfying detection efficiency since they were quickly becoming unstable entering the high current drain mode. This is caused due to the high ionization potential of helium, hence a low amount of primary ionization generated in it (Tab. 3.2). A higher percentage of the isobutane is required, which significantly enhances the total ionization. Other mixtures at 300 mbar (besides the very stable pure isobutane) demanded greater caution while measuring. Some voltage steps had to be remeasured because gas breakdown occurred even after running stable for some time already. Lack of room temperature control could have been responsible for this behavior. The whole detector was therefore moved to a room with an air conditioning and an integrated temperature stabilization.

Based on measured distributions of signal heights V (Fig. 4.7 left) a wider range for the ADC was established. The upper limit was set to ~ 400 mV. Although the distributions have long tails towards higher signals, exceeding the

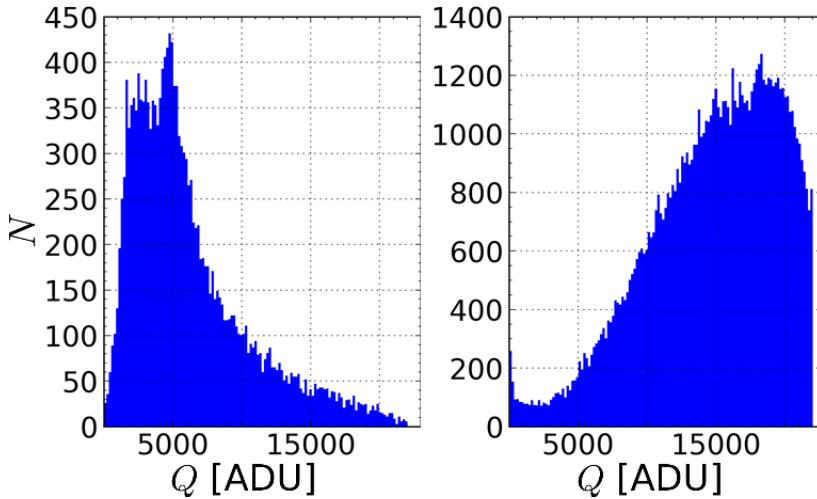


Figure 4.9: Distributions of the total signal height Q for the 70/30 helium-isobutane mixture at 300 mbar for the signal plane at (left) 1380 V, where the gain was too low and (right) 1580 V, where the gain was high enough (however the ADC range was insufficient).

limit of the ADC, the chosen range provides the optimal resolution [78]. The ability to measure the highest signals properly was compromised in order to keep the expected value of the signal height distribution close to the middle of the ADC's range.

The rise time Δt of signals delivered by FASTER revealed a broad range (Fig. 4.7 right), which is not tolerated by the Constant Fraction Discriminator (CFD) used in the miniBETA DAQ analog boards. All discriminators were therefore exchanged to Leading Edge ones, simply triggering when the signal passes the given threshold. The influence of the walk effect introduced by new discriminators is analyzed in Sec. 5.3.1.

It was observed that the secondary pulses, especially for mixtures with lower isobutane ratio at higher voltages, can disturb the efficiency estimations. However, simply removing all counts other than the primary ones, solves the problem.

In addition, filtering out all hits with $t_d > 400$ ns cleared the data from the counts of a dubious origin. Later on, when the chamber was modified to use more planes, it was observed that this effect is mostly present in the external cells. Hence the conclusion that these counts are caused by the electrons drifting

to the cell from further parts of the chamber, outside of the area of the cells. Because the inner cells are shielded by the external ones, this effect vanishes.

During the Townsend avalanche, a high number of photons is created in addition to electrons. The quencher absorbs these photons, limiting their range in the detector. If the amount of isobutane is not high enough (or the gas gain is too high), photons from the avalanche can reach the chamber walls, causing the photoelectric effect. Photoelectrons drift to the nearest cell, where they create secondary pulses with lower than typical heights (single photoelectron vs ionization cluster of multiple electrons). This mechanism explains the observed relation between the isobutane amount, the gas gain and the number of secondary counts as well as their delayed drift time distribution (Fig. 4.5).

The ^{45}Ca source was found inappropriate for the chamber commissioning phase due to the greater systematic effects related to its low E_0 . In the later measurements it was replaced by a ^{207}Bi source, emitting conversion electrons with energy groups around 500 and 1000 keV [74]. Having a discrete spectrum is also beneficial for the spectrometer calibration.

4.6 HV settings for 10 planes configuration

The following parts of the thesis describe measurements performed with the chamber consisting of 10 consecutive rows of cells (Fig. 3.10). The HV needed for this configuration is significantly higher than the one for the same mixture but with only one signal plane. This effect is understandable since the presence of charge on other planes influences the field in the considered cell. In this section, the procedure used to find the chamber working point is described, i.e. the HV setting giving the desirable efficiency.

The influence of the HV setting on two observables has been monitored: (i) on spectra of the signal height and (ii) on the relative plane multiplicity (Fig. 4.10). ^{207}Bi was used as the radiation source. The voltage was evenly increased on each plane until spectra on the outer planes (1 and 10) were no longer distorted by the detection threshold. The even voltage on all planes resulted in a lower signal gain for the inner planes (2-9). The relative plane multiplicity, calculated as the number of hits N_i on a plane i divided by the number of hits N_{10} on plane 10, confirmed that the efficiency was lower inside the chamber when the voltage was equal on all planes.

In order to compensate for this effect, the voltage was increased on the inner planes individually until all of the spectra were shifted such that they were no longer affected by the threshold and similar multiplicities were achieved for all

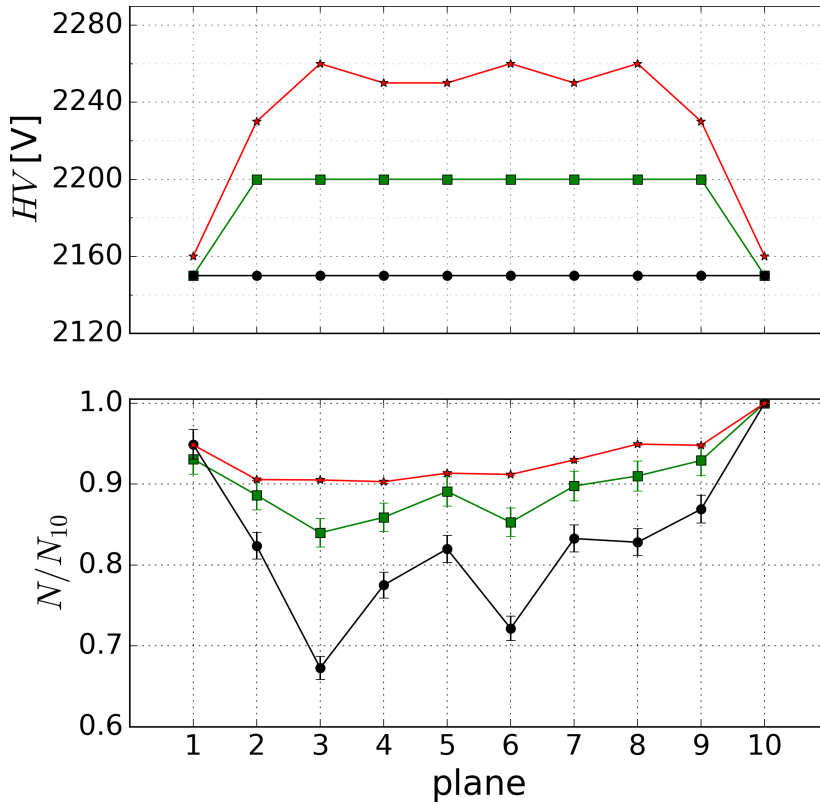


Figure 4.10: (Top) HV settings per plane. (Bottom) The relative plane multiplicity N_i/N_{10} , where N_i is the number of hits detected by the plane i , when the ^{207}Bi source was used and the chamber was filled with 50/50 at 600 mbar mixture. Colors and symbols correspond to 3 different measurements and are consistent in between the panels: (i) black - the initial; (ii) green - the intermediate; (iii) red - the final voltage setting. Connecting lines are added only to guide the eye.

the planes. It was observed that some planes required a slightly higher voltage than their neighbors, which can be a result of the varying performance of the electronic components used in their circuits.

The plane multiplicity can be treated as a simple tool for monitoring the plane performance while tuning the HV, although it does not take into account systematic effects such as the increased amount of noise at the outer planes or the system geometry. A more sophisticated method of calculating the detection

Table 4.1: Table of voltages set per given plane (#p) for a given mixture (mix 0/100@300 means 0/100 helium-isobutane mixture at 300 mbar), determined from the analysis of signal-height spectra and relative plane multiplicities.

#p↓ mix→	voltage [V]			
	50/50@600	0/100@300	70/30@600	50/50@300
1	2160	2100	1950	1750
2	2230	2170	2010	1820
3	2260	2180	2050	1850
4	2250	2180	2040	1850
5	2260	2190	2050	1850
6	2250	2190	2040	1850
7	2250	2180	2040	1850
8	2260	2180	2040	1850
9	2230	2170	2010	1820
10	2160	2100	1950	1770

efficiency, based on cosmic muons trajectories tracking, is presented later in the thesis (Sec. 5.4.2)

Table 4.1 presents values of HV per plane that were selected based on the above procedure for tested mixtures and that were since then used during the chamber commissioning. The mixture of 50/50 helium-isobutane ratio at 300 mbar was the last that has been tested in the described prototype, and this after a long period of extensive usage. The voltage stability was poor during that time and discharges, potentially further damaging the system, were occurring without a clear reason. It is believed that the electronic circuits on the PCB boards used as the signal planes were damaged because the safety current monitor was disconnecting the HV even for the mixtures that had already been tested previously and at levels where the chamber used to work without any problems, even before the defined working points were reached. Due to these issues, the HV for the 50/50 at 300 mbar mixture was limited to the level where the chamber was working relatively stable, but the desired signal height and the relative multiplicity was not reached. This issue is being fixed during the ongoing upgrade of the system.

In the following chapters, the 50/50 at 600 mbar mixture is used as the model one. Unless specifically mentioned, the analysis results, plots and tables relate to the chamber filled with this mixture. A comparison between the mixtures is presented at the end of the chapters. Similarly, the cell defined by wire 5 at plane 9 is used to present the standard behavior and the phrase “for the exemplary cell” refers to this cell.

Chapter 5

Reconstruction of particle trajectory in the xy -projection

5.1 Overview

When a charged particle is traversing a gaseous medium it ionizes atoms and gas molecules along its trajectory. Since particles measured in the miniBETA chamber move with relativistic velocities, one can assume that the ionization takes place instantaneously along the whole trajectory and that the particle hits the scintillator at the same moment. Subsequently, created electrons move slowly (as compared to the ionizing particle) towards centers of drift chamber cells, where the electric potential is the highest. Positive ions are attracted towards field wires which are grounded.

An instance of ionization in a cell, resulting in a single readout from the corresponding signal wire, is called a hit. An event is a collection of hits linked together by the same scintillator signal.

The drift time t of a hit is defined as the time which has passed between the detection of the ionizing particle by the scintillator and the detection of the hit in the signal wire.

The electron drift distance r is calculated according to a drift time-to-radius relation ($r - t$ relation, $r(t)$) and it approximates the distance of the closest approach of an ionizing particle trajectory to a cell center. Time offsets generated by delays in the electronics are neglected in this picture, but they are included in the analysis (Sec. 5.3.3).

Trajectories generated by cosmic muons were used to establish the $r - t$ relation for each individual cell in the chamber by an iterative autocalibration procedure. Major systematic effects, e.g. “time walk”, were identified and corrections were applied. The tracking resolution and efficiency in the drift plane were evaluated for a few gas mixtures.

Finding parameters of a trajectory allows to reduce the ambiguity of the hit location from the circle with radius r to the single point in the xy -coordinate system. The y -coordinates of the hits obtained this way are then used in the following analysis of the trajectory in the yz -projection.

5.2 Determination of the drift time-to-radius relation

Electron drift in a given gas mixture under certain electric field conditions is a complicated process with parameters which have to be experimentally determined. Simulations can provide qualitative guidance results [79] but in order to obtain quantitative results, one has to verify this relation experimentally. The following section describes algorithms determining ionizing particle trajectories in the miniBETA drift chamber and explains how the $r - t$ relation was obtained from measurements of cosmic muon trajectories traversing the tracking detector.

5.2.1 Principles of the trajectory fitting in the drift plane

Finding a trajectory of an ionizing particle traversing the chamber is performed in two steps. First, a prefit is done. A straight line passing the closest to the centers of cells participating in the event is found using the least-squares fitting. Parameters of this line are then used as an initial parametrization for the main fit. This step is crucial for the robustness of the main fit performance since without it the main fit tends to end in local minima. Hits from cells crossed by the prefit line are flagged and only these are included in the main fit. The prefit also helps to cut off outliers (random noise) from the main fit.

In the second step, for each cell i marked in the prefit, the drift distance r_i is calculated according to the cell’s individual $r_i(t)$ calibration for the recorded drift time t in that cell. Assuming cylindrical-like symmetry for the electric field inside a cell one obtains circles originating in the selected cells centers with radii $r_i(t)$ indicating equidistant positions where detected primary ionization

clusters could have been created. The main fit finds a trajectory:

$$x + Ay + C = 0, \quad (5.1)$$

which is the closest to these circles, using the least squares technique. The fit finds parameters A and C which minimize a sum of squared residuals $\sum_i \Delta_i^2 = \min$ defined as:

$$\Delta_i = d_i - r_i, \quad (5.2)$$

where d_i is the distance between the cell center $(x_{i,0}, y_{i,0})$ and the fitted line:

$$d_i = \frac{|Ay_{i,0} + x_{i,0} + C|}{\sqrt{A^2 + 1}}. \quad (5.3)$$

In other words, $\Delta_i = 0$ means that the fitted line is tangent to the circle with the radius r_i and the center at $(x_{i,0}, y_{i,0})$. Figure 5.1 shows an example of a fitted muon trajectory.

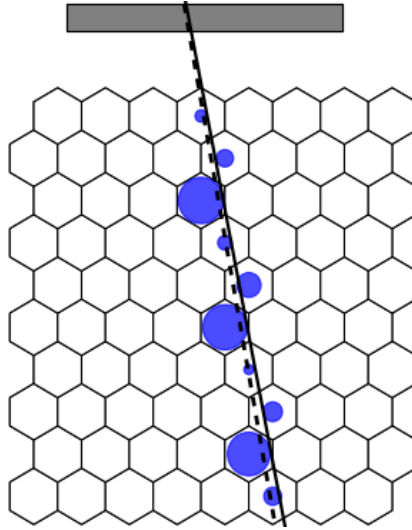


Figure 5.1: Reconstructed muon trajectory. The rectangle at the top of the picture represents the triggering scintillator. The circles originate in the centers of the cells which contributed to the event and their radii were calculated according to the individual $r(t)$ functions. The dashed line represents the prefit and the solid line represents the main fit.

5.2.2 Determination of x - and y -coordinates of the detected ionization position

In principle one does not possess information about hit x - and y -coordinates directly from the chamber readouts, only a circle of equidistant points defined by the measured drift time. Coordinates x and y of hits in an event can be calculated once the parameters of the straight line L passing closest to the circles are found (Sec. 5.2.1).

Equation (5.1) can be rewritten as:

$$L : x = ay + b. \quad (5.4)$$

A line $L_{i\perp}$ perpendicular to L , passing through a point $(x_{i,0}, y_{i,0})$ in the i -th cell center is given by:

$$L_{i\perp} : x = -\frac{1}{a}y + \frac{y_{i,0}}{a} + x_{i,0}. \quad (5.5)$$

The coordinates of the crossing point $P_{i,L} = (x_{i,L}, y_{i,L})$ are described by:

$$\begin{aligned} x_{i,L} &= \frac{a^2 x_{i,0} + ay_{i,0} - a^2 b}{a^2 + 1} + b, \\ y_{i,L} &= \frac{ax_{i,0} + y_{i,0} - ab}{a^2 + 1}. \end{aligned} \quad (5.6)$$

The point found in this way represents this part of primary ionization which was produced the closest to the cell center and is considered as the closest-approach point on the trajectory (due to the statistical character of primary ionization, these points do not have to align). Uncertainties of its coordinates are calculated according to the standard method of propagation of uncertainty, based on the parameters' a and b covariance matrix from the trajectory fit. The coordinate y_L will be used in the next chapter for finding the particle's trajectory in the yz -projection (Sec. 6.3)).

In order to complement the information about the fit an extra set of variables was introduced: r_s and d_s . They are defined as:

$$\begin{aligned} d_{i,s} &= \text{sgn}(x_{i,L} - x_{i,0}) \cdot |d|, \\ r_{i,s} &= \text{sgn}(x_{i,L} - x_{i,0}) \cdot |r|, \end{aligned} \quad (5.7)$$

where sgn is the sign function. They allow to look for systematic differences in the fitting between hits located to the left and to the right of the cell center, which are not visible in the default set because of its radial symmetry.

The partial residuals Δ_x and Δ_y are further useful variables, used in the following sections:

$$\begin{aligned}\Delta_x &= x_{i,L} - x_{i,0}, \\ \Delta_y &= y_{i,L} - y_{i,0}.\end{aligned}\tag{5.8}$$

5.2.3 Cosmic muons as the calibration source

Cosmic radiation hitting upper parts of the atmosphere produces pions, which quickly (within several meters) decay into muons and muon neutrinos (Fig. 5.2). Muon momenta p at the sea level range from $\sim 1\text{GeV}/c$ up to more than tens of TeV/c with maximum intensity between $10\text{-}100\text{ GeV}/c$ [17].

Calibration measurements using cosmic muons as the source of primary ionization in a gas mixture have a few advantages. Muons with $p = 1\text{ GeV}$ passing $x=25\text{ cm}$ of pure isobutane at atmospheric pressure deviate from their original trajectories by a multiple scattering angle $\Theta_{MS} \approx 2.5 \cdot 10^{-4}$ leading to the difference $d = 0.062\text{ mm}$ from a projected destination point assuming there was no scattering. In the miniBETA chamber, mixtures of helium and isobutane are used at a lower than atmospheric pressure. Therefore one can assume that muon trajectories are perfectly straight in the chamber. Additionally, muons provide approximately uniform illumination of the MWDC volume, which is required for the following technique.

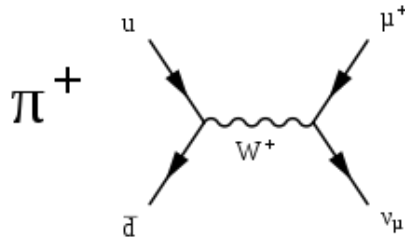


Figure 5.2: Feynman diagram of the leptonic pion decay.

5.2.4 Initial calibration

With the assumption that cells have cylindrical symmetry the uniform illumination condition means that if a large number N_0 of muon trajectories was detected in a given cell of radius R_{max} , all drift distances r should occur with the same probability in the data set:

$$\frac{dN}{dr} = \text{const} = N_0/R_{max},\tag{5.9}$$

Then the following transformation can be used:

$$v(t) = \frac{dr}{dt} = \frac{dr}{dN} \frac{dN}{dt} = \frac{R_{max}}{N_0} \frac{dN}{dt}, \quad (5.10)$$

where $v(t)$ is the drift velocity of electrons from primary ionization towards the anode, r is the drift distance, t is the drift time and N is the number of muons.

Integrating Eq. (5.10) leads to the $r(t)$ relation:

$$r(t) = \int_{t_0}^t v(t') dt' = \frac{R_{max}}{N_0} \int_{t_0}^t \frac{dN}{dt'} dt', \quad (5.11)$$

indicating that the radius r is proportional to the integral of the drift time spectrum. The idea of integrating the drift time spectra in order to obtain the drift time-to-radius relation is based on [80].

Since the detection resolution is finite, there are no perfect edges to the distribution. Especially, at the border of the cell, where the electric field is weak and electrons can wander for some amount of time, the edge of the spectrum is significantly smeared.

To obtain an approximation of the effective border values of t : t_0 and t_{max} , between which the integral can be calculated, an empirical formula describing the drift time distribution in the tube-like cell [81] was used:

$$\frac{dN}{dt} = P_0 + \frac{P_1 \left(1 + P_2 \exp \left(\frac{P_4 - x}{P_3} \right) \right)}{\left(1 + \exp \left(\frac{P_4 - x}{P_6} \right) \right) \left(1 + \exp \left(\frac{x - P_5}{P_7} \right) \right)}, \quad (5.12)$$

where P_i for $i=0, \dots, 7$ are fit parameters: P_0 is the noise offset, P_1 is a scale factor, P_4 and P_5 correspond to t_0 and t_{max} , respectively, P_2 and P_3 depend on the shape of the distribution, while P_6 and P_7 describe its leading and trailing edge slopes.

Figure 5.3 shows a typical drift time distribution for the measurement using cosmic muons with the corresponding shape fitted. The resulting parameters from this fit are:

$$\begin{aligned} P_0 &= 0.0(3.7), \\ P_1 &= 912(61), \\ P_2 &= 1.75(11), \\ P_3 &= 43.1(4.5) \text{ ns}, \\ P_4 &= 185.32(93) \text{ ns}, \end{aligned}$$

$$\begin{aligned}
P_5 &= 427.6(6.6) \text{ ns}, \\
P_6 &= 9.80(22) \text{ ns}, \\
P_7 &= 56.1(3.9) \text{ ns}.
\end{aligned}$$

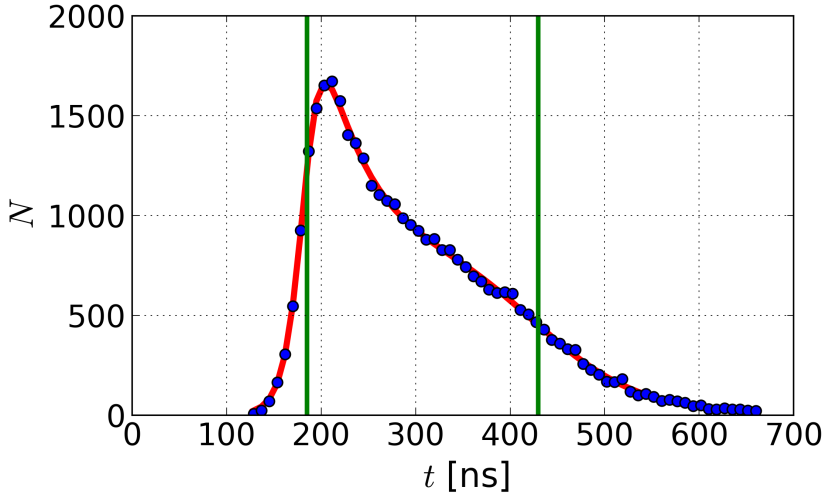


Figure 5.3: Typical drift time spectrum for cosmic muons passing through a single cell with the fitted distribution function (Eq. (5.12)) (red). Vertical lines indicate the values of the parameters $P_4(t_0)$ and $P_5(t_{max})$ obtained from the fit. Due to the fact that the cell is a hexagonal prism (not cylindrical) and the field at cell borders is low, the tail on the right side has no distinguishable edge.

As the values of P_4 and P_5 are used only to give a starting point for the iterative autocalibration, results of this fit are not discussed in this thesis.

Integrating the spectrum according to Eq. (5.11), in the range between t_0 and t_{max} , leads to the initial $r(t)$ calibration. A cubic spline was fitted to parametrize the calibration function. For $t < t_0$ and $t > t_{max}$ the drift distance was set constant: $r(t < t_0) = 0$ mm and $r(t > t_{max}) = R_{max}$. Figure 5.4 presents an example of the initial $r(t)$ relation.

5.2.5 Iterative autocalibration procedure

Since miniBETA cells are not perfect cylinders, the parameters of Eq. (5.12) can only be used as an approximation for determining the $r(t)$ relation and the latter has to be tuned for better performance. The procedure described below, called autocalibration, within a few iterative steps, improves the $r(t)$ relation based on its own accuracy.

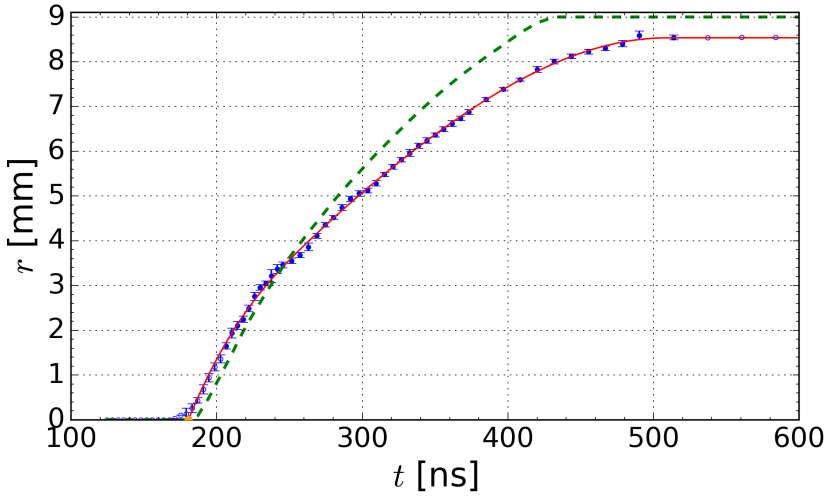


Figure 5.4: Initial (dashed green) and final (solid red) $r(t)$ relation for the exemplary cell (plane 9 wire 5). Blue circles show positions of calibration nodes. Only full circles ($r > 1.5$ mm, $t < 520$ ns) were used in the fit. The orange circle on the horizontal axis marks the t_0 position and was also included in the fit.

During each step, trajectories are fitted individually for each event of the measurement data. A software cut is applied to reject events containing hits from less than 4 planes as well as events with no hits from plane 1 (the most distant from the scintillator), to eliminate trajectories coming from the sides of the chamber and possible noise events. The radius of each hit is determined according to the individual $r_i(t)$ relation of the cell, defined at the beginning of the step (starting with the initial calibration function calculated in Sec 5.2.5). Each event produces a set of residuals Δ_i related to the cells participating in the fitting (Eq. (5.2)). The fit quality ξ is defined by:

$$\xi = \sum_i \Delta_i^2 / \nu, \quad (5.13)$$

where ν is the number of degrees of freedom, which is equal to the number of cells participating in the fit minus 2 (there are 2 parameters in the fit). For the calibration purpose, only trajectories resulting in $\xi < 3$ mm² are included in the tuning procedure. Figure 5.5 shows the initial distribution of ξ and how it evolved with consecutive iterations.

Figure 5.6 presents the initial 2D distribution of pairs $(t, \Delta)_i$ resulting from the fits. An additional index j was introduced to divide the time scale into subsets of equal sizes, centered at t_j , and will be referred to as a node. A

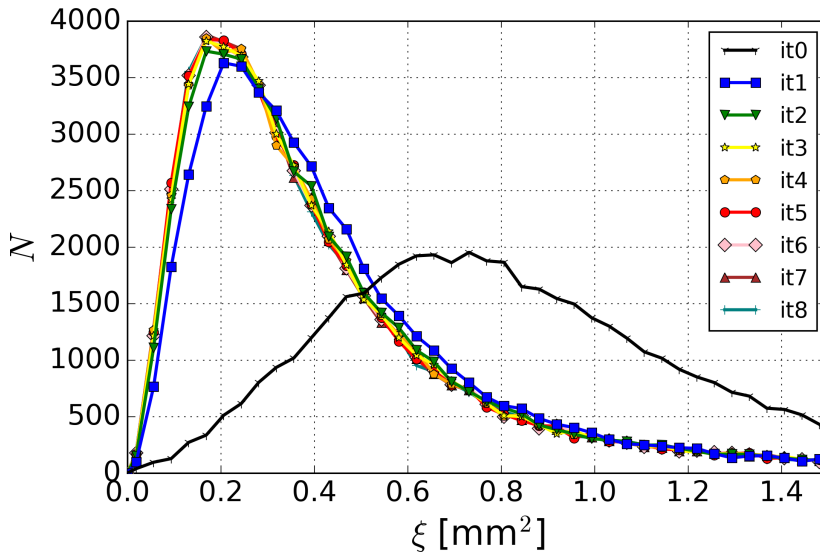


Figure 5.5: Distributions of summed squared residuals of fitted trajectories, divided by degrees of freedom. ‘it0’ refers to values obtained when the initial calibration was used, ‘it1’ after the first iteration step, etc. Lines were added to guide the eye.

residual index j is given by the closest node. Due to the nonlinear nature of the $r(t)$ function, the nodes have a varying width in the r dimension. To compensate the decreasing dN/dt nodes with higher t_j were located further away from each other. Nodes with $t_j \in (125, 250)$ ns were separated by $\Delta t = 4$ ns, for $t_j \in (250, 374)$: $\Delta t = 6$ ns, for $t \in (374, 500)$: $\Delta t = 12$ ns and for $t \in (500, 800)$: $\Delta t = 24$ ns.

For each pair of (i, j) a histogram is created containing residuals with these indices (Fig. 5.7). A skewed normal distribution is fitted to each of the histograms and a mode μ_{ij} is calculated for each distribution. A nonzero value of μ_{ij} indicates that there is a systematic shift in this region that has to be corrected for. Figure 5.6 shows values of calculated μ_{ij} for nodes when the initial calibration is used for muon tracking. The Locally Weighted Scatterplot Smoothing technique (LOWESS) [82] is applied to the data and the corresponding μ'_{ij} are found.

The nodes r_{ij} of individual calibration functions are then shifted according to:

$$r'_i(t_j) = r_i(t_j) + \mu'_{ij}. \quad (5.14)$$

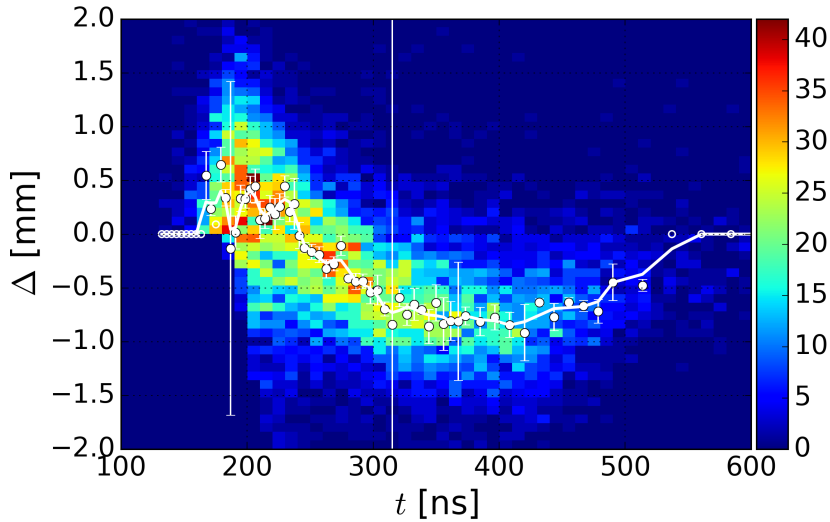


Figure 5.6: Two-dimensional distribution of $(t, \Delta)_i$ pairs when the initial $r_i(t)$ relation was used. The sharp edge of the distribution for $t < 185$ ns occurs due to the fact that there are no trajectories crossing the circle with $r = 0$ mm. White circles represent modes of distributions at each calibration node; the white line is a product of LOWESS (see text). Empty circles mark nodes where the distribution fit failed.

This smoothing helps in maintaining the continuity of the calibration function and the stability of the procedure.

For $r \approx 0$ mm, distributions of residuals are distorted because positive values are favored, since the possibility of a trajectory passing outside the circle is higher than for the one crossing it. In the extreme: if $r = 0$ mm only trajectories outside the circle can exist, hence only positive residuals are obtained. In order to minimize this systematic shift on the calibration, only nodes with $r'_{ij} > 1.5$ mm were used and $t_{i,0}$ where $r_i = 0$ was found independently (Sec. 5.3.3) and added to the remaining nodes.

A cubic spline is fitted to the selected $r'_i(t)$. The function is additionally flattened outside of the region used in the fit, in order to eliminate nonphysical behaviors, i.e. arms bending and obtaining negative radii (Fig. 5.4). The resulting function provides the next iteration of $r_i(t)$ relation.

The autocalibration procedure is then repeated until convergence is achieved, i.e. the distribution of fit quality ξ no longer improves. Additionally, a correction

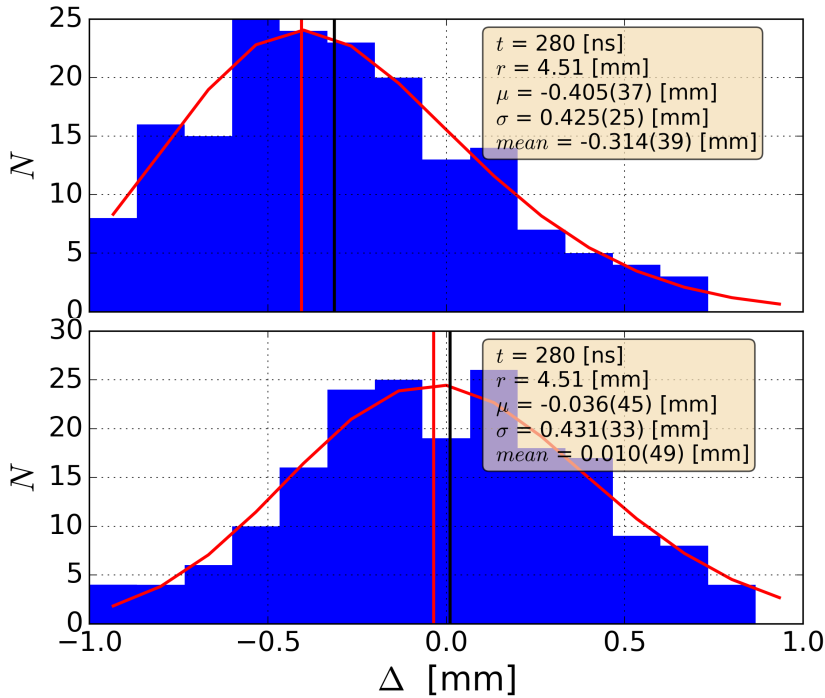


Figure 5.7: Distribution of residuals Δ_{ij} obtained with (top) the initial and (bottom) the final $r(t)$ relation for the given node (its location (t, r) is given in the legend) with fitted probability density function of a skewed normal distribution (solid red line). The vertical red line marks the position of the distribution mode and the black line its mean value. Square root of the distribution variance is also given in the legend as σ .

for possible signal wire misalignment (Sec. 5.3.4) is calculated every second iteration step and positions of cell centers are shifted accordingly.

It was found that 5 iteration steps are enough and no further improvement will be obtained with more steps (Fig. 5.5). Figure 5.4 shows both the initial and the final drift time-to-radius relation for the exemplary cell. The largest differences are visible in the region of larger r values due to the poor initial calibration approximation in the region of the non-cylindrical field. Figure 5.8 shows the final distribution of $\Delta_i(t)$.

To visualize the final result of the autocalibration a distribution of pairs (t, d_s) with the overlayed $r(t)$ relation is presented in Fig. 5.9. One can notice that the

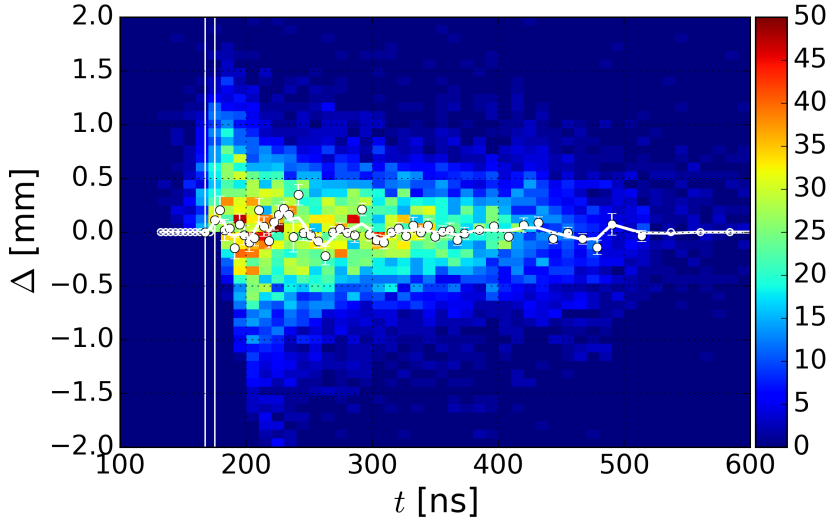


Figure 5.8: As Fig. 5.6 but after the 5th iteration step. The greatest deviation from $\Delta = 0$ mm is observed at $t = 230$ ns and it is ~ 0.25 mm.

fitted distances d_s (Eq. (5.7)) group around $r(t)$ which indicates good accuracy of the calibration.

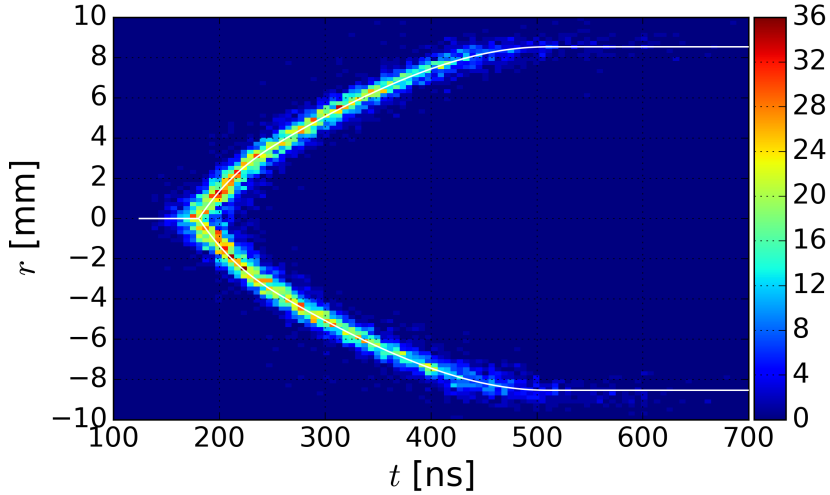


Figure 5.9: Two-dimensional histogram of (t, d_s) pairs obtained for the exemplary cell when the final $r(t)$ relation (plotted as a white line) was used in the analysis of cosmic muon trajectories.

Figure 5.10 shows initial distributions of d_s , Δ and (d_s, Δ) pairs for the exemplary cell. This kind of plot is useful to determine whether the used $r(t)$ relation was accurate. If the relation was correct the distribution of (d_s, Δ) would lie along the $\Delta = 0$ mm axis. In the figure, a systematic shift of the distribution from the $\Delta = 0$ line is visible which indicates that the initial $r(t)$ calibration requires a correction. In addition, due to the uniform illumination of the cell, the histogram of d_s should have a rectangle-like shape. It is not exactly the case with the initial calibration since fluctuations in $\frac{dN}{dd_s}$ are higher than it would result from the counting statistics. Figure 5.11 shows these distributions when the final $r(t)$ relation was used. An improvement in the $r(t)$ accuracy is clearly visible and $\frac{dN}{dd_s}$ is more uniform than before.

Figure 5.8 shows that there are still some systematic trends in fit residuals. It is possible to set fit parameters in a way that would make the spline pass closer to all nodes, regardless of their uncertainties. This leads to the $r(t)$ relation taking a more “step-like” shape. Although it flattens μ_{ij} , it creates big fluctuations in the $\frac{dN}{dd_s}$, which indicates that this approach should not be taken.

It is believed that the method of grouping residuals by the closest node and approximating their distribution with the skewed normal distribution might lead to these discrepancies, however, it was not definitely proven nor was a better solution proposed. Additionally, Figs. 5.11 and 5.9 suggest that better results might be obtained without the radial symmetry approximation because some differences are visible between the regions on the left and on the right from the cell center when the sides are distinguished. The remaining systematic shifts were found to be $\mu_{ij} < 0.1$ mm for the vast majority of the chamber detection region, which was considered sufficiently low in the scope of this project.

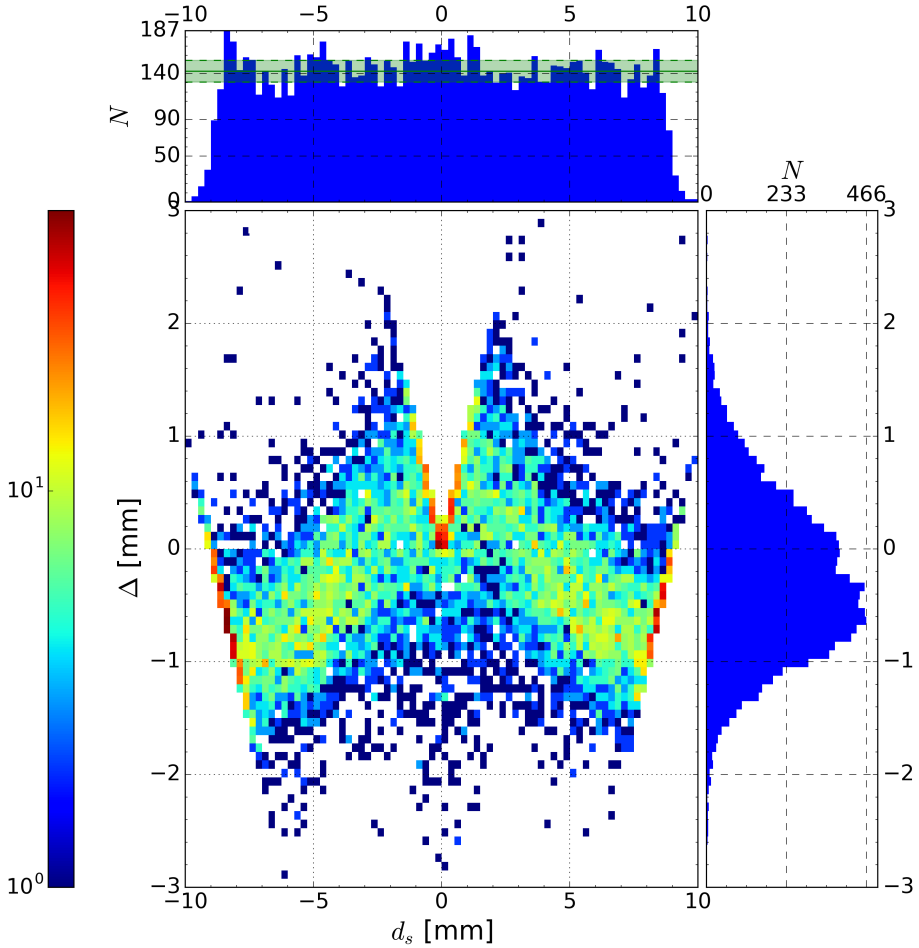


Figure 5.10: Plots showing distributions of d_s , Δ and (d_s, Δ) pairs for the exemplary cell when the initial $r(t)$ relation is used during muon trajectories fitting. A green line on the histogram of d_s marks the average of bin counts $\langle N \rangle$ and dashed lines highlights the region of $(\langle N \rangle - \sqrt{\langle N \rangle}, \langle N \rangle + \sqrt{\langle N \rangle})$.

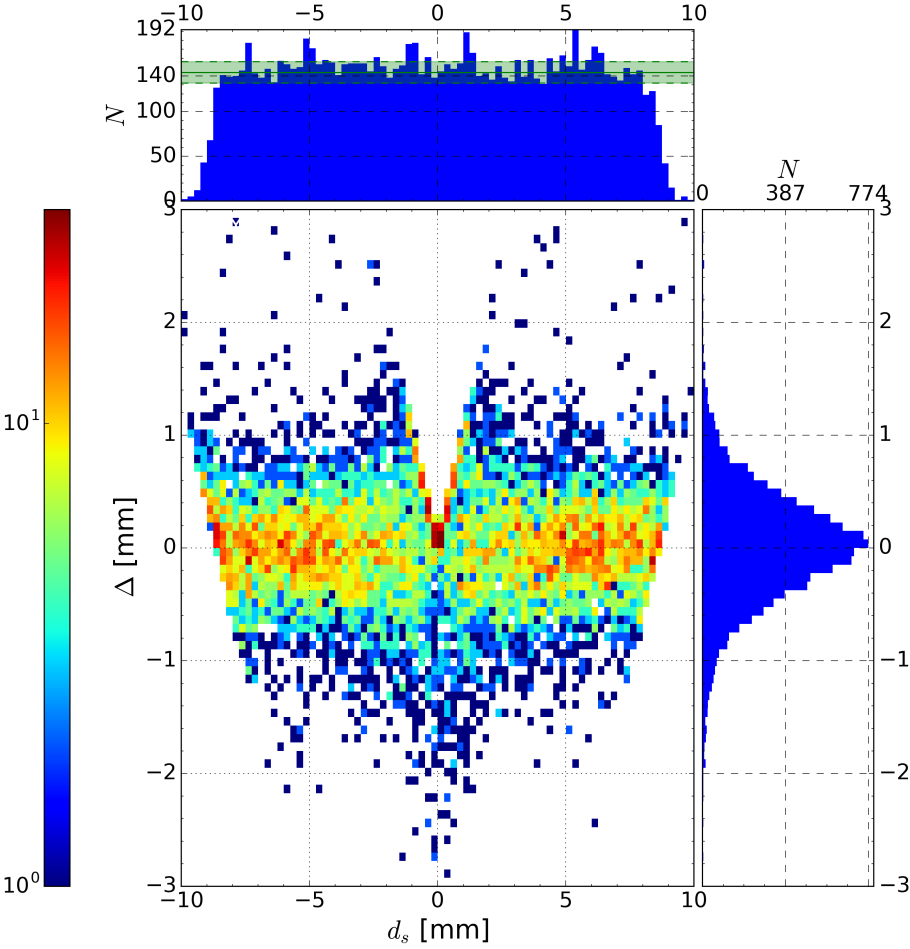


Figure 5.11: As Fig. 5.10 but for the final $r(t)$ relation used during muon trajectory fitting.

5.3 Systematic errors affecting the drift time-to-radius relation

5.3.1 Correction of the “time walk” effect

The “time walk” effect occurs if a leading-edge threshold discriminator is used to produce a START or a STOP signal for a TDC and incoming signals vary in heights (Fig. 5.12). The higher the signal the earlier it will be detected. Without any correction, this can lead to a systematic uncertainty of the measured drift time. For signals with identical rise times and peak shapes one can use a constant fraction discriminator, which cancels the “time walk”. However, rise times of signals from the miniBETA drift chamber vary significantly (Fig. 4.7), so that this solution was not suitable.

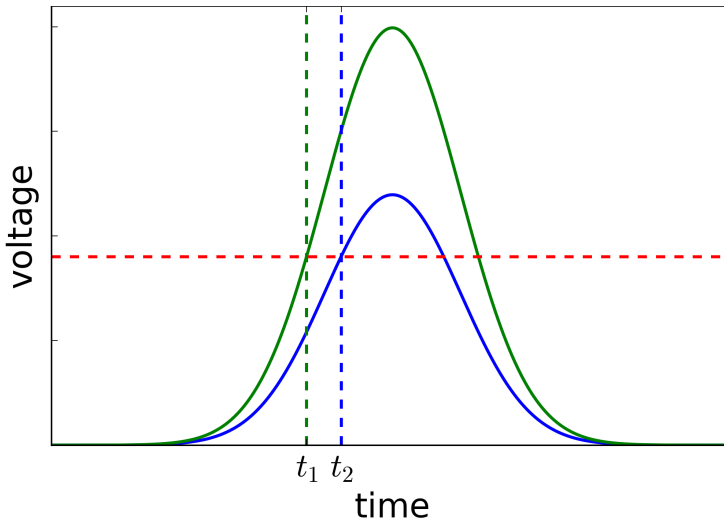


Figure 5.12: Illustration of the “time walk” effect. Two Gaussian signals differing in height pass the threshold (red dashed line) at two different moments t_1 and t_2 .

A custom made electric circuit generating a signal similar to signals coming from the drift chamber was used to find a correction for this “time walk” effect on the individual channels. The generator allowed to change the height of the signal and was connected to a single DAQ channel. It also produced a step signal to trigger the DAQ, replacing the PMT signal. The delay between these signals was fixed. Similarly to regular operation, the DAQ was measuring the

height V of the voltage signal (in analog-to-digital units, ADU) and the time t between the trigger detection and the passing of the threshold by the voltage signal. For each voltage level ~ 50000 events were recorded and mean values of V and t and their uncertainties were calculated.

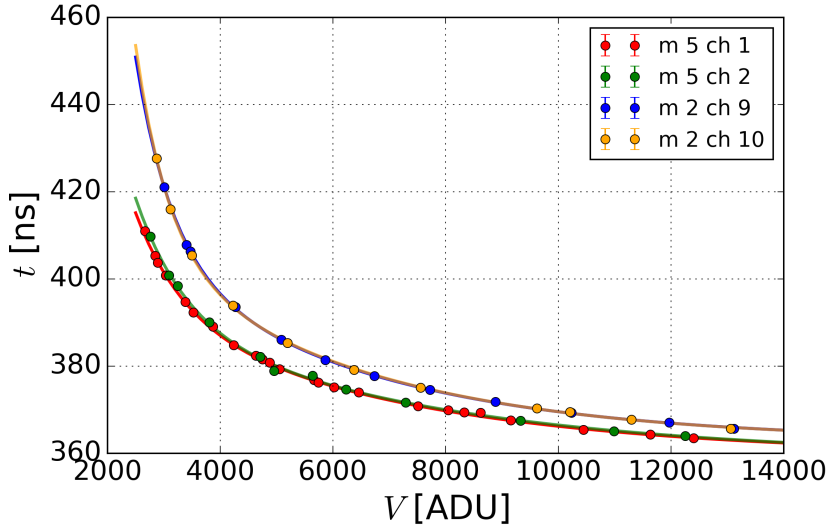


Figure 5.13: Measured relation between the signal height V and the time t that passed between detection of the trigger signal and the moment of the wire signal passing the discriminator threshold. The sum of two exponents (Eq. (5.15)) was fitted (solid lines). The legend describes the color coding associated with the DAQ modules (m) and their channels (ch).

The obtained data points were plotted and a sum of two exponential decays was fitted in order to parametrize the relation:

$$t = A_0 + A_1 \exp(\lambda_1 V) + A_2 \exp(\lambda_2 V), \quad (5.15)$$

where A_0, A_1, A_2, λ_1 and λ_2 are fit parameters. Figure 5.13 shows the measured relation between V and t with the fitted line for a few selected channels. Fitted parameters for channel 1 in module 5 (which reads the signal from side A of wire 1 at plane 5 during the regular chamber operational mode) are:

$$\begin{aligned} A_0 &= 359.40(82) \text{ ns}, \\ A_1 &= 54.3(4.0) \text{ ns}, \\ A_2 &= 450(120) \text{ ns}, \\ \lambda_1 &= -2.08(18) \cdot 10^{-4} \text{ ADU}^{-1}, \\ \lambda_2 &= -1.18(12) \cdot 10^{-3} \text{ ADU}^{-1}. \end{aligned}$$

The DAQ is triggered by the sum of signals $Q = V_a + V_b$ from the preamplifiers at both ends of a wire. In the test setup $Q = V_{a(b)}$, since there was no signal on the counterpart channel.

The parameter A_0 is the sum of the initial delay between the generated signals and the delay in the electronics for the exemplary channel. This parameter is not interesting for the “time walk” correction, because this is a constant which is anyhow canceled during the $r(t)$ calibration. The final correction is calculated from the formula:

$$W(Q) = A_1 e^{\lambda_1 Q} + A_2 e^{\lambda_2 Q}, \quad (5.16)$$

Every detected drift time t has to be corrected by:

$$t' = t - W(Q). \quad (5.17)$$

The correction can reach up to 40 ns for the smallest, yet triggering signals. A typical drift time spectrum in the miniBETA drift chamber is ~ 300 ns wide (Fig. 5.15). Not including this correction would result in the systematic error for the drift distance $\sim \frac{40}{300} \cdot 8.67 \text{ mm} \approx 1.15 \text{ mm}$, for the smallest signals. Incorrect drift distance calculation affects the determination of the electron’s trajectory, hence the extrapolated position where the scintillator was hit influencing the energy readout (Sec. 7.3).

Calibration of the walk effect for individual channels is a cumbersome and time-consuming procedure. It was therefore investigated how large systematic uncertainties would be when applying a common (unified) walk correction instead of individual ones. First, the parameter $A_{0,i}$ was subtracted from each drift time, where the $A_{0,i}$ value was taken from the previous fit of two exponents (Eq. (5.15)) for the channel i . These parameters were different for each channel and were needed to cancel individual delays generated by the electronics. Then, the same parametrization (Eq. (5.16) based on the fit for module 5 channel 1) was used to correct for the “time walk” (Eq. (5.17)) in each channel. Results are presented in Fig. 5.14.

One can notice, that for both channels in module 5 the “time walk” effect is fully canceled after the correction, which is obvious for that individual case. For module 2, the “time walk” is not fully canceled for smaller signals, but it quickly reaches zero, such that about 93% of the events are fully compensated during the regular operation mode of the miniBETA drift chamber (Fig. 5.15).

In this thesis, only a few channels were separately tested for the influence of the “time walk” effect which, if uncorrected, could lead to a decrease in the drift time resolution, hence a worse spatial resolution. However, the final resolution (Sec. 5.4.1) is experimentally determined and includes all possible uncompensated factors. No significant difference between the cells was observed, hence the

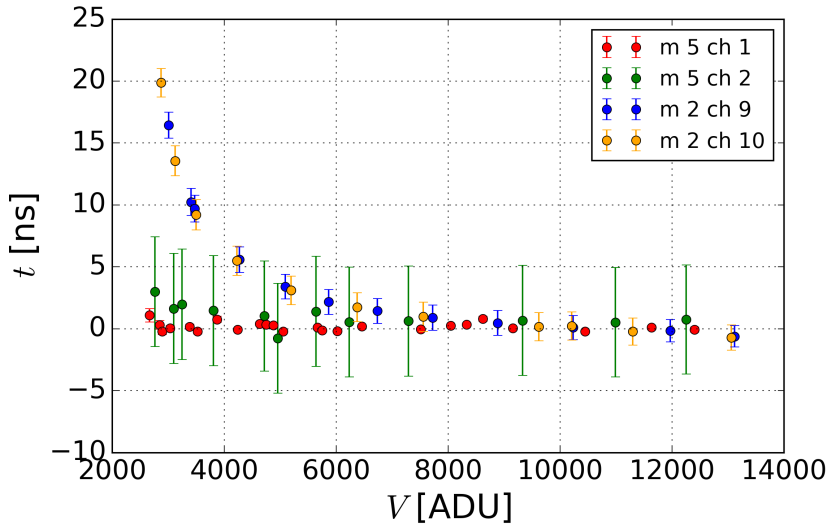


Figure 5.14: Systematic uncertainty which is the result of the common parametrization (based on the data from module 5 channel 1) being used to compensate for the “time walk” effect in all of the measured channels.

conclusion, that one common parametrization of the “time walk” effect can be applied safely to all channels. Nevertheless, this effect might require further analysis, individually for each channel, since a correlation between Q and r is observed, both in the data and in the simulation [55]. The average signal height drops down significantly close to the cell borders (see Fig. 5.31 in 5.4.3), which means that the tracking in this region is more prone to the walk effect.

5.3.2 Problem with trajectories parallel to traversed cell centers

During the analysis of the autocalibration results a systematic behavior was observed: a lack of detected hits at certain positions (x_L, y_L) in all the cells, visible as a white line in 2D histograms of (x_L, y_L) pairs (Fig. 5.16). This indicates that there must be some correlation between the fit accuracy and the slope a of the muon trajectory.

The cause of the problem was found when a 2D histogram of the fitted trajectory parameter pairs (a, b) was investigated (Fig. 5.17). A parallelogram shape of trajectory parameters results from the detection geometry. Unexpectedly, one can find holes with missing counts, located around $a \approx \pm 0.58 \approx \pm 1/\sqrt{3}$. These

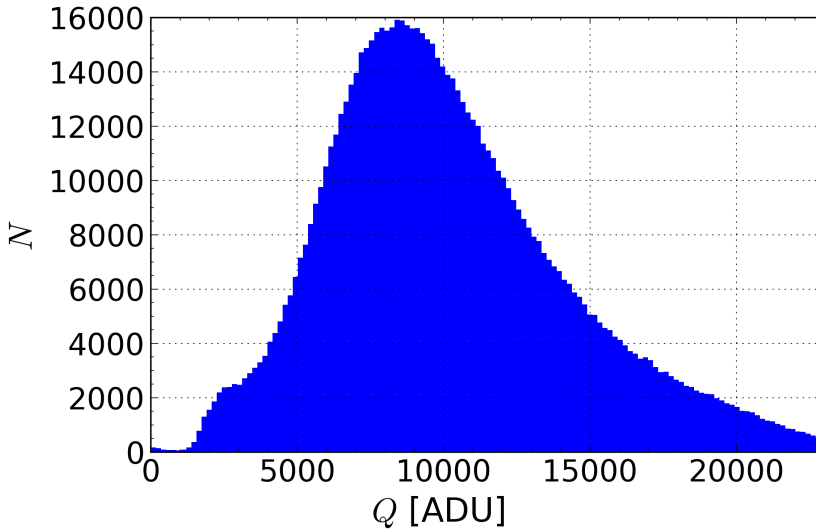


Figure 5.15: Histogram of Q for the exemplary wire for signals collected during the measurement with ^{207}Bi source and the chamber filled with 50/50 He-Iso mixture at 600 mbar. Signals with $Q > 5000$ ADU (where the “time walk” effect is considered to be fully compensated) constitute 93% of the whole.

values correspond to the set of lines that pass all the traversing cells at the same distance from their centers. The problem with this kind of trajectories is known in the literature as “left-right ambiguity”. The ambiguity is caused because two trajectories fit the data equally good if the cell centers participating in the event lie on a single straight line.

In order to avoid this problem drift chambers are constructed in a way that every second layer is shifted so that consecutive cell centers do not lie on the same line anymore. This shift was also included in the miniBETA chamber geometry by using the “honeycomb” structure of the cells. However, trajectories with $a \approx \pm 0.58$, passing through cells which centers are aligned, will still suffer from the “left-right ambiguity”. In order to avoid this problem only trajectories with $a \in (-0.3, 0.3)$ were arbitrarily selected in the autocalibration procedure, and results presented in this thesis already include this cut.

5.3.3 Determination of t_0

The method of calibrating the $r - t$ relation described in the previous section cannot be used in the region close to the cell center. The sign of the residual Δ

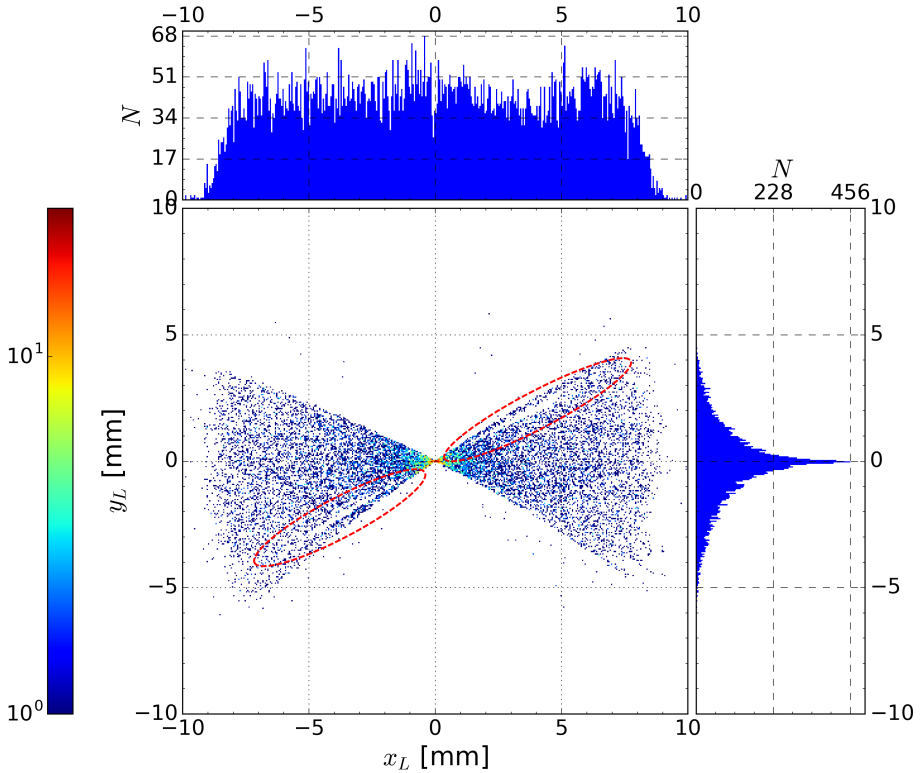


Figure 5.16: Two-dimensional histogram of coordinates pairs (x_L, y_L) showing all the calculated hit positions in the exemplary cell for the cosmic muon measurement. The origin of the coordinate system was set at the cell center. Red dashed ellipses were added to mark the region of missing points.

is positive if the fitted trajectory passed outside of the circle given by the $r(t)$ relation ($d > r$) and negative when the trajectory crossed the circle ($d < r$) (Eq. 5.2). The residual distribution can then no longer be approximated by a skewed Gaussian for low drift times as the probability of $d < r$ is getting lower, up to the extreme at $r = 0$ mm, where only $\Delta \geq 0$ can exist since it is not possible to obtain $d < 0$ mm. This effect is visible in Fig. 5.8 in the bottom left part of the (t, Δ) distribution and in Fig. 5.11 above the center of the (d_s, Δ) distribution.

Extrapolation of the fitted spline up to $r = 0$ mm is unreliable, hence a different approach was taken. For each cell i only hits from trajectories passing close to the cell center, i.e. with $d_{i,s} \in (-0.5, 0.5)$ mm, were selected and their drift times were histogrammed (Fig. 5.18). A skewed normal distribution was fitted

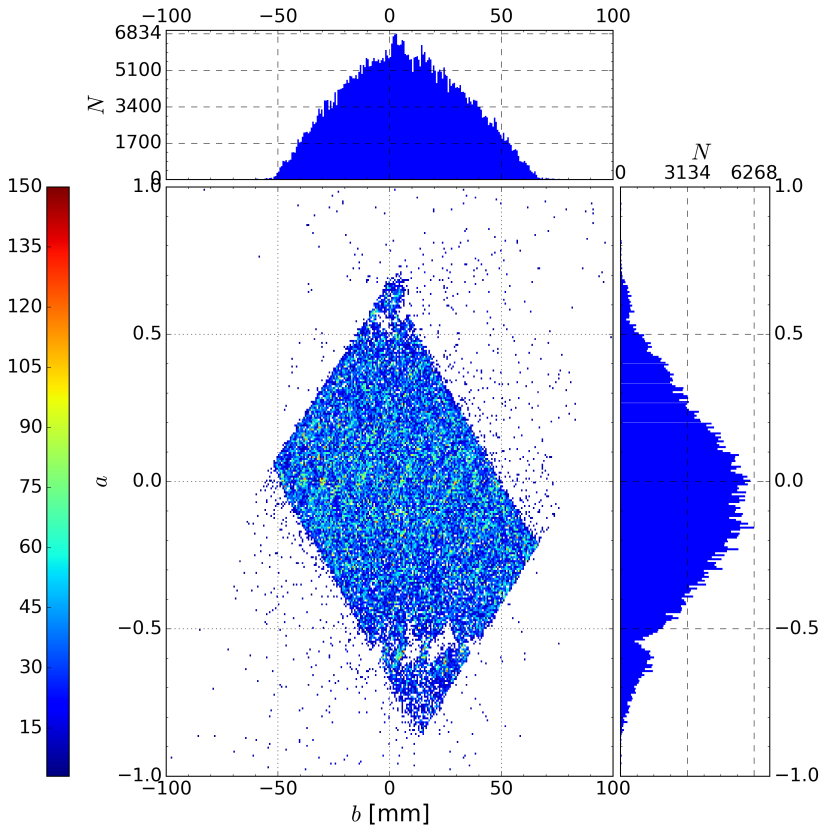


Figure 5.17: Two-dimensional histogram of fit parameter pairs (b, a) of cosmic muons trajectories.

and its mode $\tau_{i,0}$ calculated. It was assumed that $r_i(\tau_{i,0}) = 0$ mm and this point was added to the spline fit as one of the calibration nodes.

5.3.4 Correction for the misalignment of signal wires

Wires of the MWDC are manually soldered to the thin guiding pads on the PCB boards. The mechanical precision of their alignment was estimated as $\sigma_{i,0} \sim 0.1$ mm. During the data analysis a systematical shift was observed between the mean value of residuals corresponding to trajectories passing on the left and on the right side of the cell center (Fig. 5.19). It appeared that if the trajectory passed on the right side the residual distribution mean value

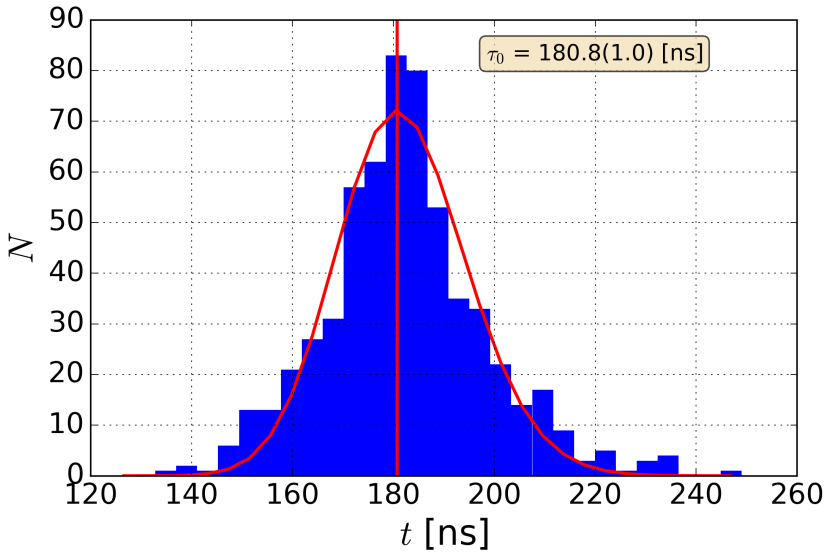


Figure 5.18: Histogram of drift times for hits registered in the neighborhood of the cell center: $d_s \in (-0.5, 0.5)$ mm with the fitted skewed normal distribution. The vertical red line marks the position of the distribution mode.

was mostly positive and mostly negative for the other side. This shows that the fitted trajectory, systematically for all d_s , passed more frequently on the right side of the position determined by the $r(t)$ relation. It was concluded that the actual position of the signal wire was different from the one used in the analysis, hence the systematic shift in the fit residuals. The autocalibration procedure is blind to this effect because there is no left-right distinction included and shifts from both sides cancel each other giving $\langle \Delta \rangle = 0$ mm.

An additional step was introduced between every second calibration iteration in order to correct for the wire position misalignment δ . Figure 5.20 shows distributions of Δ_x , Δ_y and (Δ_x, Δ_y) (Eq. (5.8)) for the exemplary wire before the first correction. A skewed normal distribution is fitted to the Δ_x histogram. The mode of the fitted distribution is used as a correction δ_x for the wire x-coordinate. The wire y-coordinate correction δ_y was calculated as the mean value of the Δ_y distribution since the shape of the distribution cannot be reliably approximated by the normal nor the skewed normal one. Shifting cell center positions twice was enough to eliminate the misalignment. It was found that the y-coordinates are equal to 0 within their uncertainty limits ($\sim 10^{-3}$ mm). The total correction δ_x and an average t correction per plane $\langle \delta_x \rangle$ is given in Tab. 5.1.

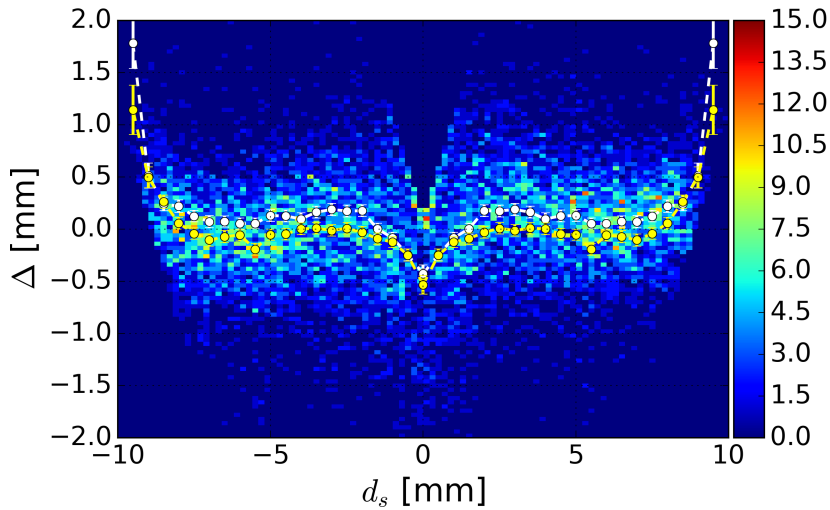


Figure 5.19: Two-dimensional histogram of (d_s, Δ) pairs for muon trajectories, after the autocalibration procedure, without the correction for the wire position. White points marks mean values of distribution slices calculated for $d_s > 0$ mm, for $d_s < 0$ mm values were mirrored. Yellow points are analogically calculated for $d_s < 0$ mm, and mirrored for $d_s > 0$ mm. Dashed lines were added to guide the eye.

The uncertainty of the distribution mode, which after the shifts equals 0 mm, is taken as the uncertainty of the required total correction as well as the uncertainty of the corrected wire position. The average shift per plane $\langle \delta_x \rangle$, calculated as a weighted average of the corresponding wires corrections, differs from 0 for most of the planes. This leads to the conclusion that the wires misalignment comes mostly from the shift of the whole plane, rather than from the positioning of individual wires. This is understandable because the method of the plane positioning has limited precision. After the correction the systematic shift between the left and the right part of the cell present in Fig. 5.19 is no longer visible. As a result, the muon measurement allowed to increase the accuracy of the signal wire positions by almost an order of magnitude.

5.3.5 Effects correlated with the total height of a signal

After the final calibration, the drift time-to-radius relation allows to look for some additional correlations and systematic trends in the r dimension. The correlation between the total height of the signal $Q = V_1 + V_2$ and the drift

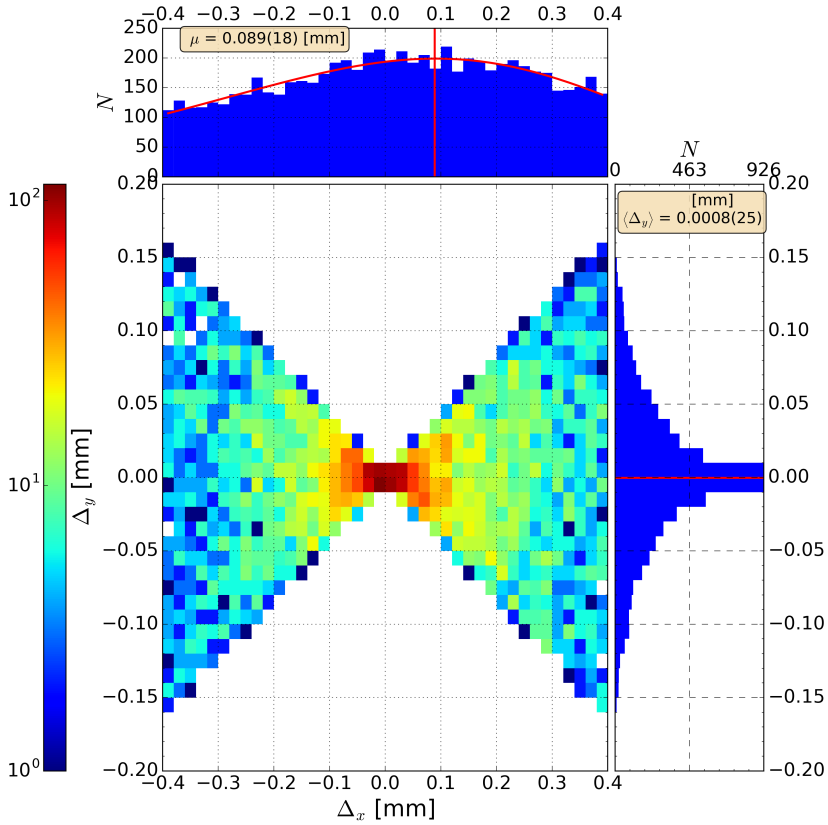


Figure 5.20: Histograms of (Δ_x, Δ_y) , Δ_x with fitted skewed normal distribution and a line marking its mode, and Δ_y with a line marking its mean value. Plots show results of the autocalibration procedure when the cell center correction was not applied.

radius r has been analyzed. Figure 5.21 presents an example of a 2D histogram of pairs (r, Q) .

A trend is visible: Q is slowly decreasing with r and the slope gets gradually steeper for $r > 5$ mm. One can also notice, that there are almost no signals with $Q < 5000$ ADU for $r < 7$ mm and almost only such for $r > 7$ mm, which indicates that the signals related to trajectories passing close to the cell borders are more prone to the walk effect (Fig. 5.14). The drop of the detection efficiency at the cell borders (Sec. 5.4.2) is also correlated with the drop of Q in that region.

Table 5.1: Table showing the total correction δ_x required to align the wire position, based on the measurement of cosmic muon trajectories. The weighted average $\langle\delta_x\rangle$ is also shown for each plane. All values are in mm. $\delta_x = 0(10)$ mm means that the correction could not be calculated for the corresponding wire.

		plane				
		1	2	3	4	5
wire	1	0.000(27)	0.148(31)	0(10)	-0.023(24)	0(10)
	2	-0.087(31)	0.005(53)	0.038(28)	-0.054(27)	0.011(37)
	3	0.053(34)	0.115(46)	0.086(24)	-0.059(24)	0.000(30)
	4	0.000(25)	0.111(26)	0.000(22)	-0.117(21)	-0.045(22)
	5	0.032(24)	0.050(27)	0.038(23)	-0.079(23)	0.010(17)
	6	-0.046(25)	0.115(35)	0.017(31)	-0.035(26)	-0.025(19)
	7	0.036(28)	0.112(28)	0.071(21)	-0.139(24)	-0.052(21)
	8	0.008(28)	-0.015(48)	-0.139(51)	0(10)	0.205(40)
$\langle\delta_x\rangle$		-0.0008(96)	0.093(12)	0.0364(97)	-0.0761(90)	-0.0086(87)
		plane				
		6	7	8	9	10
wire	1	-0(10)	0(10)	0(10)	0(10)	0(10)
	2	-0.037(27)	-0.107(31)	0.024(21)	-0.282(68)	0.114(26)
	3	-0.088(29)	-0.087(22)	-0.029(19)	0.108(23)	0.064(16)
	4	-0.112(21)	-0.074(17)	0.044(23)	0.032(20)	0.026(21)
	5	-0.103(21)	-0.079(14)	-0.015(15)	0.090(15)	0.059(17)
	6	-0.090(18)	-0.092(21)	-0.063(19)	0.076(26)	0.000(28)
	7	-0.148(23)	-0.054(17)	-0.192(27)	0.065(42)	-0.085(41)
	8	0(10)	-0(10)	0(10)	0(10)	0(10)
$\langle\delta_x\rangle$		-0.0991(91)	-0.0775(76)	-0.0296(81)	0.0694(94)	0.0481(88)

In addition, 2D histograms of (Q, Δ) pairs were analyzed for each cell in search of any uncompensated correlation between these variables (Fig. 5.22). The Pearson correlation coefficient r_P was found to be ~ 0.25 for all the cells. This suggests that some small correlation between Q and Δ is still present in the data although its effect was considered negligible within the achieved detection resolution (Sec. 5.4.1).

Table 5.2 summarizes issues related to the systematic effects which were considered as important and affecting the $r(t)$ calibration, together with the solutions which were applied and estimates of the resulting uncertainties.

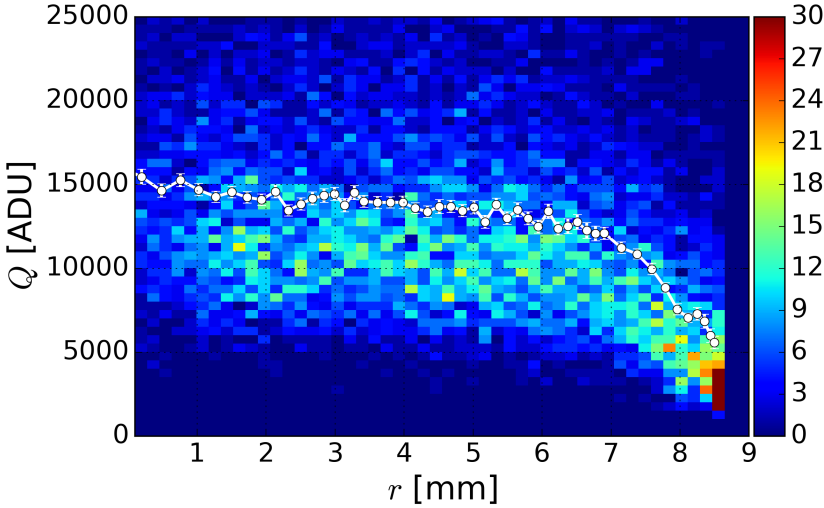


Figure 5.21: Two-dimensional histogram of (r, Q) pairs for the exemplary cell. The color scale was capped at 30 to increase the visibility. White circles shows mean values of Q distributions at calibration nodes. The line is added to guide the eye.

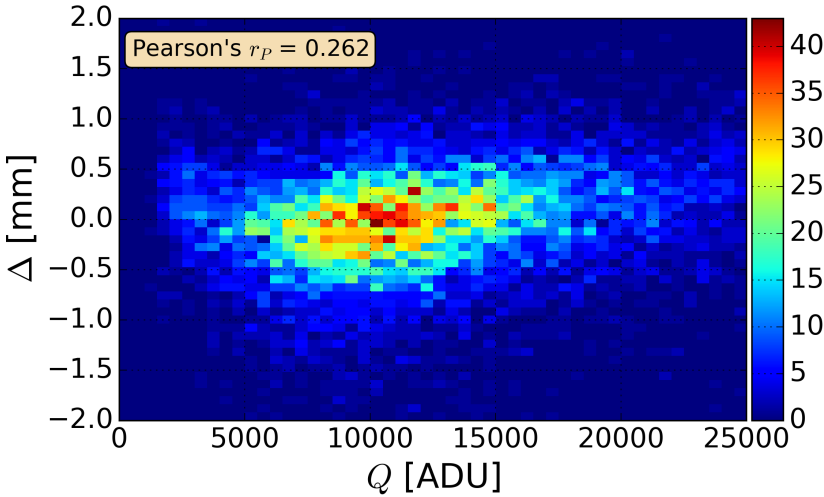


Figure 5.22: Two-dimensional histogram of (Q, Δ) pairs for the exemplary cell.

Table 5.2: Summary of the issues related to the systematic effects and the solutions which were applied. The size of the correction Δ and the estimated order of the uncertainty σ of these corrections are also given in the table. References to the appropriate sections are provided in the column labeled ‘Sec.’. ‘N/A’ states ‘not applicable’.

Issue	Solution	Δ [mm]	σ [mm]	Sec.
time walk	applying the correction function determined in the dedicated measurement	up to 1	0.1	5.3.1
left-right ambiguity	discarding trajectories with the slope $a \notin (-0.3, 0.3)$	N/A	N/A	5.3.2
determination of t_0	t_0 calculated from distributions of drift times corresponding to trajectories passing in the vicinity of a wire	N/A	0.1	5.3.3
signal wires’ misalignment	applying corrections based on distributions of trajectory residuals in x - and y -dimensions	up to 0.2	0.02	5.3.4

5.4 Results

5.4.1 Position resolution

For given conditions (i.e. the gas mixture composition and the applied HV on the signal planes), the position resolution of the i -th cell at the node j was defined as the standard deviation σ_{ij} of the distribution of residuals Δ_{ij} obtained from fitting cosmic muon trajectories with the final $r_i(t)$ relation. It was found that these distributions can be asymmetric, hence they were approximated by a skewed normal distribution (Fig. 5.7). A typical function $\sigma_i(r)$ (Fig. 5.23) starts from ~ 0.6 mm in the proximity of the signal wire, where the drift velocity (Eq. (3.10)) is the greatest and the primary ion statistics (Eq. (3.8)) has the strongest influence, and decreases to ~ 0.4 mm for $r > 4$ mm. The further drop is compensated by electron cloud diffusion (Eq. (3.11)).

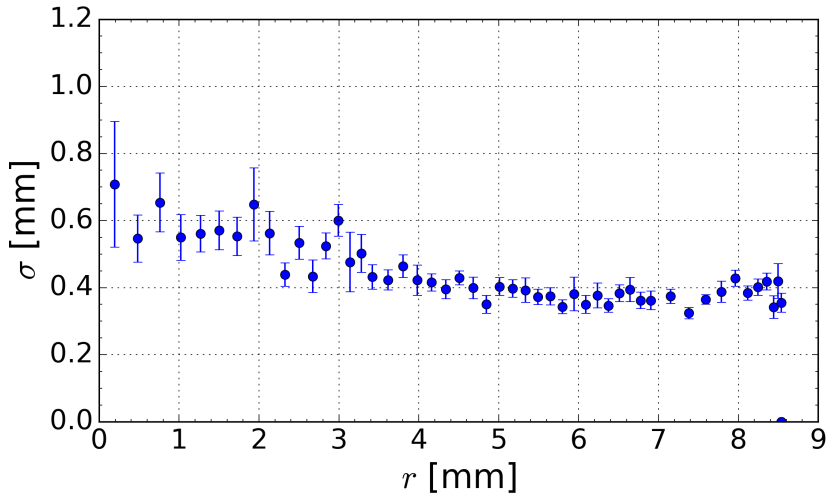


Figure 5.23: Position resolution σ of the exemplary cell as a function of the drift radius r .

5.4.2 Efficiency

The electric field is weaker in the vicinity of cells boundaries, hence ionized electrons wander longer in these regions, can migrate to the neighboring cell or even get lost. In addition, the field varies between cells. Therefore, the efficiency $\eta_i(r)$ was calculated individually for each cell as a function of the drift radius. Fitted trajectories of cosmic muons were used to calculate the chamber efficiency.

For each event, a set of cells was selected through which the ionizing particle passed. If the trajectory is crossing the cell i the node index j is assigned, based on the node being the closest to the measured drift time, and a variable $N_{ij,total}$ is incremented by one. If this cell delivered a signal that participated in the trajectory fitting, a variable $N_{ij,fired}$ is also incremented by one. The single cell efficiency η is calculated as:

$$\eta_{ij} = \frac{N_{ij,fired}}{N_{ij,total}}. \quad (5.18)$$

Figure 5.24 presents exemplary behavior of $\eta_i(r_j)$. The single cell efficiency is higher than 0.99 for most of the cell volume and rapidly drops down for $r > 7$ mm.

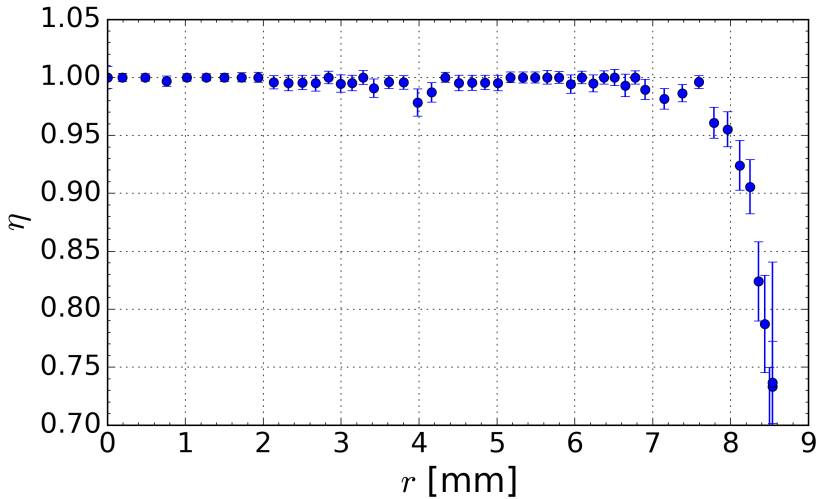


Figure 5.24: Single cell efficiency η as a function of the drift radius r .

Figure 5.25 shows a 2D histogram of the calculated (x_l, y_l) pairs (Eq. 5.6), visualizing all the positions where the muon trajectories were detected, with casts at x - and y -axis. Positions of signal wires are also marked in the picture. One can notice count drops in the x cast at the marked positions due to the efficiency drop at cell edges (edges and centers of consecutive cells are aligned). Step drops at $x \approx -40$ and $x \approx -50$ mm result from broken preamplifiers on wire no. 8 at planes 4 and 9.

In addition, a mean cell efficiency $\bar{\eta}_i$ was calculated for each cell:

$$\bar{\eta}_i = \frac{\sum_j N_{ij, \text{fired}}}{\sum_j N_{ij, \text{total}}}. \quad (5.19)$$

Figure 5.26 shows the calculated mean efficiency of each cell in the chamber. A table with numbers is located in Appx. A. For most of the cells (66 out of 80) $\bar{\eta}_i > 0.97$ was achieved.

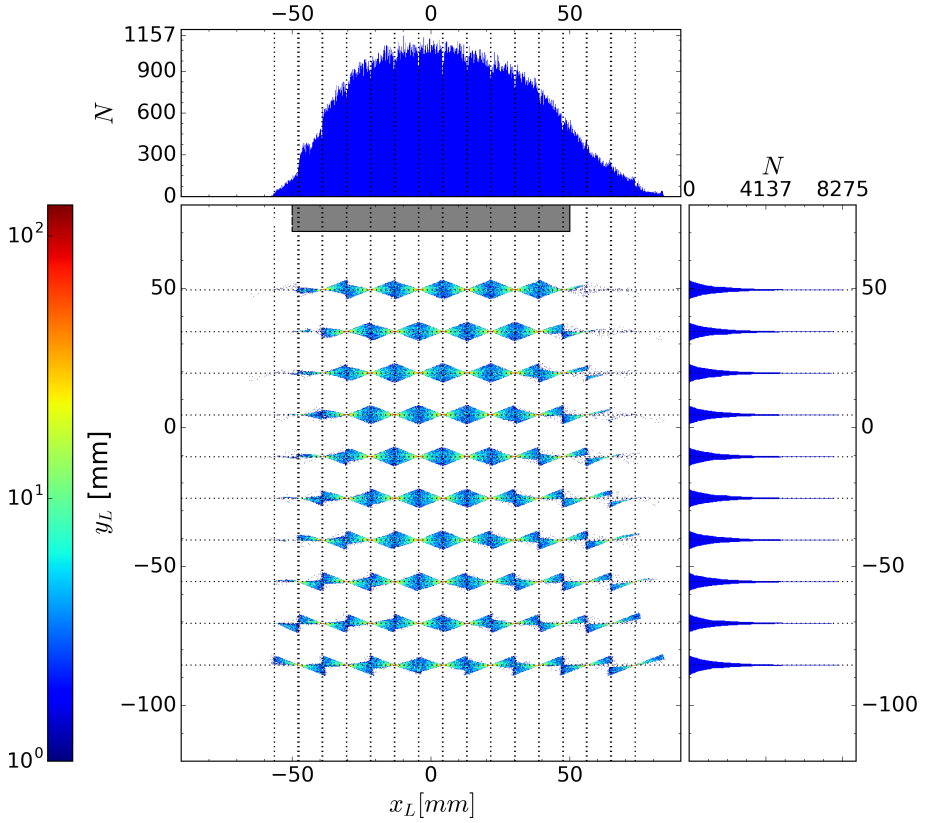


Figure 5.25: Two-dimensional histogram of (x_l, y_l) pairs, visualizing all the positions where muon trajectories were detected, with casts at x and y axis. Positions of signal wires are marked by dotted black lines.

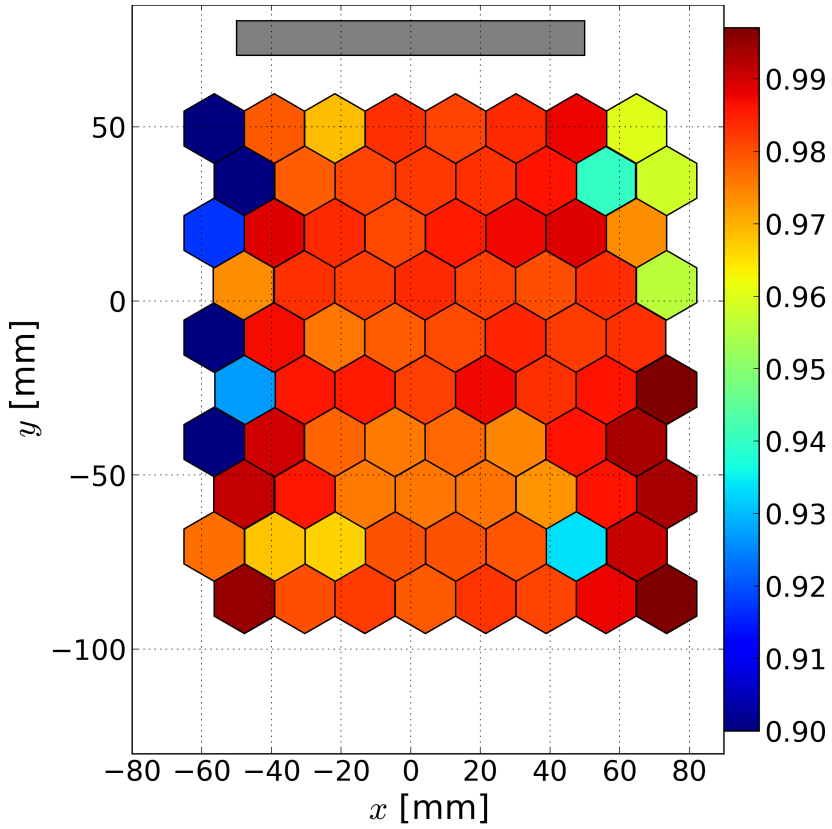


Figure 5.26: Visualization of mean cell efficiencies. The majority of cells reached $\bar{\eta}_i > 0.97$. Efficiencies of cells at plane 4 wire 8 and plane 9 wire 8 were ~ 0.3 due to the fact that they had a faulty preamplifier on one of their wire ends.

5.4.3 Comparison of results obtained with different gas mixtures filling the chamber

The miniBETA tracking in the xy -projection, based on measurements of drift times of electrons created along the ionizing particle trajectory, had been commissioned for the following helium-isobutane mixtures: 50/50 and 70/30 at 600 mbar and 50/50 and 0/100 at 300 mbar. The number of registered, accepted and rejected events in each set is given in Tab. 5.3.

Most events were rejected by the “no P1” cut, clearing the data from events that did not provide a signal on plane 1. This cut filters out muons coming from the sides of the chamber, the xy -projections of which would show missing cells along the trajectory and would falsely decrease the calculated detection efficiency. The “ $a \notin (-0.3, 0.3)$ ” cut filters out trajectories that can cause a “left-right ambiguity” problem (Sec. 5.3.2). Events with a low number of hits (< 6), which are vastly noise-related, are filtered out as well by the “ $\nu < 4$ ” cut. Finally, trajectories with fit quality $\xi > 3$ mm were discarded. This group contains events disturbed with noise but also events where large angle scattering occurred in the chamber.

Figure 5.27 shows the drift time-to-radius relation obtained in the iterative autocalibration procedure for all of the mixtures, for the exemplary given cell. Figure 5.28 presents the corresponding resolution $\sigma(r)$ and Fig. 5.29 presents the efficiency $\eta(r)$. The distribution of the fit quality parameter ξ is plotted in Fig. 5.30.

Table 5.3: Table showing the total number of events registered during each muon run with a division into accepted (green) and rejected (red) ones. In addition, the rejected subset was divided according to the cause of the rejection. P1 refers to the plane 1, a is the slope of the trajectory, ν is the degree of freedom of the fit, and ξ is the sum of squared residuals of the fit (see text for the description of each cut).

	mixture			
	0/100@300	50/50@300	50/50@600	70/30@600
accepted	40815	23226	49766	101008
no P1	224709	95813	98272	246115
$a \notin (-0.3, 0.3)$	8980	4517	9874	20497
$\nu < 4$	3966	10056	2580	6037
$\xi > 3$ mm	21404	10926	16608	37721
total	299874	144538	177100	411378

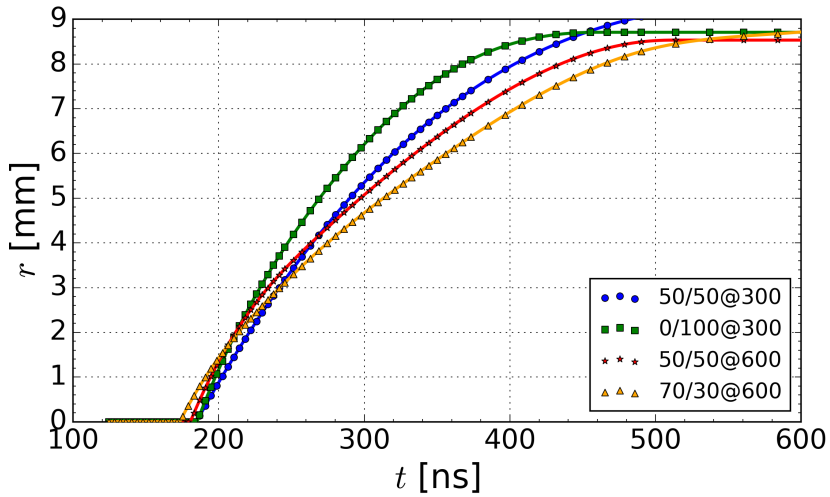


Figure 5.27: Drift time-to-radius relation $r(t)$ of the exemplary cell. The legend describes the measured mixtures.

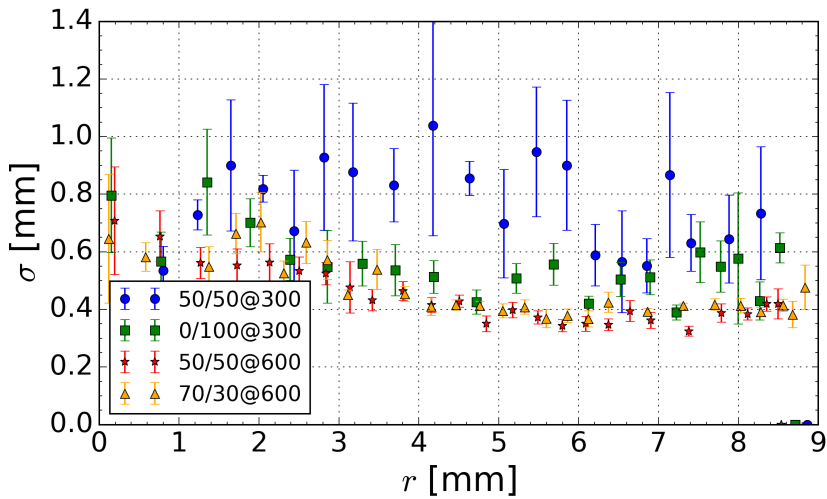


Figure 5.28: Spatial resolution $\sigma(r)$ of the exemplary cell. The legend describes the measured mixtures.

Mixtures of 50/50 and 70/30 at 600 mbar showed almost identical properties: $\sigma(r) \sim 0.6$ mm close to the center of the cell and 0.4 mm starting from $r = 4$ mm, although the ξ distribution indicates that fits are slightly better with the 70/30

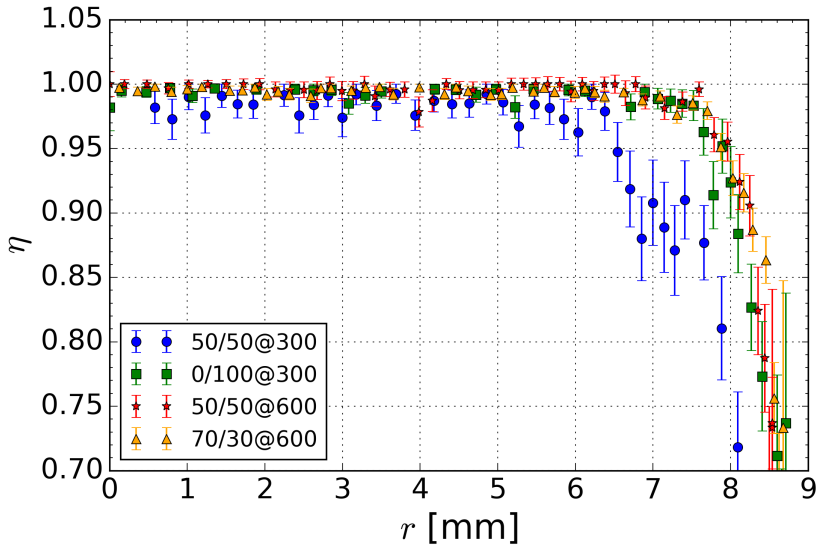


Figure 5.29: Efficiency η as a function of the distance r from the center of the exemplary cell. The legend describes the measured mixtures.

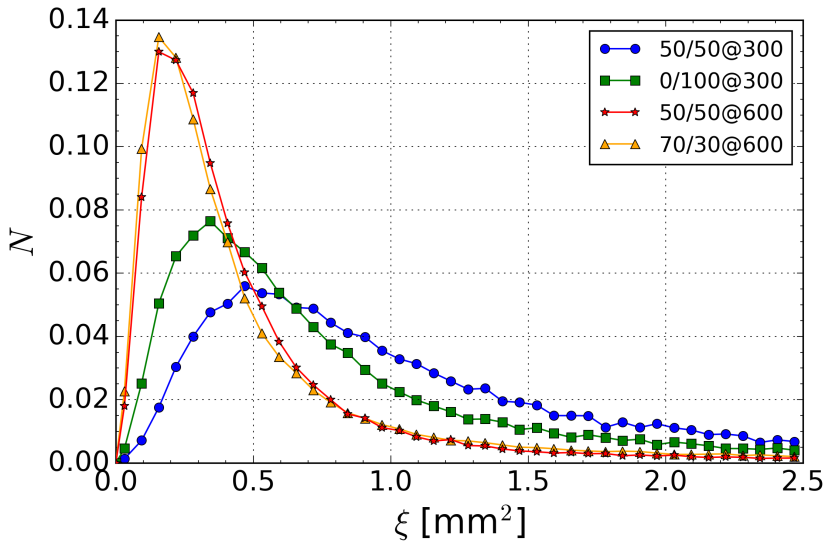


Figure 5.30: Normalized ($\Sigma N = 1$) distributions of fit quality ξ for muon xy -trajectories in the measured mixtures (described in the legend).

mixture. The efficiency $\eta(r) \sim 0.99$ for almost the entire cell and starts to drop down around $r = 7$ mm, which is the result of the low electric field at the cell periphery. The pure isobutane at 300 mbar has almost identical $\eta(r)$, however, its spatial resolution is roughly 0.15 mm worse everywhere in the cell, which is also visible in the ξ distribution.

The mixture of 50/50 at 300 mbar showed the worst performance. Its $\sigma(r)$ is almost twice worse than the one of 50/50 or 70/30 at 600 mbar. Additionally, $\eta(r)$ drops down earlier, already around 6 mm. It is believed that the reason behind the efficiency loss was a non-optimal HV setting. The lower number of primary ionization characterizing 50/50 at 300 mbar mixture has to be compensated by operating in a higher gas gain regime. The spectrum of heights of incoming signals was shifted towards lower values as compared to other mixtures (Fig. 5.31), hence part of the signals was not reaching the detection threshold. It was the last tested mixture and the HV system was already showing problems with delivering the appropriate voltage. The chamber was heavily exploited during the tests and failure of some electronic components, like HV capacitors responsible for the separation of signals from HV DC offsets, was observed. During the ongoing upgrade phase, all signal planes will be replaced with new ones, with an improved voltage stability protection.

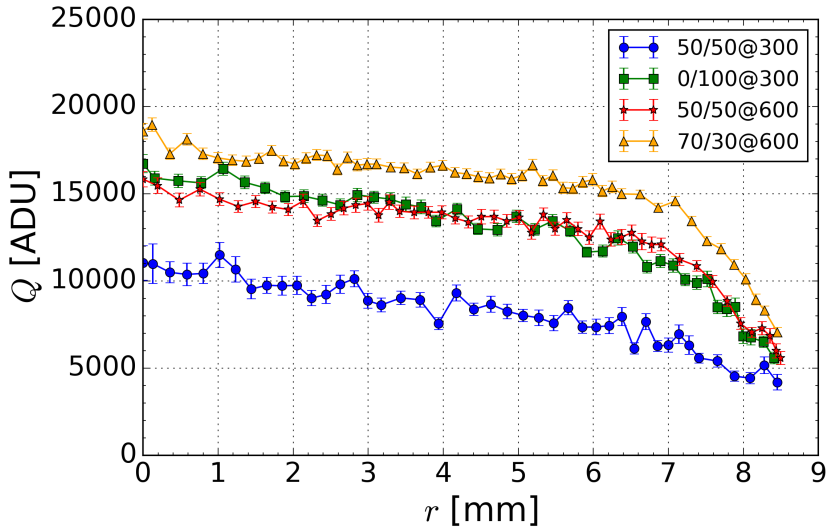


Figure 5.31: Mean value of the Q distribution as a function of r for the exemplary cell. Corresponding mixtures are labeled in the legend.

Chapter 6

Reconstruction of particle trajectory in the yz -projection

6.1 Overview

In order to obtain the full 3D trajectory the z -coordinates of the hits have to be extracted from the acquired information in addition to the previously determined x - and y -coordinates. In the miniBETA spectrometer, the collected charge is read out from both ends of the signal wire. The position along the wire, where the charge was created, is calculated using the charge division technique [34]. In the following sections an algorithm for finding the trajectory in the yz -projection is presented and the efficiency and resolution of the tracking are estimated, based on the measurements of cosmic muons (Sec. 5.2.3). Culprits of systematic uncertainties are also identified and methods of eliminating them are discussed.

6.2 Charge division technique

In the vicinity of the signal wire, in the gas gain region where the electric field is the highest, the number of drifting electrons is multiplied in an avalanche, producing a negative charge Q . According to the Shockley–Ramo theorem, an electron moving in the vicinity of an electrode induces an instantaneous electric current i :

$$i = E_v ev, \quad (6.1)$$

where e is the charge of the electron, v is its instantaneous velocity, and E_v is the component in the direction v of the electric field which would exist at the electron's instantaneous position under the following circumstances: electron removed, given electrode raised to unit potential, all other conductors grounded [83, 84]. The superposition principle guarantees that the total induced current I is proportional to the total charge Q :

$$I = \Sigma i \propto Q = \Sigma e. \quad (6.2)$$

During the avalanche, the same number of positive ions as electrons is created, however, the drift velocity of positive ions is about 1000 times lower than the drift velocity of electrons. Therefore, the influence of the ions on the induced current measured in the setup can be neglected when fast preamplifiers are used. The induced current splits and follows two paths $I = I_a + I_b$, towards both ends of the wire. The current I_i flowing in each path is inversely proportional to the path resistance R_i : $I_i \propto \frac{1}{R_i}$. The wire resistivity and diameter are considered constant. Therefore, the resistance is proportional to the path length: $R_i \propto l_i$. Preamplifiers at each end of the wire transform the currents linearly into differential voltage signals:

$$V_i = \pm f(I_i) = \pm(q_0 + q_1 I_i), \quad (6.3)$$

where q_0 and q_1 are parameters of the linear function depending on the preamplifier gain. Differential signaling was chosen as a method of voltage signal transmission to reduce noise introduced along this path. Signals are transmitted to the DAQ, where they are converted into digits by the 14-bit ADC module and stored in the hit data. Recorded values are called A_a and A_b and are expressed in analog-to-digital units (ADU). Figure 6.1 shows the idea of the charge division technique.

6.2.1 Determination of the offset of the amplitude readout

A detailed description of the ADC module and its operation is given in [34]. In the scope of this thesis it is sufficient to understand that the recorded value A corresponds to the measured signal height V through the following relation:

$$A = O - V, \quad (6.4)$$

where O is the level of the baseline (also called offset) of the DAQ channel responsible for reading out the signal V . The value $A = 0$ ADU corresponds to the end of the ADC range and overshooting signals. Measuring the signal in such a way requires knowledge of the offset O_i of every DAQ channel.

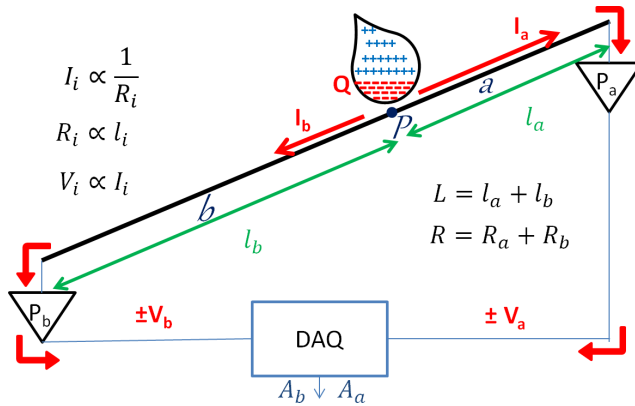


Figure 6.1: Schematic representation of the idea behind the charge division technique. The negative charge Q induces a current in the wire which splits into two paths, inversely proportional to the path length $I_{a(b)} \propto 1/l_{a(b)}$. At the end of each path a charge-voltage preamplifier $P_{a(b)}$ is mounted generating a differential signal $\pm V_{a(b)}$, which is transmitted to the DAQ and converted by the ADC module into a digital signal recorded on the PC.

The determination of offsets is based on the premise that if a hit is detected on a channel in the ADC module, the other channels, where the measured signals are smaller than the discrimination threshold, are measuring their baselines. Hence, for every event, readouts of channels which passed the discriminator threshold are saved as A values, and readouts of all the other channels are saved as O values.

A test with the acquisition electronics detached from the chamber was performed in order to measure the internal noise of the DAQ. A signal generator (Tabor PM8572) generated signals at 100 Hz in two channels in coincidence: TTL triggering the DAQ (instead of the PMT signal) and a pulse signal passing through the dedicated tester [34] which simulated a signal from a wire. The tester was connected to the DAQ in a way that only a single channel was receiving the signal. In this setup, readouts of other channels in the DAQ module show their offsets (Fig. 6.2 (left)). During measurements with an ionizing source, all of the DAQ channels are connected with the chamber, hence they experience additional noise generated by the preamplifiers causing bigger fluctuations in the baseline, therefore increasing the standard deviation of the recorded values (Fig. 6.2 (right)). Small deviation in the offsets' mean values is a result of differences in the setups. The internal noise of the module was measured for the channel without any load connected, whereas in the full setup the channel is connected to the drift chamber. The spikes on the line of the

internal noise are probably artefacts caused by events registered when the baseline was not properly prepared by the module [78]. The influence of the baseline noise on the z -position uncertainty is evaluated in Sec. 6.3.2.

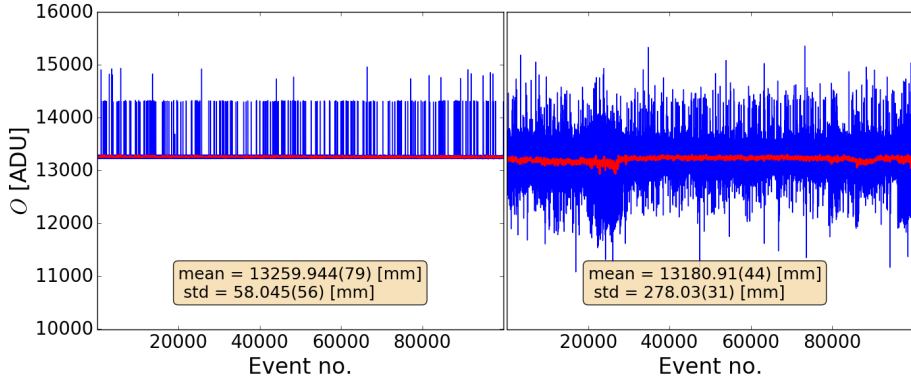


Figure 6.2: Subset of recorded offset values for an ADC channel when the triggering signals were created (left) by the signal generator and tester simulating a signal from a wire and (right) by the ionizing source (^{207}Bi). The red line represents the moving average with the size of the subset $N=100$.

In this thesis, an average value $\langle O_i \rangle$ was determined for each channel in the measurement and used in the V_i calculations. Nevertheless, the DAQ saves the offset readout for each event, which allows for more a sophisticated analysis, e.g. using a moving average, with optimized sampling size, which would eliminate possible drifts in the baseline during the measurement period. In the miniBETA drift chamber, there are no physical walls between cells and a moving charge can possibly be seen in cells adjacent to the one recording the hit, affecting their baseline readout. This effect can also be analyzed and, if needed, channels neighboring with the one that recorded the hit could be excluded from the offsets determination.

6.2.2 Principles of the z -coordinate extraction

The coordinate z_p of a point P , dividing a wire of length L into two segments a and b of lengths l_a and l_b (Fig. 6.1), can be described as:

$$z_P = \frac{L}{2} \cdot \frac{l_a - l_b}{l_a + l_b}. \quad (6.5)$$

This coordinate system is aligned with the wire and its center is located at the center of the wire. Using relations between l_i , R_i , I_i , V_i and applying:

$$f^{-1}(V_i) = I_i = p_{i,0} + p_{i,1}V_i, \quad (6.6)$$

being the inverse relation to (6.3), where $p_{i,0}$ and $p_{i,1}$ are parameters depending on the preamplifier gain, Eq. (6.5) can be transformed as follows:

$$\begin{aligned} z_P &= \frac{L}{2} \cdot \frac{R_a - R_b}{R_a + R_b} = \frac{L}{2} \cdot \frac{\frac{1}{I_a} - \frac{1}{I_b}}{\frac{1}{I_a} + \frac{1}{I_b}} = \frac{L}{2} \cdot \frac{I_b - I_a}{I_b + I_a} \\ &= \frac{L}{2} \cdot \frac{f^{-1}(V_b) - f^{-1}(V_a)}{f^{-1}(V_b) + f^{-1}(V_a)}. \end{aligned} \quad (6.7)$$

In principle, each preamplifier can have a slightly different gain. This could cause systematic shifts in z , if not corrected accordingly.

6.2.3 Experimental method for correcting the gain balance for preamplifiers

The method described in this section increases the accuracy of the charge division technique. This is achieved by experimentally determining corrections which balance the gains of all preamplifier pairs used in the chamber, simultaneously. The reasoning behind the method is provided in the following text.

If a charge is generated in the center of a wire (emphasized by an indicator 0) the current measured at both ends should be the same. This can be written as:

$$I_a^0 = I_b^0 \equiv f^{-1}(V_a^0) = f^{-1}(V_b^0) \equiv p_{a,0} + p_{a,1}V_a^0 = p_{b,0} + p_{b,1}V_b^0, \quad (6.8)$$

where V_a^0 and V_b^0 are the measured signal heights and $p_{i,j}$ are the parameters of the preamplifier gains. One can reduce the number of parameters by defining:

$$\begin{aligned} p'_0 &= \frac{p_{a,0} - p_{b,0}}{p_{b,1}}, \\ p'_1 &= \frac{p_{a,1}}{p_{b,1}}. \end{aligned} \quad (6.9)$$

Using this notation, one can rewrite Eq. (6.8):

$$V_b^0 = p'_0 + p'_1 V_a^0. \quad (6.10)$$

If the charge was divided into two branches equally, the voltages recorded at the wire ends are equal only if $p'_0 = 0$ and $p'_1 = 1$, i.e. if the preamplifiers have

the same gain. Other values of p'_j will cause an artificial asymmetry. In order to compare the measured voltages, one has to find the parameters p'_0 and p'_1 that transform V_a^0 into $V_{a,corr}^0$:

$$V_{a,corr}^0 := p'_0 + p'_1 V_a^0, \quad (6.11)$$

such that:

$$V_{a,corr}^0 = V_b^0. \quad (6.12)$$

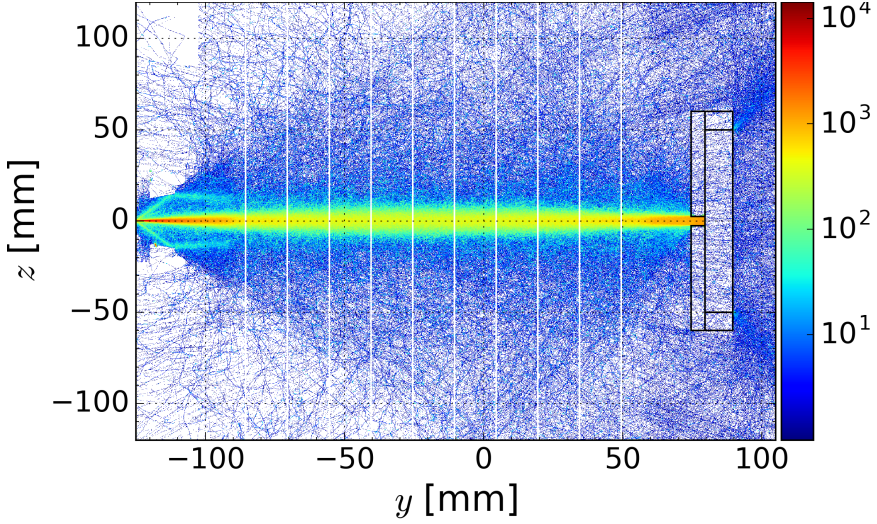


Figure 6.3: Two-dimensional histogram (log scale) of simulated electron trajectories from a 1 MeV monoenergetic source at $z = 0$ mm, $y = -125$ mm detected by the scintillator covered by the mask with the slit in the center (black contour) [55]. The miniBETA geometry was used and the chamber was filled with the 50/50 He-Iso mixture at 600 mbar. White vertical lines visualize the positions of the signal wires.

To approximate the condition for equal currents in both branches, a mask with a slit was mounted on the surface of the scintillator. It worked as an analyzer in measurements with a ^{207}Bi source, filtering out electrons that did not pass close to $z = 0$ mm (Fig. 6.3). The mask was made of two rectangular layers of plastic (2 and 3 mm wide) with a layer of brass (1 mm) in between and it was mounted to the plastic support surrounding the scintillator. The slit was cut through the center of the mask and had a width $d = 5$ mm (Fig. 6.4). The slit dimension was chosen so that it allows for a reasonable detection rate of particles in the chamber (~ 10 cps). The slit spanned at $z = 0$ mm and the source was positioned in front of it.

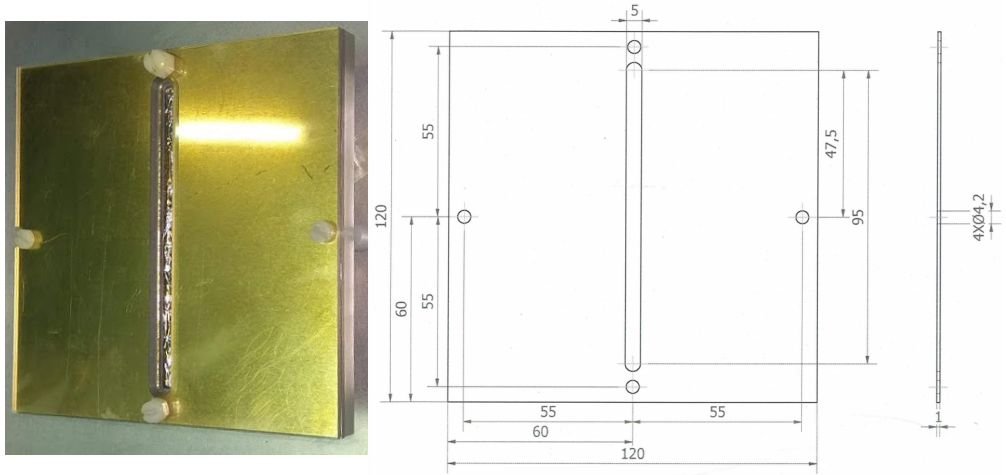


Figure 6.4: (Left) Picture of the scintillator covered with the mask used for preamplifier gain correction measurements. (Right) Technical drawing of the brass plate being part of the mask.

Figure 6.5 presents measured distributions of values V_a and V_b for a given channel. Figure 6.6 (left) presents a 2D histogram of recorded pairs (V_a, V_b) for a given pair of preamplifiers in the measurement. If both preamplifiers had the same gain the distribution would be symmetric along the line $V_a = V_b$. Fitting a straight line $V_b = p'_0 + p'_1 V_a$ provides parameters p'_0 and p'_1 necessary for the gain correction for the given pair of preamplifiers. The line was fitted with the orthogonal distances regression (ODR) procedure, which minimizes residuals along both axes. Signals from the wire P3W4 were chosen to illustrate the gain correction, because it has one of the biggest slopes $p'_1 = 1.1042(22)$.

Measurements were performed for 3 source positions along the slit: in front of the wire 3, 5 and 7 and combined together to maximize the number of illuminated wires.

The average gain correction $\langle p'_1 \rangle = 1.020(8)$ and the standard deviation of its distribution $\sigma(p'_1) = 0.07(1)$. Variation in preamplifier gains is nothing unusual knowing the limited accuracy of electronic components. However, it indicates the need for the gain calibration procedure.

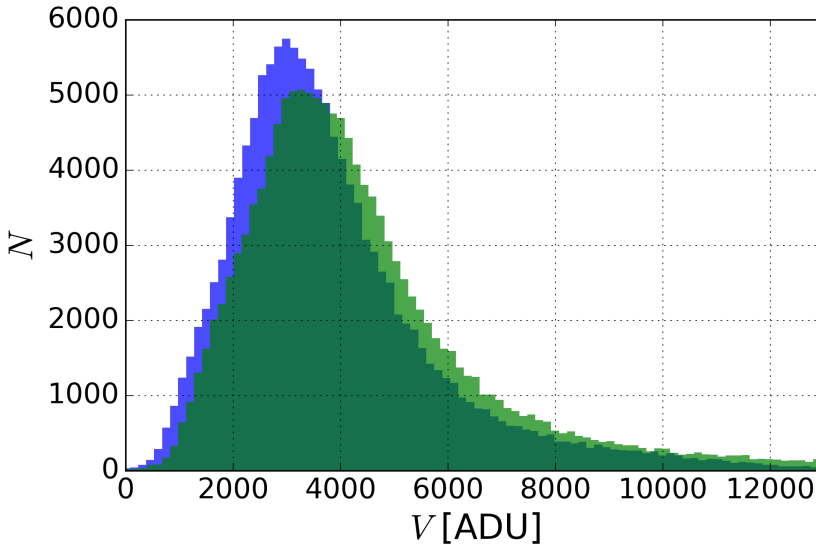


Figure 6.5: Example of measured V_a (blue) and V_b (green) distributions for the 3rd wire at the 4th plane, obtained from the gain correction dedicated measurement. Distributions should be identical if the preamplifiers gains were equal.

The explicit equation for determining the z_i position for a given wire i , parameterized by experimentally measured variables, is given by:

$$\begin{aligned}
 z_i &= \frac{L}{2} \cdot \frac{V_{i,b} - V_{i,corr,a}}{V_{i,b} + V_{i,corr,a}} = \\
 &= \frac{L}{2} \cdot \frac{(\langle O_{i,b} \rangle - A_{i,b}) - (p'_{i,0} + p'_{i,1} (\langle O_{i,a} \rangle - A_{i,a}))}{(\langle O_{i,b} \rangle - A_{i,b}) + (p'_{i,0} + p'_{i,1} (\langle O_{i,a} \rangle - A_{i,a}))}.
 \end{aligned} \tag{6.13}$$

Figure 6.7 shows the distribution of calculated z values for the wire P3W4 before (blue) and after (green) the gain ratio correction. The calculated gain corrections are then automatically applied for all further measurements. This procedure has to be repeated every time preamplifiers are replaced in the system.

6.3 Particle tracking in the yz -projection

For every trajectory, a subset of cells participating in its determination is established (based on xy -fit as described in Sec. 5.2.1). The position z_i , where

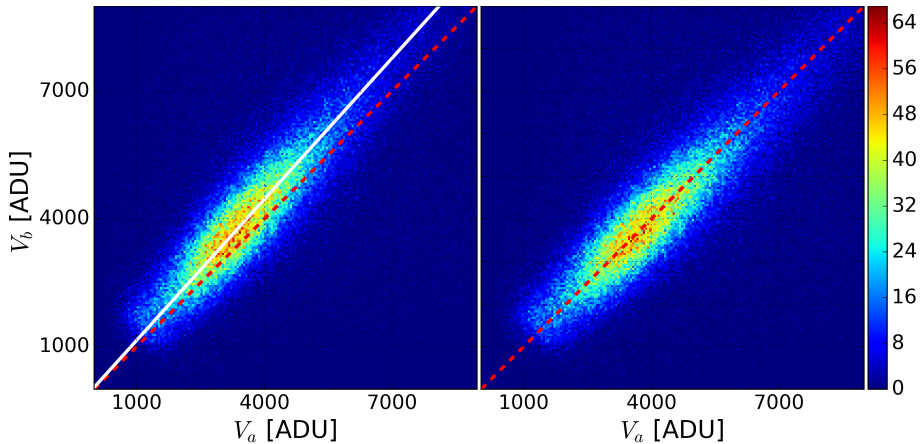


Figure 6.6: (Left) Histogrammed distribution of (V_a, V_b) pairs for the 3rd wire at the 4th plane from the measurement with the slit along $z = 0$ mm. The red dashed line visualizes the $V_a = V_b$ relation. The solid white line is a result of the ODR fit. (Right) Modified distribution after applying the gain correction.

the detected charge was created, is calculated according to Eq. (6.13) for each of the selected cells. The coordinate y_i of the hit is set to be equal to the coordinate $y_{L,i}$ of the point $P_{L,i}$ lying on the fitted XY trajectory projection line (Eq. (5.6)). Hits with at least one overshooting channel ($A_i = 0$ ADU) are filtered out, as well as the ones with too low signal ($A_i > 13000$ ADU).

If an event contains at least 4 hits a straight line:

$$z = cy + d, \quad (6.14)$$

passing the closest to the points (y_i, z_i) is found with the least-squares technique. The average value of the squared residuals $\langle \Delta^2 z_i \rangle$ is calculated. If any hit results in giving $\Delta^2 z_i > 5 \cdot \langle \Delta^2 z_i \rangle$ this hit is treated as an outlier and discarded. The trajectory is refitted with remaining hits. Figure 6.8 shows an example of a fitted muon trajectory in the yz -projection.

Residuals of muon trajectories in the yz -projection were used for correcting Eq. (6.13) for systematic uncertainties resulting from effects not included in the fit and to search for dependencies on other hit parameters, i.e. the sum of measured signals $Q_i = V_{i, \text{coord}, a} + V_{i, b}$ (the same letter was used as for the detected charge to stress the proportionality between these variables) and the fitted trajectory slope c .

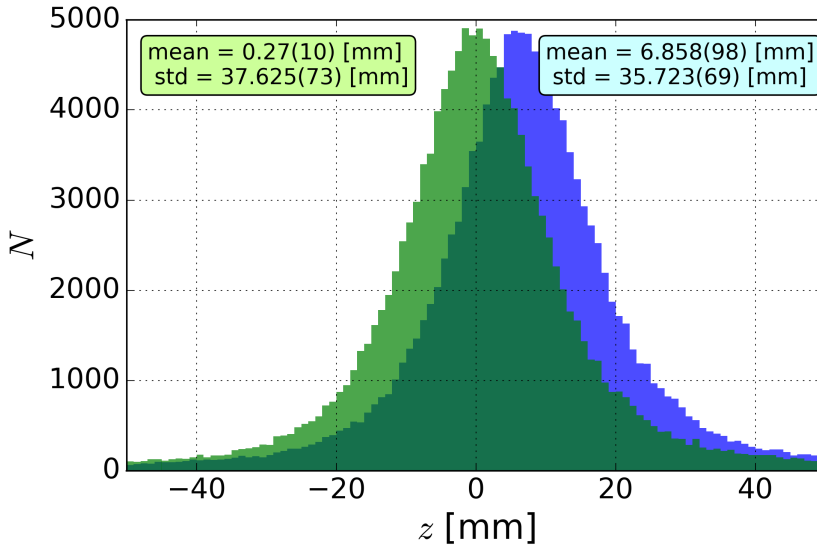


Figure 6.7: Distributions of calculated z -positions for the 3rd wire at the 4th plane from the measurement with the slit at $z = 0$ mm before (blue) and after (green) the gain ratio correction. One can see that the deviation from zero of the distribution's mean value was canceled after the correction (see the distribution's blue and green tables).

6.3.1 Determination of experimental corrections for the z -coordinate

Equation (6.13) assumes that the z -position is linearly dependent on the asymmetry α :

$$\alpha_i := \frac{V_{i,b} - V_{i,corr,a}}{V_{i,b} + V_{i,corr,a}}. \quad (6.15)$$

This picture is oversimplified, especially for positions further away from the center of the wire. In the evaluation of the equation, it was assumed that there are no other resistances beside the one of the wire. Having better resolution in mind one should not neglect the influence of preamplifiers input resistances and other electronic components not included in the simplified picture. These additional resistances will be seen as if the effective length of the wire was greater than the actual one and full asymmetry ($\alpha = \pm 1$) will never be measured, even for charges created at the edge of the wire.

A procedure similar to the one used for improving the $r(t)$ calibration can be applied in order to correct the function $z(\alpha)$. For each muon trajectory in the

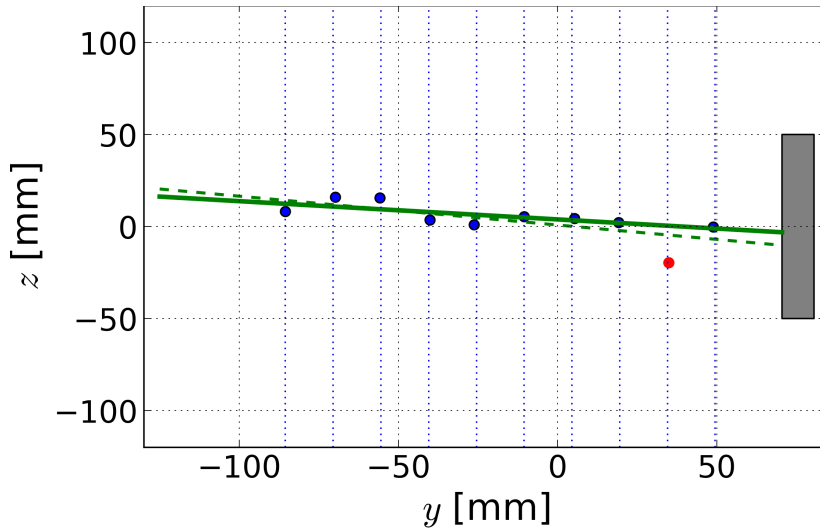


Figure 6.8: Example of a fitted muon trajectory (green line) in the yz -projection. Vertical dotted blue lines represent the positions of signal wires. The gray rectangle on the right represents the scintillator. The dashed green line corresponds to the initial fit including all of the hits (dots). The hit which was treated as an outlier is colored in red. The solid green line corresponds to the fit without outliers.

yz -projection the residuals Δz are calculated:

$$\Delta z_i = z_{i,meas} - z_{i,fit}, \quad (6.16)$$

where $z_{i,meas}$ is calculated based on Eq. (6.13) and $z_{i,fit}$ corresponds to y_i on the fitted line. The fit quality is defined in the same way as for the xy -fit by ξ (Eq. 5.13). Only tracks resulting in $\xi < 500 \text{ mm}^2$ were selected for this procedure. Figure 6.9 shows an example of a 2D histogram of $(\alpha, \Delta z)$ pairs for the exemplary cell (plane 9 wire 5).

Distributions of $(\alpha_i, \Delta z_i)$ were divided along α into 40 subsets of equal length, marked by a center value α_c in a given subset. Next, the mean value $\langle \Delta z_i \rangle$ was found for each subset. A spline function was fitted to the obtained $(\alpha_c, \langle \Delta z_i \rangle)$ points to find the relation between Δz_i and α (Fig. 6.9).

However, it was found, that the detection geometry, confined by the scintillator acceptance cone, affects significantly the distribution of residuals. This problem will be discussed in the next paragraph. To limit this influence, only a sub-range corresponding to $z \in (-50, 50) \text{ mm}$ was chosen, and a straight line $P^1(\alpha)$ was

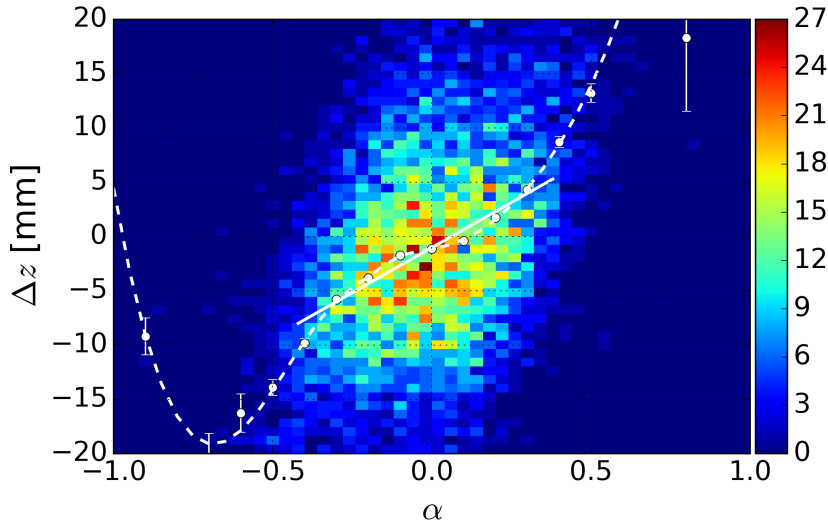


Figure 6.9: Example of a 2D histogram of measured asymmetries α and related residuals Δz of yz -fits. White points represent mean values of Δz around a given α . The solid straight line is the linear fit for a range corresponding to $z \in (-50, 50)$ mm and the dashed line is the fitted spline for the whole range.

fitted. This gives the first order correction for $z(\alpha)$:

$$z'_i = \frac{L}{2} \cdot \alpha_i - P_i^1(\alpha_i), \quad (6.17)$$

Figure 6.10 shows the fitted splines for $(z, \Delta z)$ pairs for wire 5 on each signal plane, before and after the first-order correction. One can see that the spline arms bend in the same direction for every plane and the distance between the arms is systematically getting smaller with the plane number, hence with decreasing width of the scintillator acceptance cone. After the first order correction splines have more similar shapes and are shifted so that all of them pass near $z(\Delta z = 0\text{mm}) = 0$ mm (the largest shift being visible for planes 4 and 9).

Moreover, applying the iterative correction procedure with this geometry resulted in a falsely positive improvement of the fit quality, since all the residuals from regions outside of the scintillator acceptance cone are pulled into its borders by this procedure. Therefore, only the first-order correction was applied for the current version of the scintillator. This problem will be reevaluated after the exchange of the scintillator for a bigger one.

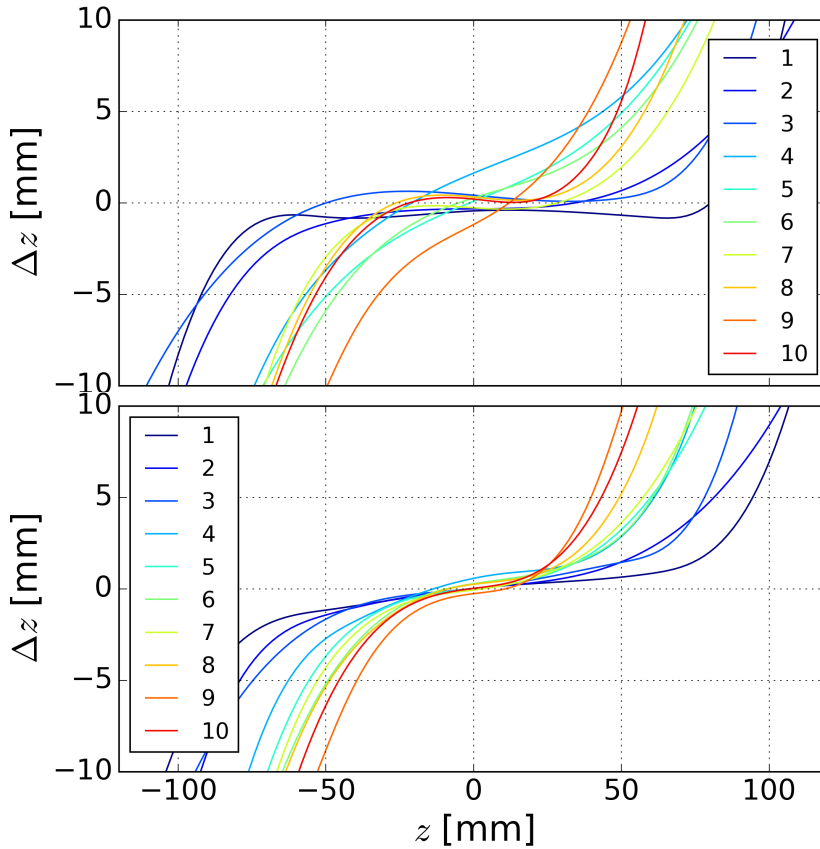


Figure 6.10: Fitted spline functions for $(z, \Delta z)$ pairs for wire 5 at every plane (top) before and (bottom) after the first order correction. The plane number and the corresponding color are given in the legend.

6.3.2 Resolution of the hit positioning in the z -direction

It was observed that Q of recorded hits, hence the total charge created on a wire, has a major effect on the distributions of fit residuals Δz . Figure 6.11 presents an example of a 2D histogram of $(Q, \Delta z)$ pairs after the first order correction was applied for the exemplary cell. The behavior is as expected because the higher Q the better signal-to-noise ratio, hence the resolution.

For each cell i , the distribution of $(Q, \Delta z)_i$ was divided along Q into 28 subsets of equal length, marked by the central value Q_c in a given subset. The standard deviation $\sigma(\Delta z)$ was calculated for each subset and an exponential function

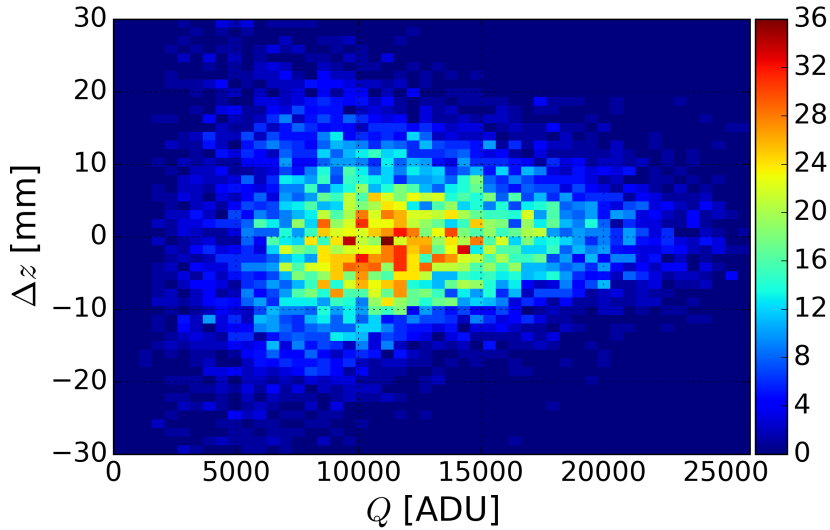


Figure 6.11: Two-dimensional histogram of $(Q, \Delta z)$ pairs for the exemplary cell obtained from fitting muon trajectories.

was fitted to the obtained points $(\sigma(\Delta z), Q_c)_i$ (Fig. 6.12):

$$\sigma_i(\Delta z) = A_i + B_i \exp(\kappa_i Q), \quad (6.18)$$

where A_i , B_i and κ_i are fit parameters. These relations were considered to be the hit positioning resolution in the z -dimension. It was observed that the resolution of individual channels can vary significantly even between neighboring wires on the same plane, therefore it is expected that this is an effect related to the detector electronics.

Additionally, the influence of the preamplifier noise is shown on the resolution plot as a dashed line. It was assumed that the noise affecting the signal height is given by the standard deviation of the corresponding baseline fluctuations (Sec. 6.2). The uncertainty of the z -coordinate was calculated for a range of Q values assuming that the signal height was equal in both branches. Calculations proved that the difference between channels originates from the preamplifier noise and that this noise influences the resolution in a major way.

It was also tested whether the slope c (Eq. (6.14)) of the fitted muon trajectory affects the distribution of the fit residuals (Fig. 6.13) and no effect was found (Pearson correlation coefficient $r \in (-0.15, 0.15)$). It means that within the detector accuracy one can neglect the influence of the trajectory slope c on the z -tracking performance i.e. no additional correction for $z(c)$ is needed.

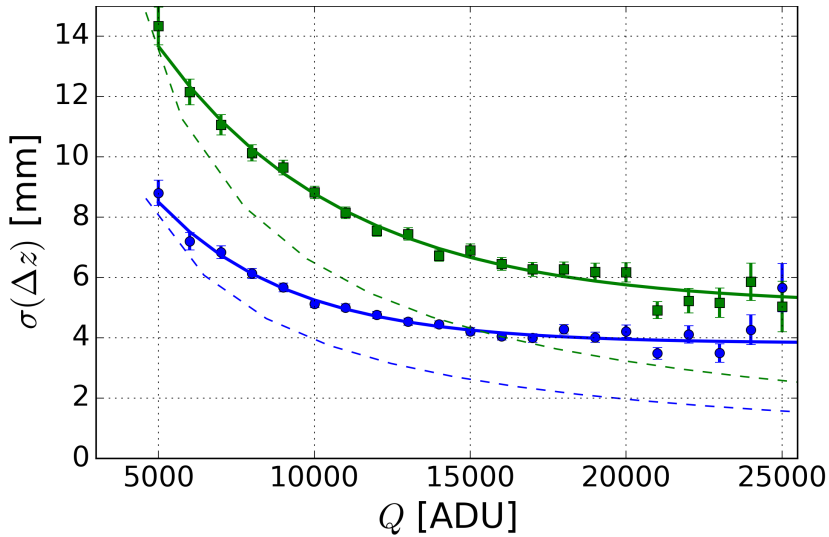


Figure 6.12: Example of the correlation between the standard deviation of yz -fit residuals $\sigma(\Delta z)$ and the sum of recorded signals Q for neighboring cells, related to plane 9 wire 4 (blue dots) and wire 5 (green squares). Solid lines represent fitted exponential functions (Eq. 6.18), which define the cell resolution. Dashed lines visualize the influence of the base line fluctuations).

A similar conclusion was drawn about an effect of the trajectory distance d from the signal wire on the resolution of the z -position (Fig. 6.14). Within achieved accuracy, an effect of electron cloud diffusion along the z -axis during the drift towards the signal wire is not visible. The standard deviation of the residual distribution is getting bigger closer to the cell edges, however this is an effect of decreasing Q in that region Sec. (5.3.5).

6.3.3 Efficiency of the tracking in the yz -projection

The efficiency of the tracking in the yz -projection was defined in a similar way as in the xy -projection. Only the total cell efficiency $\bar{\eta}^z$ was calculated, since the scintillator geometry limits the detected trajectories to the ones in the middle part of the wires. The detection efficiency of a cell i was defined as:

$$\bar{\eta}_i^z = \frac{N_{i,fired}^z}{N_{i,total}}, \quad (6.19)$$

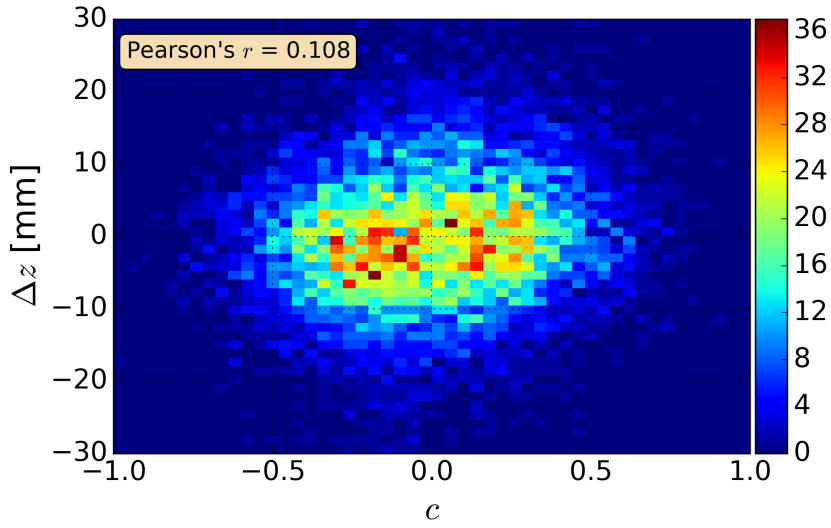


Figure 6.13: Two-dimensional histogram of $(c, \Delta z)$ pairs, where c is the slope of the fitted trajectory and Δz is the yz -fit residual, for the exemplary cell.

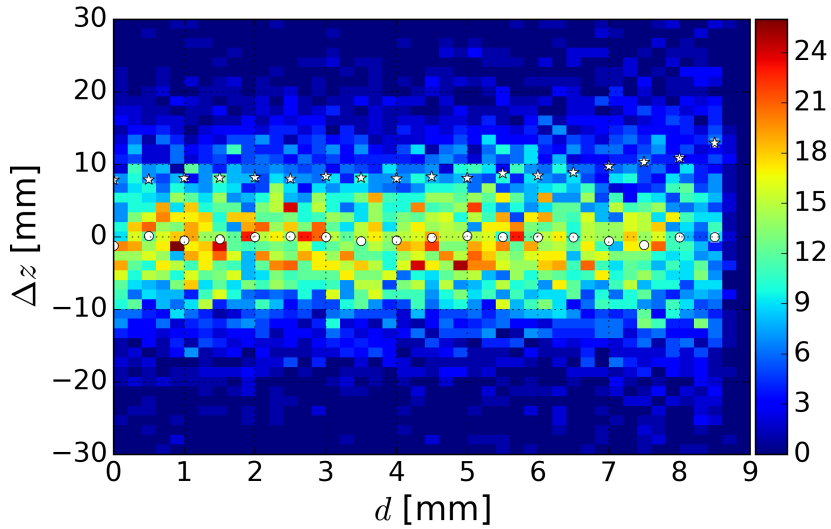


Figure 6.14: Two-dimensional histogram of $(d, \Delta z)$ pairs, where d is the distance from the wire and Δz is the yz -fit residual, for the exemplary cell. White dots represent mean values of slices along d and white stars their standard deviations.

Table 6.1: Total cell efficiency for muon tracking in the yz -projection. It was found after measurements that cells defined by plane 4 wire 8 and plane 9 wire 8 had one of their preamplifiers broken, hence their efficiency is 0.

		wire							
		1	2	2	4	5	6	7	8
plane	1	0.27	0.7	0.78	0.8	0.78	0.76	0.78	0.73
	2	0.76	0.86	0.83	0.8	0.81	0.89	0.83	0.85
	3	0.29	0.85	0.88	0.89	0.88	0.9	0.76	0.89
	4	0.51	0.75	0.77	0.82	0.8	0.83	0.83	0
	5	0.43	0.81	0.84	0.87	0.82	0.69	0.78	0.83
	6	0.72	0.82	0.84	0.81	0.86	0.87	0.9	0.75
	7	0.25	0.8	0.71	0.86	0.86	0.85	0.86	0.87
	8	0.73	0.83	0.82	0.82	0.87	0.86	0.88	0.74
	9	0.1	0.77	0.85	0.85	0.83	0.82	0.74	0
	10	0.39	0.82	0.84	0.86	0.85	0.89	0.89	0.66

where $N_{i,fired}^z$ is the number of times the cell contributed to the muon trajectory yz -fit and $N_{i,total}$ is the number of times the muon trajectory passed through the cell. Table 6.1 presents results for the muon measurements.

The efficiency of tracking in the yz -projection is lower than the one in the xy -projection, which is mainly related to the limited ADC conversion range. Measured signals V have to be high enough to provide a reliable readout but if the signal from any side of the wire overshoots, calculation of the asymmetry cannot be performed. A dynamic range of the ADC was chosen in a way providing the optimal resolution for the majority of signals. However, it required compromising the ability to properly measure signal heights from the tail of the height distribution (Sec. 4.5). Table 6.2 presents the ratio of times when any of the cell channels overshoot and the total number of trajectories going through the cell. Further modifications of the ADC modules might be needed to optimize the detection range, if high efficiency is required.

Table 6.2: Proportion of hits that were excluded from trajectories fitting due to the ADC module overshooting.

		wire							
		1	2	2	4	5	6	7	8
plane	1	0.73	0.29	0.21	0.19	0.21	0.23	0.22	0.27
	2	0.22	0.06	0.13	0.16	0.16	0.06	0.07	0.09
	3	0.7	0.11	0.08	0.07	0.08	0.07	0.2	0.09
	4	0.46	0.17	0.13	0.13	0.13	0.12	0.14	0.07
	5	0.55	0.15	0.11	0.1	0.11	0.12	0.14	0.08
	6	0.2	0.13	0.08	0.08	0.08	0.07	0.07	0.05
	7	0.69	0.14	0.12	0.1	0.1	0.11	0.1	0.09
	8	0.19	0.14	0.15	0.14	0.1	0.1	0.1	0.11
	9	0.9	0.14	0.12	0.12	0.12	0.12	0.13	0.2
	10	0.53	0.16	0.14	0.12	0.13	0.07	0.08	0.16

6.4 Summary

The determination of the z -coordinate, according to the charge division technique, was implemented successfully. The tracking of cosmic muons, in the direction along the signal wire, by the miniBETA detector, has been commissioned. The identified major sources of systematic uncertainty are:

- Knowledge of baselines (offsets) is crucial for the correct calculation of the signal height. More efficient algorithms of extracting offsets from recorded data are considered.
- Due to the spread in gains of the charge-to-voltage preamplifiers mounted at each end of the signal wires, the appropriate correction is needed. The experimental procedure of determining this correction for each pair of preamplifiers was successfully developed and tested.
- The total collected charge Q shows the greatest influence on the z -coordinate resolution and this dependency was included in the weighted fit, individually for each cell.
- The resolution varies significantly between cells. It was shown that this effect has its source in the preamplifier noise and properties of the DAQ.

As a result, the preamplifier design was upgraded: an additional electromagnetic shielding was implemented and some minor changes in electronic components were introduced, which should improve their overall performance and consistency [78].

The influence of other parameters, i.e. the trajectory slope c and the distance from the signal wire d were found to be negligible within the achieved resolution. The limited scintillator acceptance cone introduces a correlation of the residuals with the chamber geometry, which hinders the extraction of reliable corrections. Only the first-order correction for $z(\alpha)$ was introduced. The need for corrections of a higher order, resolving possible nonlinearities, will be evaluated after the exchange of the scintillator.

The preamplifiers were exchanged in between runs with different gas mixtures, hence the dependency of individual cell resolution on the gas mixture cannot be compared. However, the distribution of the fit quality ξ for muon trajectories can be used as an indicator of the general mixture performance. Because the trajectories span the entire chamber, the general trend becomes visible. Figure 6.15 presents histograms of ξ obtained for the tested mixtures, normalized with the total number of counts. According to this, the 70/30 at 600 mbar mixture gives the best fit quality, 50/50 at the same pressure is slightly worse, followed by 0/100 at 300, while 50/50 at 300 is the worst.

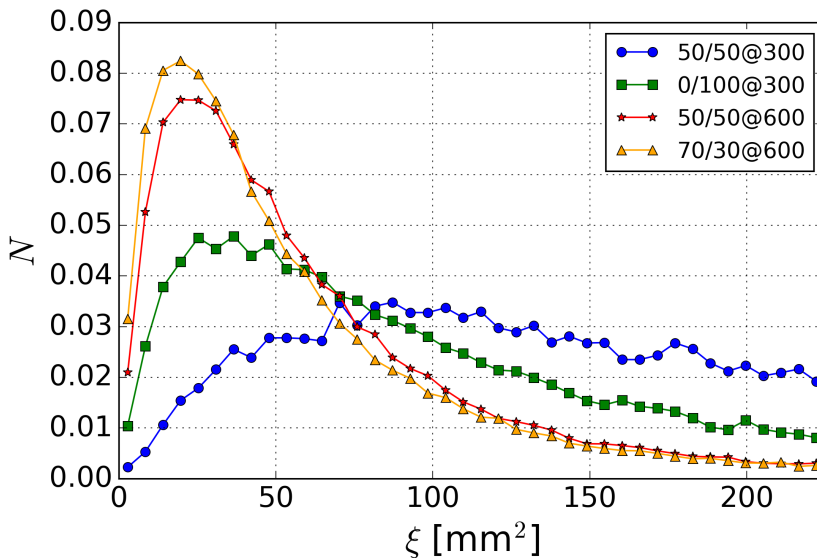


Figure 6.15: Normalized ($\Sigma N = 1$) histograms of fit quality ξ for muon trajectories in the yz -projection, for tested gas mixtures (label in the legend).

The efficiency of determining a valid position from the charge division method was estimated to be around 0.75-0.85 for most of the cells and tested gas mixtures. Tables with cells efficiencies for all the mixtures can be found in Appx. A. The major limitation comes from the optimization of the dynamic range of

the ADC. Overshooting signals, from the tail of the signal height distribution, cannot be used in the calculations (Sec. 4.5).

To solve the above problems, related with signal height measurements, a different approach for determining the charge collected on a wire is being considered, based on a method called time-over-threshold (ToT) [78, 85]. In the ToT, the charge is determined from the width of a signal, instead of its height. This converts measurements of the signal amplitude, handled by the ADC, to measurements of the time the signal stayed above a given threshold, handled by the TDC.

6.5 3D tracking

The ability to trace an ionizing particle in three dimensions is beneficial for the precision beta spectrum shape measurements planned for the miniBETA spectrometer, as it allows for better handling of the (back)scattering. Moreover, as will be presented in Sec. 7.3, the efficiency of light collection by a PMT (hence the energy resolution) depends on the position where a beta particle hits the scintillator. This dependency was particularly strong in the used scintillator, as its primary role was to trigger the DAQ and the shape was not yet optimized for a spectroscopic measurement.

The final straight 3D trajectory L is given by a set of equations:

$$\begin{cases} x = ay + b, \\ z = cy + d, \end{cases} \quad (6.20)$$

where the parameters a, b result from the fit based on the drift time-to-radius relation and c, d from the fit based on the charge division. Uncertainties of point $P(x, y, z) \in L$ coordinates are calculated individually with the standard uncertainty propagation from covariance matrices of the fit parameters. The uncertainty of x - and y -coordinates is typically an order of magnitude smaller than the uncertainty of the z -coordinate.

Figures 6.16 and 6.17 present distributions of uncertainties of the extrapolated positions, at the scintillator surface, from xy - and yz - fits, accordingly. Resolutions of these extrapolations are slightly better than single cell resolutions in the corresponding mixture.

Figure 6.18 presents a 2D histogram of hit positions on the scintillator surface extrapolated from the fitted muon trajectories, for the chamber filled with 50/50 helium-isobutane mixture at 600 mbar. The square shape of the scintillator is reproduced, which is a signature of the successful tracking technique. Edges in the x -dimension are sharper than the ones in the z -dimension due to different resolutions in these directions.

An inhomogeneity of counts can be seen along the x -axis. This inhomogeneity is especially visible in the measurement with the ^{207}Bi source (Fig. 6.19), where an interference-like pattern is visible on the scintillator surface. This is a combined effect of cell efficiencies dropping at cell edges, poor quality of the scintillator used in the commissioning phase, and a possible systematic error introduced due to the extrapolation of the drift time-to-radius relation near the signal wires (at $r < 1.5$ mm). The visible structure was changing with the source position and is related to the periodic structure of the drift chamber.

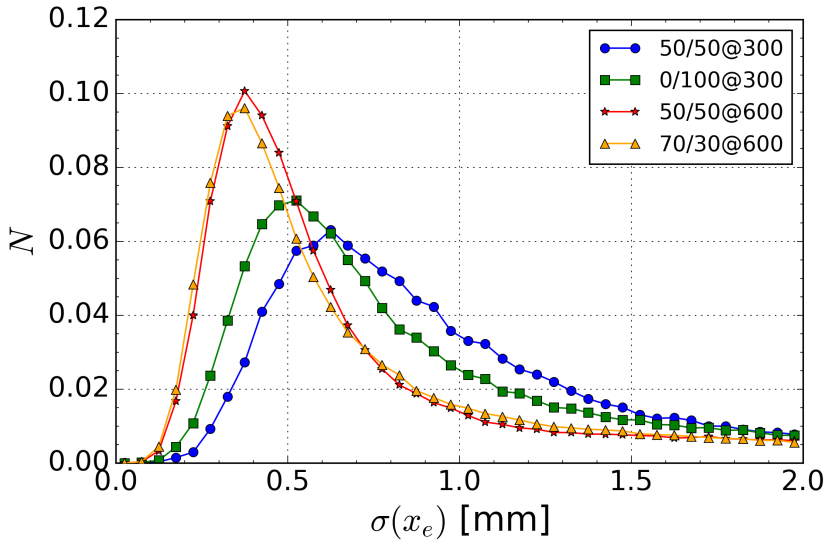


Figure 6.16: Distributions of uncertainties of the x -coordinate extrapolated to the scintillator surface.

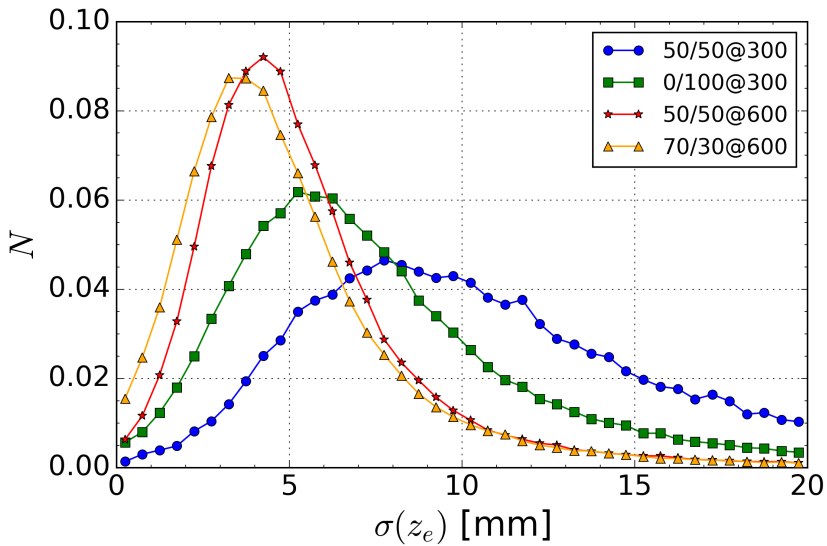


Figure 6.17: The same as Fig. 6.16 but for the z -coordinate.

When the source position is fixed, the hit position on the scintillator corresponds to a certain path a particle might have passed. This causes an effect resembling

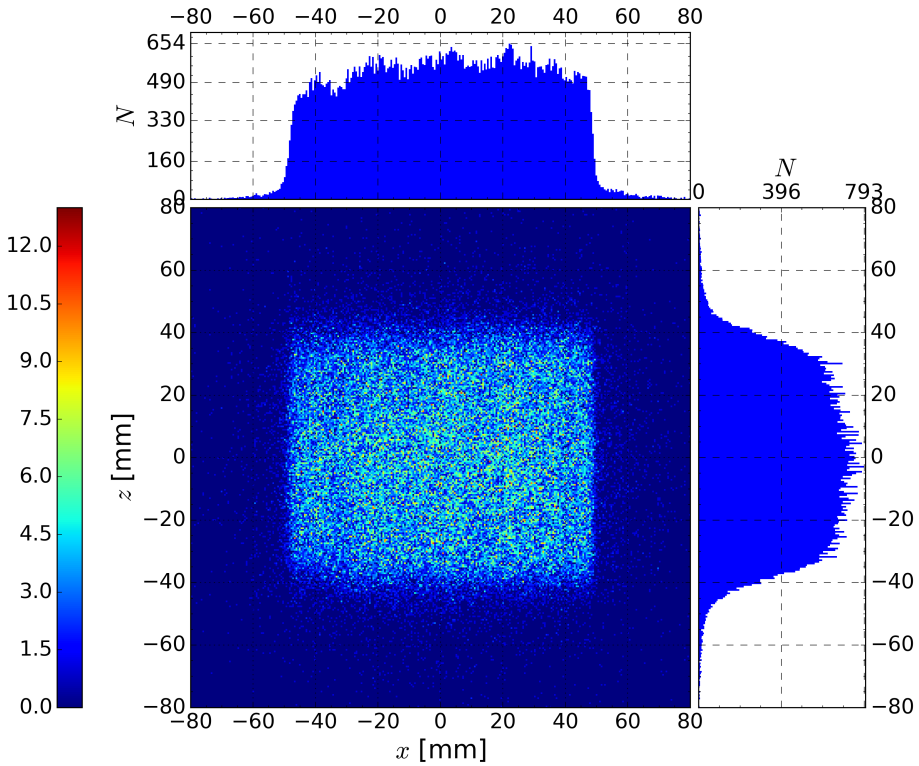


Figure 6.18: Two-dimensional histogram of extrapolated points where fitted muon trajectories crossed the plane where the scintillator surface is located, with casts at x and y axis.

the channeling/blocking effect, known from the physics of monocrystals. The drop of the detection efficiency decreases the probability of registering a trajectory passing through a region of $r = R_{max}$ (blocking). In addition, a systematic shift in the drift time-to-radius relation, close to $r = 0$ mm, can pull/push the trajectory towards/from the cell center (channeling).

Figure 6.20 shows a 2D histogram of calculated (x_l, y_l) pairs, visualizing all the positions where the ^{207}Bi trajectories were detected, with casts at the x - and y -axes. Drops in the counts along the x -axis are greater than for muons (Fig. 5.25). Trajectories from the ^{207}Bi source systematically pass through multiple regions with lower efficiency. Whereas trajectories of muons, coming from different directions, suppressed the influence of the periodic structure.

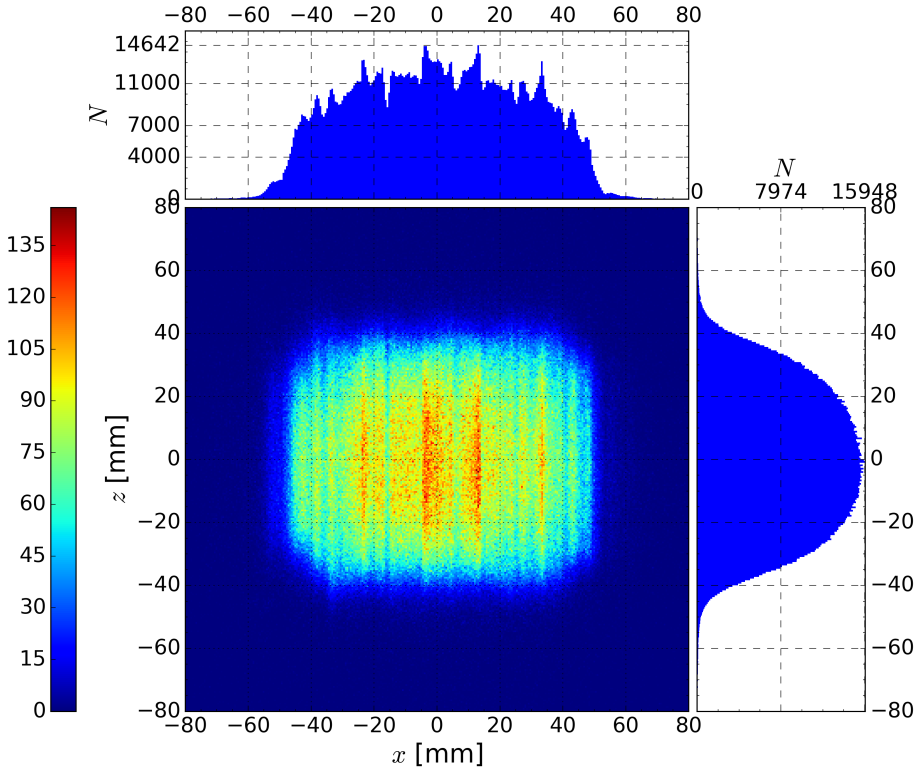


Figure 6.19: As Fig. 6.18, but for the ^{207}Bi source.

Figure 6.21 combines the distribution of trajectories' x -coordinates extrapolated on the scintillator with the scheme of the chamber geometry. Straight lines were added connecting the source with the locations where the biggest differences in counts are located, which helps in understanding the above problem.

The current version of the analysis software allows to select subgroups of the fitted trajectories according to any combination of the following conditions, individually for xy - and yz -fits:

- number of planes participating in the event reconstruction;
- fit quality ξ (based on the sum of squared residuals of the fit) and the precision of the extrapolation to the scintillator surface;
- region through which the trajectory passed;

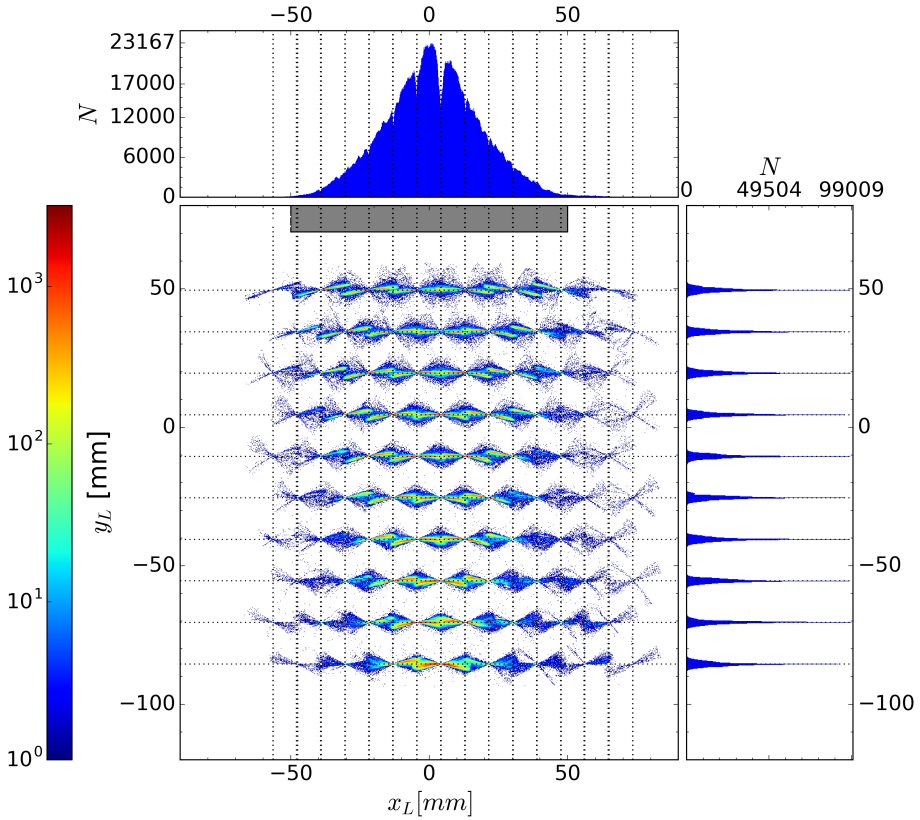


Figure 6.20: Two-dimensional histogram of (x_l, y_l) pairs, visualizing all the positions where ^{207}Bi trajectories were detected, with casts at x and y axis. Positions of signal wires are marked by dotted black lines.

Using the cut based on the fit quality sharpens the scintillator shaped borders, which suggest that hits outside the scintillator came from noisy events. If needed, hits located in suspicious regions (cell center, cell periphery) can be rejected from the fit. Additionally, the radiation source can be moved during the measurement to diversify the span of trajectories, thus evening out the channeling/blocking effect of the periodic structure of the cells (Fig. 6.18 vs 6.19). Moreover, the fitting procedure will be tested on the data obtained from simulations, to verify if no systematic errors are introduced by the procedure itself.

In addition, problems with the accuracy of the positioning close to the cell center can cause systematic shifts in the extrapolation. In order to eliminate

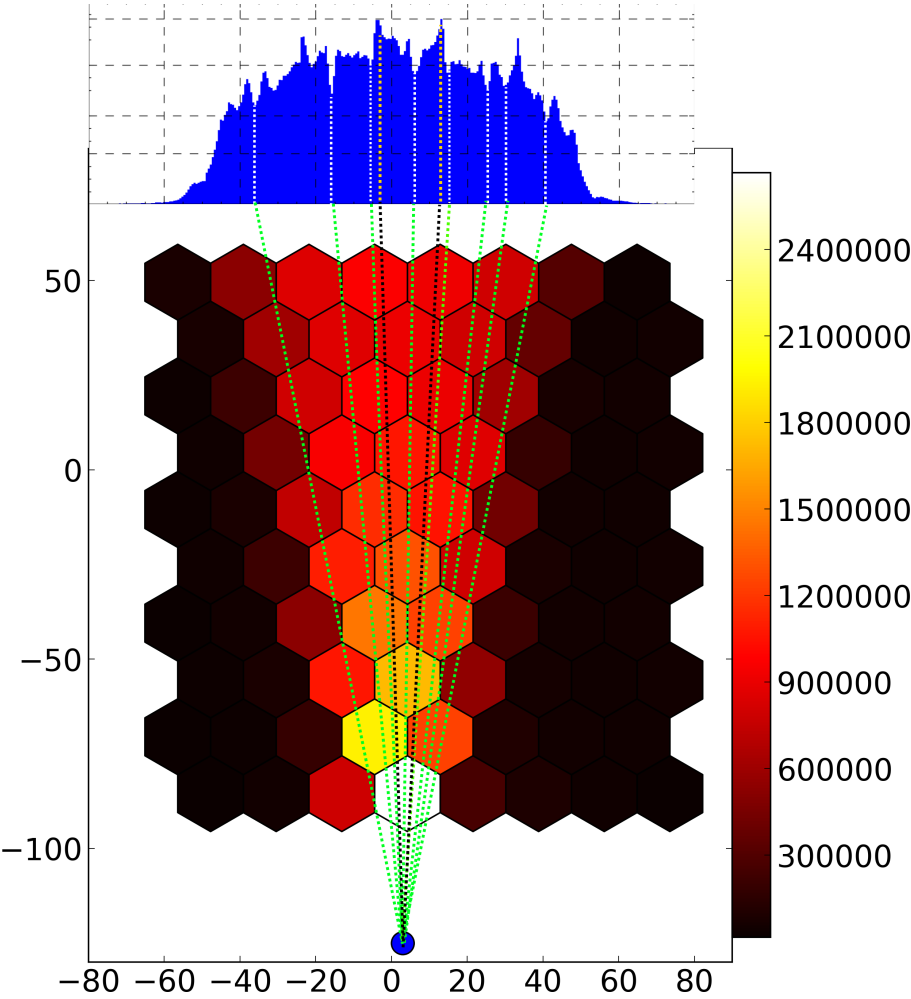


Figure 6.21: Visualization of the correlation between paths connecting the ^{207}Bi source (blue dot) with locations at the scintillator where bigger differences in the number of counts were detected. The cell color indicates the number of hits detected by that cell.

this possibility, weights related to $\sigma(r)$ (Sec. 5.4.1) will be implemented in the xy -fit.

Chapter 7

Towards measurements of the energy spectrum

7.1 Overview

The ultimate goal of the miniBETA project is to precisely measure the beta spectrum shape of interesting transitions, which could lead to a better understanding of the Standard Model and the physics beyond it. A plastic scintillator was chosen for measuring the energy of the electrons. This material benefits from having a low atomic number Z , which significantly reduces the probability of backscattering and bremsstrahlung. These processes can reduce the precision of an experiment as their influence on the measured spectrum is known with limited accuracy [30].

The effect of the Fierz term b and weak magnetism f_M on the spectrum is energy dependent: $\propto 1/E$ and $\propto E$, respectively. Therefore, special care has to be taken when the energy response of the spectrometer is being calibrated. Small uncertainties in the energy response can lead to significant systematic uncertainties in the extraction of b and f_M , which can dominate the uncertainty of the experiment [86].

The prototype version of the miniBETA spectrometer was focused on the idea of using the drift chamber as a particle tracker, which (inter alia) can improve the energy resolution and calibration accuracy of the large plastic scintillator. This is achieved thanks to the information where particles hit the surface of the scintillator. Even though the scintillator and light guide setup was not optimized

in the prototype version, it helped to develop methods and algorithms for the calibration of the spectrometer, setting the ground for precise spectroscopic measurements.

The method of calibrating the detector response, based on comparison of simulated and measured spectra of the ^{207}Bi source, is presented in the following section. This isotope is well suited for the calibration because it emits conversion electrons, which energies are discrete (Tab. 7.1). Additionally, results of a preliminary spectrometer calibration are presented.

Table 7.1: Electrons emitted from ^{207}Bi with the highest absolute intensities $I(abs)$ [%] and energies $E > 100$ keV. The label “origin” indicates from which shell the conversion electron is ejected [74].

E [keV]	$I(abs)$ [%]	origin
481.69	1.537	K
554.41	0.442	L
566.06	0.111	M
975.65	7.08	K
1048.1	1.84	L
1059.92	0.44	M

7.2 Simulation of the energy spectrum

A detailed simulation of the ^{207}Bi decay products and their kinematics, in the miniBETA spectrometer, was performed using the GEANT4 framework [55, 87]. The goal was to extract from the simulation the deposited energy spectrum of particles hitting the scintillator. Such spectrum can be compared with the spectrum measured with the real setup. Comparing the spectra allows to extract properties of the spectrometer, i.e. the energy response and resolution of the detector.

The simulation included the complete geometry of the spectrometer, filled with the He-Iso 50/50 mixture at 600 mbar, with the source of 1 mm diameter and 30 nm thickness, sealed between 12 μm mylar foil sheets, mounted in the source positioning system. The isotope’s decay was included according to the decay scheme from the GEANT4 library and the emitted radiation was traced in the detection setup.

A flag was used to mark the type of the radiation emitted. In the analysis, only electrons were selected because gammas are not leaving a proper trace in the drift chamber, thus they cannot be misinterpreted by the analysis software and their energies are not added to the measured spectrum. In this step electrons from all sources are flagged, including the ones created from gamma conversions in Compton and photoelectric processes.

Finding the trajectory of a detected particle allows to determine the positions where the particle hit the scintillator and where the trajectory crossed the plane where the source is located. The latter position is used to verify if the particle might have been emitted by the decaying source. Only electrons with trajectories passing in the vicinity of the source ($r = 5$ mm) were selected for the analysis. In addition, only electrons hitting a circle of $r=5$ mm in the center of the scintillator were accepted. This requirement matches the condition which is used when measured events are selected (Sec. 7.4). The simulation did not include cosmic muons, because their influence on the measured spectrum, with the above conditions, is negligible: the ratio of muons/electrons fulfilling the conditions is $\sim 10^{-4}$.

The total length of the radiation path was recorded as well. It was used to eliminate events where too much scattering (also from the chamber walls) occurred, since the 3D tracking applied to the measured data should filter out this kind of events, due to their poor fit quality ξ .

An additional flag is used to indicate if the electron originated from Compton scattering. As such electrons cannot be distinguished from betas nor conversion electrons during the analysis of the experimental data, they are also included in the selected subset. However, it was observed that Compton electrons are almost completely cleared from the simulated spectrum if one limits the accepted point of particle origin to the vicinity of the source, hence their influence on the spectrum can be neglected (see Figs. 7.1 and 7.2).

A histogram of deposited energies of simulated particles fulfilling all of the above conditions was created (Fig. 7.2). The most visible peaks come from electrons from K-, L- and M- shells. Peaks are broadened with a tail to the left, mainly due to energy losses along the electron paths.

7.3 Positional dependency of the spectrometer response

The ^{207}Bi source was mounted in the chamber filled with the 50/50 He-Iso mixture at 600 mbar. Figure 6.21 shows a visualization of the chamber geometry

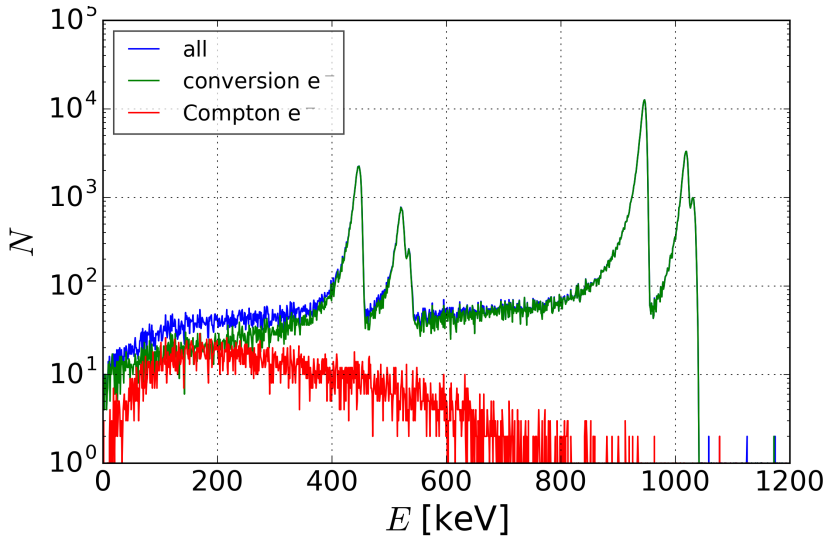


Figure 7.1: Spectrum of ^{207}Bi electron energies deposited in the scintillator, simulated with GEANT4. The chamber was filled with 50/50 Iso-He mixture at 600 mbar. Only electrons depositing energies near the center of the scintillator were selected.

with the cell color corresponding to the number of counts reported by that cell during the measurement.

The analysis software reconstructed 3D trajectories of the measured events, according to the previously described algorithms, including all the mentioned corrections, based on the calibration obtained from the measurement with cosmic muons, performed in advance in similar conditions.

Figure 7.3 presents the total (unfiltered) measured energy spectrum, for events with hits from at least 5 planes. The spectrum with no distinguishable peaks does not look like the ^{207}Bi electron spectrum at all. It was found that this misleading picture is caused by the fact that the amount of light collected by the PMT depends significantly on the distance R between the scintillator center and the location where the scintillator was hit.

For each event, the position (x, z) , where the electron hit the scintillator, was determined and its distance $R = \sqrt{x^2 + z^2}$ from the scintillator center was calculated. Figure 7.4 shows a 2D histogram of pairs (E, R) , determined for all selected events. The bin content was normalized by the factor $2\pi R dR$ to make it independent from the detection area, and scaled so that the highest

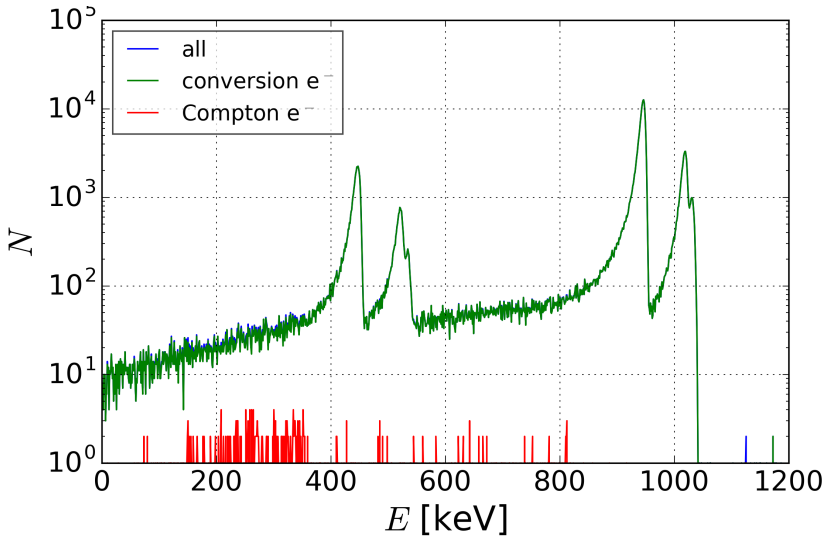


Figure 7.2: As Fig. 7.1 but limited to trajectories originating from the vicinity of the source.

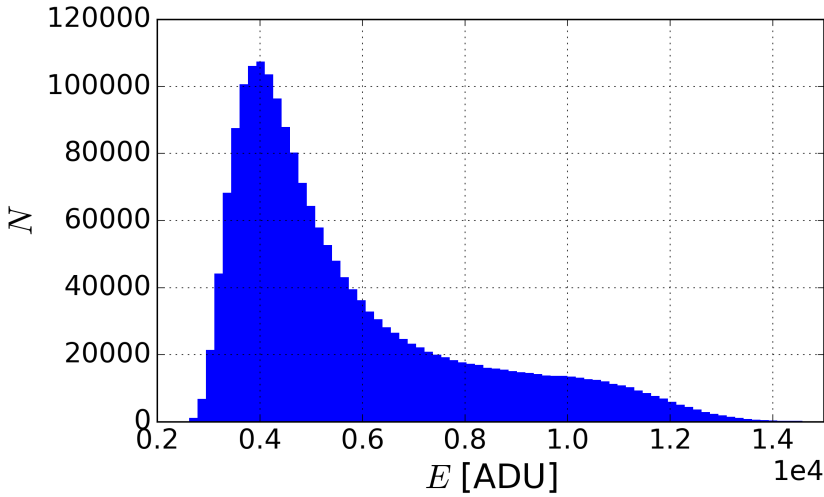


Figure 7.3: Total energy spectrum of the measured radiation coming from the ^{207}Bi source. The only selection condition was that the event consisted of at least 5 hits. The chamber was filled with a 50/50 He-Iso mixture at 600 mbar.

value is 1. One can notice a λ -like shape emerging from the picture. The two “legs” correspond to the two groups of energy lines of ^{207}Bi conversion electrons, around 500 and 1000 keV.

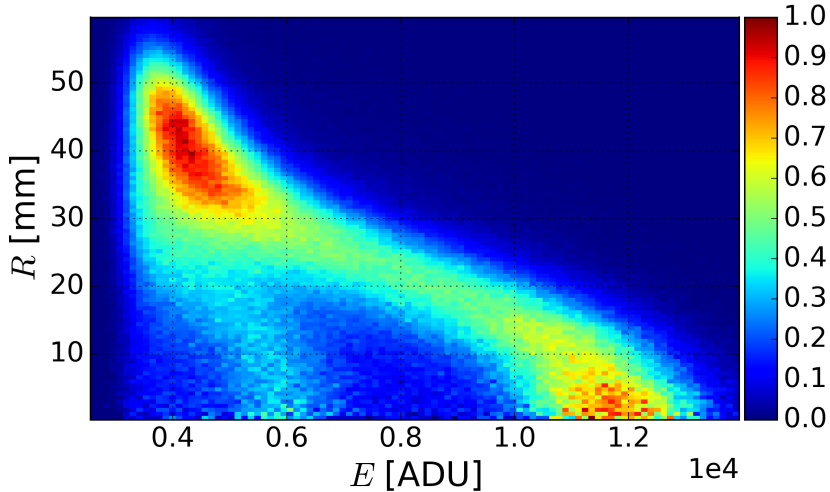


Figure 7.4: Two-dimensional histogram of (E, R) pairs, showing the correlation between the measured energy E and the distance R of a hit from the scintillator center. The chamber was filled with 600 mbar of 50/50 He-Iso mixture and the ^{207}Bi source was used. The content of each bin was divided by the factor $2\pi R dR$ so that the number of counts no longer depends on the detection area. Additionally, all bins were divided by the value of the highest one so the scale ranges from 0 to 1.

At the center of the scintillator ($R \approx 0$ mm) these groups are easier to be recognized but the further from the center the smaller the distance between them. Above $R \approx 25$ mm they are no longer distinguishable. This behavior is a result of the positional dependence of the spectrometer response, based on the scintillation light collection efficiency. The further from the center of the PMT, the more photons are lost before reaching the PMT. If electrons of the same E hit the scintillator at two different R , even though they have created the same amount of photons, the number of photons collected by the PMT, hence the ADC readout value, will vary.

This effect causes a systematic shift in the measured spectrum and leads to a drop of the spectrometer energy resolution, if not taken into account. The positions of the energy lines are moved to the left on the readout scale with increasing distance R from the center of the scintillator, thereby broadening

the peaks. To minimize the influence of this effect the acceptance range in the analysis was limited to $R < 5$ mm. Figure 7.5 shows the recorded spectrum for such events. Two peaks emerge in the spectrum around 0.55 and $1.15 \cdot 10^4$ ADU.

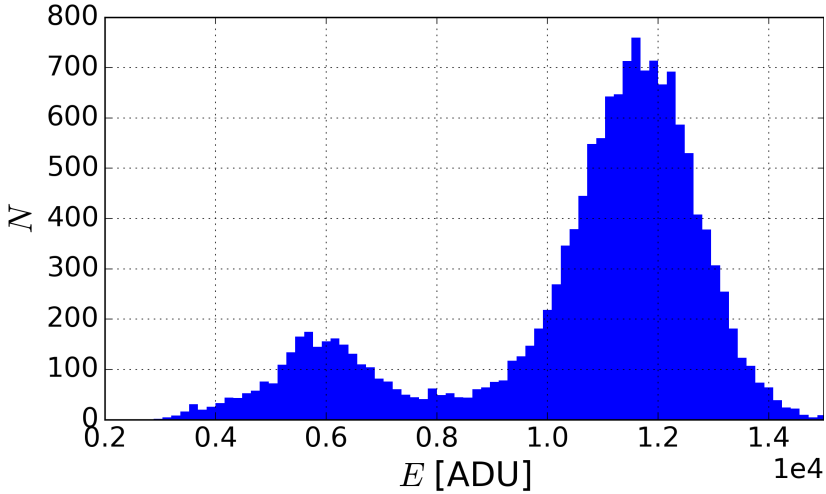


Figure 7.5: Like Fig. 7.3 but after the cut on the distance R was applied, limiting the plotted energies to the ones corresponding to electrons hitting the scintillator near its center ($R < 5$ mm).

7.4 Convolution-based method for calibrating the energy response of the spectrometer

A standard procedure of determining the energy response of a spectrometer is based on fitting a spectrum obtained from a measurement, to a spectrum provided by some model. The model spectrum of ^{207}Bi can be created as a sum of several distribution functions (e.g. Gaussian-like), corresponding to the dominant energy lines [88]. Relative heights and positions of these distributions are fixed according to the decay scheme of the isotope. The background shape is chosen arbitrarily, often as a polynomial. The accuracy of this method depends on how well a singular distribution is defined, e.g. if and how it includes energy losses along the particle path.

In this thesis, a different approach is presented. Since the energy spectrum of electrons reaching the scintillator $Y(E)$ is well known from the simulation, already including energy losses along particle trajectories and the presence of

the background, it is beneficial to use this knowledge in the fit. Using the simulated spectrum allows for a holistic approach to the problem, without the need for a detailed understanding of all the processes involved in it. Their understanding is beneficial for validation of the simulation but is not crucial for the spectrometer calibration. It also allows for a better separation of the spectrometer part from all the processes happening in the tracker.

A spectrometer with perfect energy resolution would always report the same value for monoenergetic radiation. In general, spectrometers operate in a mode, where the recorded value is proportional to the number of charge carriers (or photons for a scintillator) created in a process of interaction between a detected particle and the detector medium. Assuming that the average energy spent for the creation of a single carrier does not depend strongly on the incident energy, the average number of generated carriers N is essentially proportional to the total deposited energy E . Creation of carriers is a statistical process and the distribution of N can be approximated by the Poisson distribution [47]. Thus, the standard deviation is given by $\sigma = \sqrt{N}$.

The resolution of the spectrometer used in the measurements was approximated with a more general function:

$$\sigma_E = R_0 + F \cdot \sqrt{E}, \quad (7.1)$$

which includes the influence of the counting statistics, scaled with a parameter F , and allows for additional factors that affect the resolution but are energy independent, e.g. electronic noise, combined as R_0 .

To emulate the process of the spectrometer response, broadening the recorded spectrum, a Gaussian function $G(x)$ was used:

$$G(x) = \frac{A}{\sigma_E \sqrt{2\pi}} \exp\left(\frac{-x^2}{2\sigma_E^2}\right), \quad (7.2)$$

where A is a parameter scaling the spectrum height and σ_E is the detector resolution, described by Eq. (7.1)

For two random and independent variables $y \in Y$ and $g \in G$, the probability distribution C of their sum is given by the convolution of their individual distributions:

$$C(y + g)(E) = (Y * G)(E) := \sum_{\tau=-\infty}^{\infty} Y(E - \tau)G(\tau), \quad (7.3)$$

This means that the final spectrum C can be obtained by convolving the simulated spectrum Y with the Gaussian response G of the spectrometer. The

result can then be compared with the experimentally measured spectrum M in order to find the missing parameters of the calibration.

A linear dependency was used to obtain the energy E in keV from the recorded vales in ADU:

$$M[\text{keV}] = S[\text{keV/ADU}] \cdot M[\text{ADU}] + O[\text{keV}], \quad (7.4)$$

where S and O are scale parameters.

The standard procedure of least squares was used to minimize residua ϵ :

$$\epsilon(E) = C(E) - M(E), \quad (7.5)$$

where the following parameters of the distributions were fitted:

- S and O , as parameters of the spectrometer calibration $M[\text{ADU}] \rightarrow M[\text{keV}]$;
- A , as the parameter in G , scaling the height of the simulated spectrum Y to match the measured one M ;
- R_0 and F , as parameters depending on the spectrometer resolution.

For numerical reasons, limits of the summation in the convolution were reduced to $(-5\sigma, 5\sigma)$. Values of parameters resulting in the best match between the C and the M are:

$$\begin{aligned} S &= 0.08112(49) \text{ keV ADU}^{-1}, \\ O &= 11.32(49) \text{ keV}, \\ A &= 0.6850(91), \\ R_0 &= 44.9(9.1) \text{ keV}, \\ F &= 0.98(26) \text{ keV}^{1/2}. \end{aligned}$$

Figure 7.6 presents $C(E)$ and $M(E)$ with the above parameters.

The fit quality might suffer from some additional systematic effects not yet included. The setup used in the measurement was not optimized for spectroscopy and probably distorted the energy spectrum. The whole spectroscopic part (scintillator and PMTs) will be modified in the next version of the setup.

The resolution ρ_E of a spectrometer can be defined as:

$$\rho_E = \frac{\sigma_E}{E}, \quad (7.6)$$

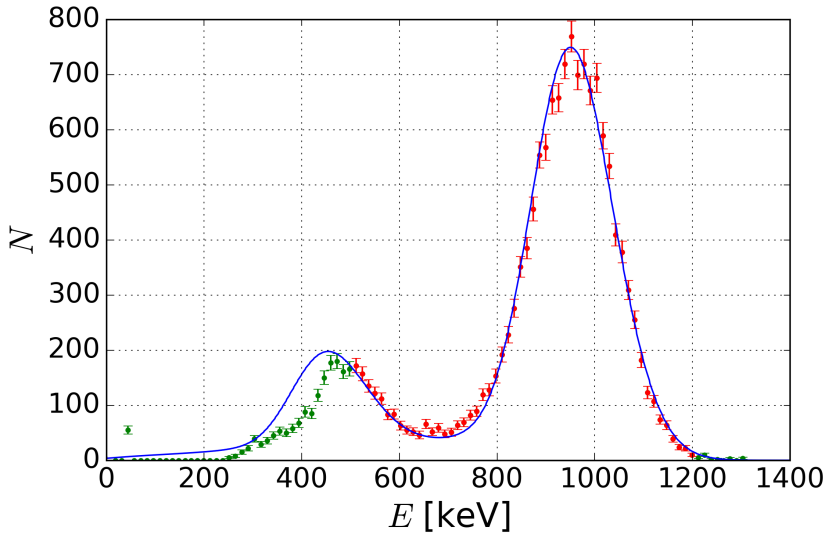


Figure 7.6: Results of matching the spectrum of measured energy E (dots) with the convolution of the simulated spectrum and the spectrometer response (solid blue line). Only the red points were used in the fit because the detection threshold distorted the low energy side of the measured spectrum.

where σ_E is the standard deviation of a peak corresponding to the detection of particles with an energy E . The resolution determined from the fit parameters at 1 MeV is $\rho_{1\text{MeV}} = 7.60(14)\%$.

It is important to stress an essential influence of the S parameter, or to be more specific - of its uncertainty $\sigma(S)$, on the extraction of the weak magnetism and Fierz term from the spectrum shape. The uncertainty of S directly constrains the precision of determining energy-dependent terms, as their influence on the spectrum cannot be distinguished from the influence of the spectrometer response, within the limits of $\sigma(S)$. Therefore, the use of the tested setup without improvements would result in a limitation of the precision of spectrum shape measurements to $\sim 5 \cdot 10^{-3}$.

The next miniBETA setup will tackle directly the issue of $\sigma(S)$, as it is focused on optimizing the spectroscopic part of the experiment. The scintillators will be exchanged for bigger ones, providing a greater solid angle for the particle detection. Four PMTs will be used at each side of the chamber and the light guide geometry was optimized to increase the homogeneity of the light collection. In addition, the detection surface will be divided (in the software) into small sections and an individual energy calibration will be determined for each one of

them. This means that a gain map will be determined for the whole scintillator area. It will also be important to analyze the influence of the in-gas scattering on correlations between the fit quality ξ , the energy E of a β particle, and slopes of the particle's trajectory.

7.5 Summary

A preliminary measurement with the ^{207}Bi source was performed, which allowed for development and tests of the calibration procedure. In this, the simulated spectrum is convolved with a Gaussian distribution, emulating the finite resolution of the spectrometer. The fitting algorithm is constructed in a way that allows for high flexibility in choosing the detector response function, which can be beneficial for precise measurements.

High spatial inhomogeneity in the light collection of the spectrometer was observed, which resulted in a poor spectroscopic resolution of this prototype setup. It was shown, that tracking of particles can significantly increase the resolution of the spectrometer. Determining the position where the scintillator was hit allows for fine-tuning of the detector calibration, taking into account the spatial inhomogeneity of the detector performance.

The determined energy resolution of the spectrometer, $\rho_{1\text{MeV}} = 7.60(14)\%$, is worse than standards for plastic scintillators but one has to remember that the prototype setup was not optimized for energy measurements. Moreover, the uncertainty of the scale parameter S in the spectrometer response function limits the precision of spectrum shape measurements to $\sim 5 \cdot 10^{-3}$.

The observed problems will be solved during the ongoing upgrade of the spectroscopic part of the system. A new, bigger scintillator will be installed, with a light guide designed to maximize uniformity of light collected by 4 PMTs. This upgrade will also help to obtain a spectrum with the desired statistics since the scintillator area will be significantly bigger. It is believed, that $\rho_{1\text{MeV}} = 5\%$ can be easily reached with an optimized setup, as this was already achieved by members of the collaboration [88]. It is also believed, that the systematic uncertainty resulting from $\sigma(S)$ will be $\sim 10^{-3}$.

Chapter 8

Conclusions

The particle tracking in the multiwire drift chamber of the miniBETA spectrometer was successfully commissioned. The thesis described the whole process, starting from the measurements involving only a single signal plane, where the detector performance was evaluated based on simplified properties, like counting rates, up to the full-scale experiment, where trajectories of electrons, emitted from the source mounted inside the chamber, were reconstructed in three dimensions, providing detailed information about the detector characteristics.

The choice of helium, as the main component of the mixture, is motivated by its low Z , which is highly beneficial for the spectroscopic goal of the experiment, as it significantly limits the energy losses along the particle path to the detector. Moreover, the chamber operates at lower than atmospheric pressure, which reduces the losses even further. Low energy losses, beneficial for spectroscopy, are the limiting factor for the particle tracking accuracy, as they diminish the primary ionization statistics. A similar compromise was made when the hexagonal shape of the cell was chosen. Electric field uniformity, simplifying the electron drift behavior, was sacrificed in favor of higher transparency of the chamber. These choices introduced several experimental challenges, which were tackled in this thesis.

The single plane measurements allowed to test a series of helium-isobutane based gas mixtures and their viability as the ionization medium in the planned experiment. It was found, that the crucial parameter for efficient detection is the signal height, which depends on the gas gain of the mixture and the amount of primary ionization. This was not surprising since a signal always has to pass some threshold of detection. The phenomenological method of quick

verification whether signals are high enough, based on the ADC spectrum shape, was introduced.

Ranges of voltages resulting in the highest, yet stable, gas multiplication were marked. Possible sources of noise, like the so-called after-pulses, were identified and methods of limiting their influence were shown. Use of the independent data acquisition module, i.e. FASTER made by LPC Caen, allowed to cross-check the performance of the custom made miniBETA DAQ, and led to its further improvement.

Four mixtures of helium-isobutane, at pressures going down to 300 mbar, were tested in detail with the full setup. The drift time-to-radius relation was determined for each mixture and each cell individually by an iterative autocalibration procedure, based on the detection of cosmic muons.

The accuracy of the particle tracking in the xy -projection was found to be about 0.4 mm for the 50/50 and 70/30 mixtures at 600 mbar. The other mixtures showed worse performance. The accuracy of the 50/50 at 300 mbar is approximately twice worse than of the same mixture at 600 mbar, which follows the limitations of the primary ionization statistics. Moreover, very high ionization detection efficiency was achieved for all the mixtures. An efficiency better than 0.99 was reached in the vast majority of the cell area for the mixtures at 600 mbar, and 0.97 for the 50/50 mixture at 300 mbar.

The usability of the charge division technique for particle tracking in the third dimension, i.e. aligned with the wire direction, was evaluated. The accuracy of this technique is an order of magnitude worse and the efficiency is reduced by about 12 percents. The difference comes from technical limitations of the system, with the accuracy dominated by the influence of the preamplifiers noise, and the efficiency limited by the ADC range.

It was also shown that the accuracy of extracting the position where the scintillator was hit, from the fitted trajectory extrapolation, is comparable with the accuracy of the tracking in the single cell.

In this work, special attention was also paid to the systematic effects affecting the measurements, as they are the limiting factor as to experimental precision. Numerous corrections were introduced, taking into account effects like the time walk and wire placement misalignment, some of these having a significant effect on the detector performance. However, the observed interference-like pattern, appearing when the trajectories are extrapolated to the scintillator surface, requires further investigation, preferably with a cross-check based on simulations.

The simulations will, in addition, be beneficial to determine the backscattering recognition efficiency. The developed tracking software can be easily upgraded, adding a pattern recognition module, able to divide cells taking part in an event into subsets corresponding to possibly independent structures. The main fit will then find the best trajectory for each such subset. If the crossing point of such trajectories is situated on the scintillator surface this would indicate that backscattering from the scintillator might have occurred.

In the last part, an insight into the actual spectrum shape measurement was presented. Although the commissioned version of the detector was not optimized for spectroscopy, it nevertheless allowed for a preliminary test of the methodology based on the modular approach. This method decouples the physics related to the energy losses along the particle path from the physics of the energy detector and its response. It is believed that such approach is beneficial for precision-oriented experiments, as it allows for better control over several individual factors affecting the spectrum shape, which are most of the time obscured by the convoluted final observable.

Initial measurements showed that the main factor limiting the precision of a spectrum shape measurement is a spatial nonuniformity of the spectrometer response. Particle tracking in the drift chamber is crucial to minimize this effect. Moreover, the geometry of the spectrometer can be modified to improve light collection efficiency, which is responsible for the nonuniformity. With the choice of plastic as the detector material, the influence of the backscattering on the spectrum shape is minimized and can be treated as a higher-order correction. Nevertheless, a different kind of a spectroscopy detector (eg. silicon strip detector) can be used with the miniBETA setup and tracking of particles will allow for proper treatment of the backscattering.

The prototypical version of the miniBETA detector was heavily exploited during the commissioning phase. The important part of the chamber, i.e. the signal planes, was damaged during measurements testing the limits of the system. A new version of the setup is now being prepared and tested. Brand new planes were made with improved electrical protection. The preamplifiers' design was enhanced as well, which should result in lower noise and better stability of their operation. Finally, a completely new scintillator with a three times bigger detection surface, twice better efficiency and significantly improved homogeneity thanks to the readout with 4 PMTs, was produced and is currently tested.

The influence of weak magnetism on a β spectrum shape can be even an order of magnitude higher than the influence of the Fierz interference term. Therefore, the miniBETA experiment will focus first on measuring weak magnetism. The first planned beta spectrum shape measurement will use the indium isotope

^{114m}In , where weak magnetism is estimated to affect the spectrum at the level of 10^{-3} - 10^{-2} [26, 55].

Appendix A

Tables of cell efficiencies

Table A.1: Mean cell efficiencies, xy -fit for muon trajectories, 50/50@600 mbar.

#p↓ #w→	1	2	3	4	5	6	7	8
1	0.9968(10)	0.9880(16)	0.9812(17)	0.9830(15)	0.9790(16)	0.9821(15)	0.9801(17)	0.9950(10)
2	0.9907(16)	0.9336(34)	0.9794(17)	0.9797(15)	0.9800(15)	0.9667(20)	0.9679(22)	0.9768(41)
3	0.9934(18)	0.9863(17)	0.9730(20)	0.9762(17)	0.9760(16)	0.9756(16)	0.9857(14)	0.9911(16)
4	0.9936(14)	0.9864(16)	0.9744(18)	0.9777(15)	0.9758(15)	0.9779(16)	0.9900(13)	0.284(28)
5	0.9971(21)	0.9863(18)	0.9832(16)	0.9874(12)	0.9817(13)	0.9857(12)	0.9857(14)	0.9273(58)
6	0.9831(32)	0.9822(18)	0.9845(14)	0.9807(14)	0.9787(14)	0.9758(16)	0.9871(17)	0.899(24)
7	0.956(25)	0.9835(23)	0.9803(16)	0.9819(13)	0.9839(12)	0.9819(13)	0.9834(15)	0.9739(44)
8	0.9737(69)	0.9889(14)	0.9873(11)	0.9855(12)	0.9811(13)	0.9841(13)	0.9887(16)	0.917(25)
9	0.958(29)	0.9400(57)	0.9863(13)	0.9831(13)	0.9826(13)	0.9814(13)	0.9786(16)	0.330(13)
10	0.960(20)	0.9876(16)	0.9840(12)	0.9813(13)	0.9832(13)	0.9688(18)	0.9790(19)	0.700(39)

Table A.2: Mean cell efficiencies, xy -fit for muon trajectories, 70/30@600 mbar.

#p↓ #w→	1	2	3	4	5	6	7	8
1	0.99609(78)	0.9865(12)	0.9814(12)	0.9806(11)	0.9795(11)	0.9817(10)	0.9821(11)	0.99311(83)
2	0.9910(11)	0.9532(20)	0.9767(12)	0.9794(11)	0.9795(10)	0.9732(13)	0.9727(14)	0.9661(34)
3	0.9804(21)	0.9874(12)	0.9771(13)	0.9803(11)	0.98184(95)	0.98215(98)	0.98948(84)	0.9852(15)
4	0.9896(13)	0.9877(10)	0.98601(95)	0.98251(93)	0.9769(10)	0.98265(99)	0.98913(96)	0.384(22)
5	0.9702(44)	0.9862(13)	0.98689(98)	0.98520(88)	0.98288(89)	0.98446(87)	0.98795(88)	0.9781(23)
6	0.9892(18)	0.9848(11)	0.98567(91)	0.98331(88)	0.98453(84)	0.98183(95)	0.9888(11)	0.906(17)
7	0.882(35)	0.8665(43)	0.8634(28)	0.8630(24)	0.98634(79)	0.98623(79)	0.98509(97)	0.9658(35)
8	0.9699(55)	0.98986(97)	0.99009(71)	0.98555(81)	0.98723(76)	0.98919(73)	0.9880(12)	0.891(21)
9	0.902(42)	0.9757(27)	0.98809(83)	0.98394(87)	0.98257(89)	0.98432(86)	0.9808(11)	0.3597(94)
10	0.909(25)	0.9882(11)	0.98803(75)	0.98767(75)	0.98663(79)	0.98557(88)	0.9880(10)	0.774(27)

Table A.3: Mean cell efficiencies, xy -fit for muon trajectories, 50/50@300 mbar.

#p↓ #w→	1	2	3	4	5	6	7	8
1	0.9973(13)	0.9702(36)	0.9713(31)	0.9657(30)	0.9645(30)	0.9698(28)	0.9679(31)	0.9875(22)
2	0.9644(44)	0.7403(88)	0.9051(51)	0.9150(44)	0.9345(39)	0.9099(47)	0.8915(57)	0.9183(96)
3	0.9746(50)	0.9497(47)	0.9276(48)	0.9462(37)	0.9362(37)	0.9420(36)	0.9670(31)	0.9635(44)
4	0.9823(34)	0.9535(41)	0.9416(40)	0.9192(41)	0.9399(35)	0.9304(40)	0.9550(39)	0.928(16)
5	0.9965(35)	0.9570(45)	0.9491(39)	0.9342(39)	0.9335(36)	0.9484(33)	0.9440(38)	0.9619(56)
6	0.9742(60)	0.9584(38)	0.9516(35)	0.9493(32)	0.9465(32)	0.9339(37)	0.9558(43)	0.884(26)
7	0.82(12)	0.9633(49)	0.9400(40)	0.9475(33)	0.9406(34)	0.9526(31)	0.9442(38)	0.9587(66)
8	0.915(21)	0.9610(38)	0.9423(35)	0.9179(40)	0.9394(34)	0.9408(35)	0.9453(48)	0.894(30)
9	0.83(15)	0.9391(90)	0.9422(37)	0.9307(37)	0.9447(33)	0.9398(35)	0.9371(40)	0.9421(76)
10	0.913(59)	0.9634(40)	0.9583(29)	0.9593(28)	0.9671(26)	0.9672(28)	0.9816(26)	0.879(33)

Table A.4: Mean cell efficiencies, xy -fit for muon trajectories, 0/100@300 mbar.

#p↓ #w→	1	2	3	4	5	6	7	8
1	0.9963(12)	0.9829(21)	0.9771(21)	0.9788(18)	0.9763(18)	0.9767(19)	0.9784(19)	0.9900(15)
2	0.9823(24)	0.9271(40)	0.9699(22)	0.9772(18)	0.9737(19)	0.9571(25)	0.9561(28)	0.9514(57)
3	0.9822(30)	0.9658(30)	0.9640(26)	0.9511(26)	0.4691(57)	0.9576(24)	0.9760(20)	0.9668(32)
4	0.9482(42)	0.7912(62)	0.8515(45)	0.8323(43)	0.4831(55)	0.9700(20)	0.9779(21)	0.9690(76)
5	0.9874(42)	0.9682(29)	0.9741(22)	0.9774(17)	0.9707(19)	0.9817(15)	0.9801(18)	0.9693(38)
6	0.9727(42)	0.9656(27)	0.9652(22)	0.9672(20)	0.9694(19)	0.9574(23)	0.9731(25)	0.934(14)
7	0.258(39)	0.2508(83)	0.2413(55)	0.2439(48)	0.9743(17)	0.9754(17)	0.9724(21)	0.9770(37)
8	0.935(10)	0.9787(22)	0.9785(16)	0.9765(17)	0.9763(17)	0.9732(18)	0.9645(28)	0.928(17)
9	0.912(34)	0.9701(44)	0.9758(18)	0.9791(16)	0.9763(17)	0.9788(16)	0.9798(18)	0.9733(37)
10	0.904(23)	0.9847(18)	0.9839(14)	0.9832(14)	0.9819(15)	0.9756(18)	0.9803(20)	0.853(23)

Table A.5: Mean cell efficiencies, y -fit for muon trajectories, 50/50@600 mbar.

#p↓ #w→	1	2	3	4	5	6	7	8
1	0.2720(80)	0.7006(65)	0.7763(51)	0.8040(43)	0.7847(43)	0.7572(45)	0.7753(47)	0.7253(60)
2	0.7600(68)	0.8615(45)	0.8291(43)	0.7979(41)	0.8099(40)	0.8900(33)	0.8332(45)	0.8503(89)
3	0.288(12)	0.8479(51)	0.8801(39)	0.8864(34)	0.8844(31)	0.9006(30)	0.7553(47)	0.8908(51)
4	0.5117(96)	0.7469(56)	0.7716(46)	0.8236(38)	0.7988(38)	0.8298(38)	0.8331(47)	0.0(0)
5	0.430(31)	0.8144(60)	0.8428(43)	0.8668(35)	0.8182(36)	0.6856(44)	0.7850(44)	0.8266(77)
6	0.722(13)	0.8193(50)	0.8389(39)	0.8143(37)	0.8629(32)	0.8699(33)	0.8968(42)	0.746(27)
7	0.25(11)	0.8001(76)	0.7094(51)	0.8630(33)	0.8644(32)	0.8463(33)	0.8645(37)	0.8695(79)
8	0.729(26)	0.8272(52)	0.8181(38)	0.8185(36)	0.8678(32)	0.8643(33)	0.8785(45)	0.737(32)
9	0.095(64)	0.774(11)	0.8546(38)	0.8531(34)	0.8285(35)	0.8229(36)	0.7378(46)	0.0(0)
10	0.387(51)	0.8186(55)	0.8390(35)	0.8590(33)	0.8506(34)	0.8943(31)	0.8935(38)	0.655(31)

Table A.6: Mean cell efficiencies, y -fit for muon trajectories, 70/30@600 mbar.

#p↓ #w→	1	2	3	4	5	6	7	8
1	0.9443(77)	0.9863(16)	0.9889(11)	0.98882(99)	0.9878(10)	0.9849(11)	0.99059(98)	0.99479(89)
2	0.688(10)	0.8464(44)	0.7959(40)	0.7757(37)	0.7913(36)	0.8725(32)	0.8052(44)	0.8315(84)
3	0.215(22)	0.7986(66)	0.8345(41)	0.8488(33)	0.8388(31)	0.8563(31)	0.7124(45)	0.8411(55)
4	0.434(17)	0.6603(61)	0.7116(44)	0.7480(37)	0.7260(37)	0.7509(40)	0.7474(50)	0.0(0)
5	0.403(58)	0.7282(94)	0.7545(47)	0.7908(36)	0.7485(36)	0.6497(40)	0.7068(45)	0.7968(79)
6	0.601(29)	0.7207(65)	0.7801(39)	0.7579(36)	0.7977(33)	0.7884(36)	0.8222(49)	0.694(27)
7	0.50(35)	0.614(13)	0.5831(55)	0.6973(39)	0.7988(33)	0.7563(35)	0.7879(40)	0.7852(91)
8	0.462(52)	0.6995(72)	0.6853(42)	0.6894(38)	0.7636(35)	0.7521(37)	0.7878(53)	0.681(34)
9	0.091(87)	0.712(15)	0.7867(44)	0.7973(35)	0.7763(34)	0.7759(35)	0.6914(44)	0.0(0)
10	0.278(50)	0.5608(74)	0.4914(46)	0.5239(42)	0.4714(42)	0.6712(42)	0.6772(54)	0.570(36)

Table A.7: Mean cell efficiencies, yz -fit for muon trajectories, 50/50@300 mbar.

#p↓ #w→	1	2	3	4	5	6	7	8
1	0.9935(27)	0.9875(25)	0.9867(24)	0.9896(18)	0.9871(19)	0.9789(26)	0.9891(19)	0.9947(15)
2	0.849(10)	0.7069(98)	0.8385(72)	0.8542(58)	0.8638(57)	0.8438(64)	0.8315(72)	0.882(12)
3	0.441(22)	0.8675(80)	0.7727(88)	0.8435(62)	0.8776(52)	0.8634(57)	0.8564(62)	0.9068(71)
4	0.784(14)	0.8560(75)	0.6812(89)	0.8011(63)	0.8580(55)	0.8258(63)	0.7270(88)	0.671(30)
5	0.348(44)	0.8668(90)	0.8503(71)	0.8576(58)	0.8517(54)	0.8699(52)	0.8105(69)	0.878(10)
6	0.747(22)	0.8456(80)	0.8686(61)	0.8730(51)	0.8520(53)	0.8506(56)	0.8736(72)	0.632(45)
7	0.25(22)	0.835(12)	0.7107(89)	0.8699(54)	0.8100(59)	0.8334(56)	0.8154(68)	0.835(13)
8	0.598(51)	0.8734(76)	0.8651(59)	0.8526(54)	0.8741(49)	0.8504(57)	0.8858(69)	0.732(45)
9	0.0(0)	0.837(15)	0.8756(61)	0.8764(52)	0.9028(44)	0.8833(49)	0.8740(58)	0.824(13)
10	0.684(75)	0.8812(76)	0.8153(65)	0.8734(50)	0.8732(50)	0.8368(62)	0.9196(54)	0.762(42)

Table A.8: Mean cell efficiencies, yz -fit for muon trajectories, 0/100@300 mbar.

#p↓ #w→	1	2	3	4	5	6	7	8
1	0.9651(70)	0.9844(24)	0.9906(15)	0.9885(15)	0.9877(15)	0.9888(14)	0.9870(16)	0.9938(12)
2	0.795(11)	0.8653(59)	0.8276(54)	0.8252(51)	0.8420(49)	0.8817(42)	0.8165(56)	0.830(10)
3	0.472(27)	0.8569(77)	0.9126(44)	0.8782(43)	0.1975(53)	0.9080(36)	0.7705(56)	0.8886(58)
4	0.535(19)	0.5692(90)	0.6522(67)	0.6230(61)	0.1061(39)	0.8239(47)	0.8157(58)	0.870(16)
5	0.318(45)	0.807(10)	0.8456(56)	0.8630(44)	0.8482(45)	0.7691(51)	0.7843(54)	0.8394(85)
6	0.756(24)	0.8504(69)	0.8349(50)	0.7857(51)	0.8868(39)	0.8550(42)	0.8839(51)	0.810(23)
7	0.158(84)	0.214(13)	0.1760(58)	0.2280(53)	0.8857(38)	0.8636(41)	0.8710(44)	0.8648(85)
8	0.768(38)	0.8824(66)	0.8360(49)	0.8824(40)	0.8981(36)	0.9023(36)	0.8970(49)	0.792(26)
9	0.130(70)	0.788(16)	0.8505(52)	0.8590(44)	0.8495(43)	0.8305(45)	0.7910(54)	0.8135(92)
10	0.302(50)	0.7345(86)	0.7129(60)	0.7289(54)	0.6791(56)	0.8236(49)	0.8197(58)	0.653(29)

Bibliography

- [1] G. 't Hooft, “The making of the standard model,” *Nature*, vol. 448, pp. 271–273, 2007.
- [2] T. Wyatt, “High-energy colliders and the rise of the standard model,” *Nature*, vol. 448, pp. 274–280, 2007.
- [3] J. R. Ellis, “Beyond the standard model with the LHC,” *Nature*, vol. 448, pp. 297–301, 2007.
- [4] Wikimedia. https://commons.wikimedia.org/wiki/File:Standard_Model_of_Elementary_Particles.svg. [Online; accessed 04-07-19].
- [5] E. Tretkoff, “March 1, 1896: Henri Becquerel Discovers Radioactivity.” <https://www.aps.org/publications/apsnews/200803/physicshistory.cfm>. [Online; accessed 04-07-19].
- [6] T. J. Trenn, “Rutherford on the Alpha-Beta-Gamma Classification of Radioactive Rays,” *Isis*, vol. 67, no. 1, pp. 61–75, 1976.
- [7] S. Bilenky, “Neutrino. history of a unique particle,” *The European Physical Journal H*, vol. 38, pp. 345–404, Apr 2013.
- [8] E. Fermi, “An attempt of a theory of beta radiation. 1.,” *Z. Phys.*, vol. 88, pp. 161–177, 1934.
- [9] F. L. Wilson, “Fermi’s Theory of Beta Decay,” *Am. J. Phys.*, vol. 36, no. 12, pp. 1150–1160, 1968.
- [10] W. Greiner and B. Müller, *The Discovery of the Weak Interaction*, pp. 1–24. Berlin, Heidelberg: Springer Berlin Heidelberg, 2009.
- [11] G. Gamow and E. Teller, “Selection Rules for the β -Disintegration,” *Phys. Rev.*, vol. 49, pp. 895–899, Jun 1936.

- [12] S. S. M. Wong, *Introductory nuclear physics*. 1998.
- [13] T. D. Lee and C.-N. Yang, “Question of Parity Conservation in Weak Interactions,” *Phys. Rev.*, vol. 104, pp. 254–258, 1956.
- [14] N. Severijns, *Weak Interaction Studies by Precision Experiments in Nuclear Beta Decay*, pp. 339–381. 08 2004.
- [15] C. S. Wu, E. Ambler, R. W. Hayward, D. D. Hoppes, and R. P. Hudson, “Experimental Test of Parity Conservation in Beta Decay,” *Phys. Rev.*, vol. 105, pp. 1413–1415, Feb 1957.
- [16] M. González-Alonso, O. Naviliat-Cuncic, and N. Severijns, “New physics searches in nuclear and neutron β decay,” *Progress in Particle and Nuclear Physics*, vol. 104, pp. 165 – 223, 2019.
- [17] M. Tanabashi and others., “Review of Particle Physics,” *Phys. Rev. D*, vol. 98, p. 030001, Aug 2018.
- [18] J. C. Hardy and I. S. Towner, “The measurement and interpretation of superallowed $0^+ \rightarrow 0^+$ nuclear β decay,” *Journal of Physics G: Nuclear and Particle Physics*, vol. 41, p. 114004, oct 2014.
- [19] N. Severijns, M. Beck, and O. Naviliat-Cuncic, “Tests of the standard electroweak model in beta decay,” *Rev. Mod. Phys.*, vol. 78, pp. 991–1040, 2006.
- [20] L. Hayen, N. Severijns, K. Bodek, D. Rozpedzik, and X. Mougeot, “High precision analytical description of the allowed β spectrum shape,” *Rev. Mod. Phys.*, vol. 90, p. 015008, Mar 2018.
- [21] J. D. Jackson, S. B. Treiman, and H. W. Wyld, “Possible Tests of Time Reversal Invariance in Beta Decay,” *Phys. Rev.*, vol. 106, pp. 517–521, May 1957.
- [22] J. D. Jackson, S. B. Treiman, and H. W. Wyld, “Coulomb corrections in allowed beta transitions,” *Nucl. Phys.*, vol. 4, pp. 206–212, 1957.
- [23] K. K. Vos, H. W. Wilschut, and R. G. E. Timmermans, “Symmetry violations in nuclear and neutron β decay,” *Rev. Mod. Phys.*, vol. 87, p. 1483, 2015.
- [24] P. Herczeg, “Beta decay beyond the standard model,” *Prog. Part. Nucl. Phys.*, vol. 46, pp. 413–457, 2001.
- [25] M. Gonzalez-Alonso and O. Naviliat-Cuncic, “Kinematic sensitivity to the Fierz term of β -decay differential spectra,” *Phys. Rev.*, vol. C94, no. 3, p. 035503, 2016.

- [26] L. Hayen and N. Severijns, “Beta spectrum generator: High precision allowed β spectrum shapes,” *Computer Physics Communications*, vol. 240, pp. 152 – 164, 2019.
- [27] N. Severijns, “Correlation and spectrum shape measurements in β -decay probing the standard model,” *Journal of Physics G: Nuclear and Particle Physics*, vol. 41, p. 114006, oct 2014.
- [28] V. Cirigliano, A. Garcia, D. Gazit, O. Naviliat-Cuncic, G. Savard, and A. Young, “Precision Beta Decay as a Probe of New Physics,” 2019.
- [29] L. Hayen, J. Kostensalo, N. Severijns, and J. Suhonen, “First-forbidden transitions in reactor antineutrino spectra,” *Phys. Rev.*, vol. C99, no. 3, p. 031301, 2019.
- [30] G. S3ti, *Search for a tensor component in the weak interaction Hamiltonian*. PhD thesis, KU Leuven, 2013.
- [31] A. Sharma and F. Sauli, “Low mass gas mixtures for drift chambers operation,” *Nuclear Instruments and Methods in Physics Research Section A: Accelerators, Spectrometers, Detectors and Associated Equipment*, vol. 350, no. 3, pp. 470 – 477, 1994.
- [32] C. Grab, “Studies of helium gas mixtures as a drift chamber gas,” in *B Factories: the State of the Art in Accelerators, Detectors, and Physics Stanford, California, April 6-10, 1992*, pp. 0443–448, 1992.
- [33] K. Lojek, K. Bodek, and M. Kuzniak, “Ultra-thin gas detector for tracking of low energy electrons,” *Nuclear Instruments and Methods in Physics Research Section A: Accelerators, Spectrometers, Detectors and Associated Equipment*, vol. 611, no. 2, pp. 284 – 288, 2009.
- [34] K. Lojek, D. Rozp3dzik, K. Bodek, M. Perkowski, and N. Severijns, “Data acquisition for multi-wire gas detector,” *Nuclear Instruments and Methods in Physics Research A*, vol. 802, pp. 38–47, 2015.
- [35] O. Naviliat-Cuncic, “Searches for exotic interactions in nuclear beta decay,” *AIP Conference Proceedings*, vol. 1753, no. 1, p. 060001, 2016.
- [36] X. Huyan, O. Naviliat-Cuncic, P. Voytas, S. Chandavar, M. Hughes, K. Minamisono, and S. V. Paulauskas, “Geant4 simulations of the absorption of photons in CsI and NaI produced by electrons with energies up to 4 MeV and their application to precision measurements of the β -energy spectrum with a calorimetric technique,” *Nucl. Instrum. Meth.*, vol. A879, pp. 134–140, 2018.

- [37] D. Pocanic *et al.*, “Nab: Measurement Principles, Apparatus and Uncertainties,” *Nucl. Instrum. Meth.*, vol. A611, pp. 211–215, 2009.
- [38] L. Broussard *et al.*, “Using Nab to determine correlations in unpolarized neutron decay,” *Hyperfine Interact.*, vol. 240, no. 1, p. 1, 2019.
- [39] D. Moser, H. Abele, J. Bosina, H. Fillunger, T. Soldner, X. Wang, J. Zmeskal, and G. Konrad, “NoMoS: An $R \times B$ drift momentum spectrometer for beta decay studies,” *EPJ Web Conf.*, vol. 219, p. 04003, 2019.
- [40] D. M. Asner *et al.*, “Single electron detection and spectroscopy via relativistic cyclotron radiation,” *Phys. Rev. Lett.*, vol. 114, no. 16, p. 162501, 2015.
- [41] C. D. Anderson, “The Positive Electron,” *Phys. Rev.*, vol. 43, pp. 491–494, Mar 1933.
- [42] F. J. Hasert *et al.*, “Observation of Neutrino Like Interactions Without Muon Or Electron in the Gargamelle Neutrino Experiment,” *Phys. Lett.*, vol. B46, pp. 138–140, 1973.
- [43] CERN, “Gargamelle: first neutral current.” <https://cds.cern.ch/record/39468>, 1973. [Online; accessed 20-06-19].
- [44] CERN, “First proton-antiproton collisions in the cern sps collider,” *Physics Letters B*, vol. 107, no. 4, pp. 306 – 309, 1981.
- [45] Wikimedia. https://upload.wikimedia.org/wikipedia/commons/2/2b/CERN_UA5_-_ppbar_interaction_at_540GeV.jpg. [Online; accessed 07-07-19].
- [46] G. Charpak, R. Bouclier, T. Bressani, J. Favier, and C. Zupancic, “The Use of Multiwire Proportional Counters to Select and Localize Charged Particles,” *Nucl. Instrum. Meth.*, vol. 62, pp. 262–268, 1968.
- [47] G. F. Knoll, *Radiation Detection and Measurement*, 3rd ed. New York: John Wiley and Sons, 2000.
- [48] W. Blum, L. Rolandi, and W. Riegler, *Particle detection with drift chambers*. Particle Acceleration and Detection, 2008.
- [49] F. Sauli, “Principles of Operation of Multiwire Proportional and Drift Chambers,” 1977.
- [50] M. P. Titov, “Gaseous Detectors: Recent developments and applications,” in *Trans-European School of High Energy Physics (TES HEP) Zakopane, Poland, July 8-14, 2009*, 2010.

- [51] A. A. Bednyakov, “On the molière theory of multiple scattering of charged particles (1947–1948) and its critique in subsequent years,” *Physics of Particles and Nuclei*, vol. 45, pp. 991–999, Sep 2014.
- [52] G. R. Lynch and O. I. Dahl, “Approximations to multiple Coulomb scattering,” *Nucl. Instrum. Meth.*, vol. B58, pp. 6–10, 1991.
- [53] T. Tabata, R. Ito, and S. Okabe, “An empirical equation for the backscattering coefficient of electrons,” *Nuclear Instruments and Methods*, vol. 94, no. 3, pp. 509 – 513, 1971.
- [54] C. AB, “COMSOL multiphysics.” <https://www.comsol.com>. [Online; accessed 08-07-19].
- [55] L. D. Keukeleere. Personal communication.
- [56] O. Sahin, I. Tapan, E. N. Ozmutlu, and R. Veenhof, “Penning transfer in argon-based gas mixtures,” *JINST*, vol. 5, no. 05, p. P05002, 2010.
- [57] E. B. Wagner, F. J. Davis, and G. S. Hurst, “Time-of-Flight Investigations of Electron Transport in Some Atomic and Molecular Gases,” *The Journal of Chemical Physics*, vol. 47, no. 9, pp. 3138–3147, 1967.
- [58] J. H. J. Parker and J. J. Lowke, “Theory of Electron Diffusion Parallel to Electric Fields. I. Theory,” *Phys. Rev.*, vol. 181, no. 1, p. 290, 1969.
- [59] F. Penning, “The starting potential of the glow discharge in neon argon mixtures between large parallel plates: Ii. discussion of the ionisation and excitation by electrons and metastable atoms,” *Physica*, vol. 1, no. 7, pp. 1028 – 1044, 1934.
- [60] G. v. Rossum, “Python tutorial,” Tech. Rep. CS-R9526, Centrum voor Wiskunde en Informatica (CWI), Amsterdam, May 1995.
- [61] T. Q. C. Ltd, “Qt Documentation.” <https://doc.qt.io/>. [Online; accessed 20-06-19].
- [62] c++. <https://isocpp.org/>. [Online; accessed 08-07-19].
- [63] T. H. Group, “Hierarchical data format version 5.” <https://www.hdfgroup.org/HDF5>. [Online; accessed 08-07-19].
- [64] pySerial module. <https://www.pyserial.readthedocs.io>. [Online; accessed 08-07-19].
- [65] P. D. Team, “PyTables: Hierarchical Datasets in Python.” <http://www.pytables.org/>, 2002. [Online; accessed 08-07-19].

- [66] E. Jones, O. T., P. Peterson, *et al.*, “SciPy: Open source scientific tools for Python.” <http://www.scipy.org/>, 2001. [Online; accessed 20-06-19].
- [67] O. Travis, *NumPy: A guide to NumPy*, 2006.
- [68] J. D. Hunter, “Matplotlib: A 2D graphics environment,” *Computing In Science & Engineering*, vol. 9, no. 3, pp. 90–95, 2007.
- [69] E. O. LEBIGOT, “Uncertainties: a Python package for calculations with uncertainties.” <http://pythonhosted.org/uncertainties/>. [Online; accessed 20-06-19].
- [70] M. Newville, T. Stensitzki, D. B. Allen, and A. Ingargiola, “LMFIT: Non-Linear Least-Square Minimization and Curve-Fitting for Python,” Sept. 2014.
- [71] Anaconda Software Distribution. <https://anaconda.com>. [Online; accessed 07-07-19].
- [72] L. Malter, “Thin Film Field Emission,” *Phys. Rev.*, vol. 50, pp. 48–58, Jul 1936.
- [73] LPC Caen, “Fast Acquisition System for nuclEAr Research.” <http://faster.in2p3.fr/index.php/about-faster>. [Online; accessed 08-07-19].
- [74] I. A. E. Agency, “Live Chart of Nuclides.” <https://www-nds.iaea.org/relnsd/vcharthtml/VChartHTML.html>. [Online; accessed 20-06-19].
- [75] A. M. Boyarski, “Additives that prevent or reverse cathode aging in drift chambers with helium isobutane gas,” *Nucl. Instrum. Meth.*, vol. A515, pp. 190–195, 2003.
- [76] M. Atac, “Breakdown processes in wire chambers, prevention and rate capability,” in *Proceedings of the 1983 DPF workshop on collider detectors: present capabilities and future possibilities* (S. C. Loken and P. Nemethy, eds.), pp. 88–96, Lawrence Berkeley Laboratory, University of California, 1983.
- [77] T. J. Sumner, P. D. Smith, G. K. Rochester, and R. K. Sood, “After-pulses from drift chambers,” *Nuclear Instruments and Methods in Physics Research*, vol. 224, pp. 477–488, 1984.
- [78] K. Lojek. Personal communication.

- [79] D. Pfeiffer, L. D. Keukeleere, *et al.*, “Interfacing Geant4, Garfield++ and Degrad for the simulation of gaseous detectors,” *Proceedings of the IRE*, vol. 27, pp. 584–585, 1939.
- [80] A. Breskin, G. Charpak, B. Gabioud, F. Sauli, N. Trautner, W. Duinker, and G. Schultz, “Further results on the operation of high-accuracy drift chambers,” *Nuclear Instruments and Methods*, vol. 119, pp. 9 – 28, 1974.
- [81] G. Gaudio, “Test of the BIL tracking chambers for the ATLAS muon spectrometer,” *Nucl. Instrum. Meth.*, vol. A572, pp. 62–63, 2007.
- [82] W. S. Cleveland, “Robust Locally Weighted Regression and Smoothing Scatterplots,” *Journal of the American Statistical Association*, vol. 74, no. 368, pp. 829–836, 1979.
- [83] S. Ramo, “Currents Induced by Electron Motion,” *Proceedings of the IRE*, vol. 27, pp. 584–585, 1939.
- [84] W. Shockley, “Currents to Conductors Induced by a Moving Point Charge,” *Journal of Applied Physics*, vol. 9, p. 635, 1938.
- [85] K. Bodek. Personal communication.
- [86] K. P. Hickerson, X. Sun, Y. Bagdasarova, D. Bravo-Berguño, L. J. Broussard, M. A.-P. Brown, R. Carr, S. Currie, X. Ding, B. W. Filippone, A. García, P. Geltenbort, J. Hoagland, A. T. Holley, R. Hong, T. M. Ito, A. Knecht, C.-Y. Liu, J. L. Liu, M. Makela, R. R. Mammei, J. W. Martin, D. Melconian, M. P. Mendenhall, S. D. Moore, C. L. Morris, R. W. Pattie, A. Pérez Galván, R. Picker, M. L. Pitt, B. Plaster, J. C. Ramsey, R. Rios, A. Saunders, S. J. Seestrom, E. I. Sharapov, W. E. Sondheim, E. Tatar, R. B. Vogelaar, B. VornDick, C. Wrede, A. R. Young, and B. A. Zeck, “First direct constraints on Fierz interference in free-neutron β decay,” *Phys. Rev. C*, vol. 96, p. 042501, Oct 2017.
- [87] S. Agostinelli *et al.*, “GEANT4: A Simulation toolkit,” *Nucl. Instrum. Meth.*, vol. A506, pp. 250–303, 2003.
- [88] A. Kozela, G. Ban, A. Bialek, K. Bodek, P. Gorel, K. Kirch, S. Kistryn, O. Naviliat-Cuncic, N. Severijns, E. Stephan, and J. Zejma, “Measurement of the transverse polarization of electrons emitted in free neutron decay,” *Phys. Rev. C*, vol. 85, p. 045501, Apr 2012.
- [89] J. C. Hardy and I. S. Towner, “Superallowed $0^+ \rightarrow 0^+$ nuclear β decays: 2014 critical survey, with precise results for V_{ud} and CKM unitarity,” *Phys. Rev.*, vol. C91, no. 2, p. 025501, 2015.

- [90] M. Perkowski, K. Bodek, L. De Keukeleere, L. Hayen, A. Kozela, K. Lojek, D. Rozpędzik, and N. Severijns, “Initial Tests of MiniBETA Spectrometer Performance,” *Acta Phys. Polon.*, vol. B49, p. 261, 2018.
- [91] B. Aubert, *Neutral Currents*, pp. 743–755. Boston, MA: Springer US, 1996.
- [92] N. Severijns and O. Naviliat-Cuncic, “Structure and symmetries of the weak interaction in nuclear beta decay,” *Physica Scripta*, vol. T152, p. 014018, jan 2013.
- [93] J. Smyrski *et al.*, “Drift chamber with a c-shaped frame,” *Nucl. Instrum. Meth.*, vol. A541, pp. 574–582, 2005.

FACULTY OF SCIENCE
DEPARTMENT OF PHYSICS AND ASTRONOMY
WEAK INTERACTIONS GROUP
Celestijnenlaan 200D box 2418
B-3001 Leuven

